

Washington University in St. Louis  
**Washington University Open Scholarship**

---

Engineering and Applied Science Theses &  
Dissertations

McKelvey School of Engineering

---

Summer 8-15-2017

# Development of High Resolution Tools for Investigating Cardiac Arrhythmia Dynamics

Christopher Reed Gloschat  
*Washington University in St. Louis*

Follow this and additional works at: [https://openscholarship.wustl.edu/eng\\_etds](https://openscholarship.wustl.edu/eng_etds)



Part of the [Biomedical Engineering and Bioengineering Commons](#)

---

## Recommended Citation

Gloschat, Christopher Reed, "Development of High Resolution Tools for Investigating Cardiac Arrhythmia Dynamics" (2017).  
*Engineering and Applied Science Theses & Dissertations*. 307.  
[https://openscholarship.wustl.edu/eng\\_etds/307](https://openscholarship.wustl.edu/eng_etds/307)

This Dissertation is brought to you for free and open access by the McKelvey School of Engineering at Washington University Open Scholarship. It has been accepted for inclusion in Engineering and Applied Science Theses & Dissertations by an authorized administrator of Washington University Open Scholarship. For more information, please contact [digital@wumail.wustl.edu](mailto:digital@wumail.wustl.edu).

Washington University in St. Louis  
School of Engineering and Applied Science  
Department of Biomedical Engineering

Dissertation Examination Committee:  
Igor Efimov, Co-Chair  
Yoram Rudy, Co-Chair  
Philip Bayly  
Stacey Rentschler  
Richard Schuessler  
Jonathan Silva

Development of High Resolution Tools for Investigating Cardiac Arrhythmia Dynamics

by

Christopher Reed Gloschat

A dissertation presented to  
The Graduate School  
of Washington University in  
partial fulfillment of the  
requirements for the degree  
of Doctor of Philosophy

August 2017  
Saint Louis, Missouri



copyright by  
Christopher Reed Gloschat  
2017

# Contents

List of Tables . . . . .	iv
List of Figures . . . . .	v
Acknowledgments . . . . .	xiii
Abstract . . . . .	xvii
<b>1 Introduction . . . . .</b>	<b>1</b>
1.1 Origin and History of Arrhythmia Research . . . . .	1
1.2 Development of Modern Day Investigative Tools . . . . .	4
1.3 The Role of Restitution Dynamics in VF . . . . .	6
1.4 Dissertation Scope and Procedure . . . . .	7
<b>2 Capacitively Coupled Arrays of Multiplexed, Flexible Silicon Transistors for Cardiac Electrophysiology . . . . .</b>	<b>9</b>
2.1 Abstract . . . . .	9
2.2 Key Terms . . . . .	10
2.3 Introduction . . . . .	10
2.4 Results . . . . .	13
2.4.1 Capacitively coupled silicon nanomembrane transistors as active sensing nodes . . . . .	13
2.4.2 <i>In vitro</i> assessment of electrical performance . . . . .	17
2.4.3 Cardiac mapping in animal heart models . . . . .	21
2.4.4 Comparison of fluorescence imaging . . . . .	22
2.4.5 Study of ventricular fibrillation . . . . .	26
2.5 Discussion . . . . .	26
2.6 Methods . . . . .	29
2.6.1 Capacitively coupled active sensing node design . . . . .	29
2.6.2 Device Fabrication . . . . .	31
2.6.3 Data acquisition . . . . .	32
2.6.4 Signal processing . . . . .	34
2.6.5 Animal experiments . . . . .	34
2.7 Acknowledgements . . . . .	35

<b>3</b>	<b>Improved Panoramic Imaging for Small Mammal Hearts . . . . .</b>	<b>36</b>
3.1	Abstract . . . . .	36
3.2	Key Terms . . . . .	37
3.3	Introduction . . . . .	37
3.3.1	Experimental Setup . . . . .	40
3.3.2	Camera Calibration . . . . .	42
3.3.3	Optical Mapping . . . . .	45
3.3.4	Surface Generation . . . . .	46
3.3.5	Projection and Visualization . . . . .	49
3.4	Results . . . . .	50
3.5	Acknowledgements . . . . .	56
<b>4</b>	<b>Role of Restitution Dynamics in Initiation and Maintenance of Ventricular Arrhythmias . . . . .</b>	<b>57</b>
4.1	Abstract . . . . .	57
4.2	Key Terms . . . . .	58
4.3	Introduction . . . . .	58
4.4	Methods . . . . .	60
4.4.1	Animal Experiments . . . . .	60
4.4.2	Data Analysis . . . . .	61
4.5	Results . . . . .	63
4.6	Discussion . . . . .	66
4.7	Future Work . . . . .	68
4.8	Acknowledgements . . . . .	68
<b>5</b>	<b>Summary and Future Directions . . . . .</b>	<b>69</b>
5.1	Active Capacitive Electrodes . . . . .	69
5.2	High Resolution Panoramic Optical Mapping . . . . .	70
5.3	Action Potential Duration Restitution . . . . .	72
<b>Appendix A MATLAB Code for Panoramic Optical Mapping Graphical User Interfaces . . . . .</b>		<b>73</b>
<b>Appendix B <math>I_{Ks}</math> Regulates Action Potential Duration in a Rate Dependent Manner . . . . .</b>		<b>74</b>
B.1	Introduction . . . . .	74
B.2	Methods . . . . .	76
B.3	Results . . . . .	77
B.4	Conclusion . . . . .	77
B.5	Acknowledgements . . . . .	78
<b>References . . . . .</b>		<b>79</b>

# List of Tables

3.1	<b>Camera and Mesh Resolutions.</b> Mapping and geometric camera resolutions were calculated by measuring the number of pixels across the cuboid in each calibration image. Final voxel resolution is that of the smallest voxels in the octree volume. The number of faces is that of the triangulated mesh output from the VTK code. Average inter-centroidal distance is the average distance between each centroid projected onto a mapping camera and it's nearest neighbor on that 2D plane. . . . .	51
-----	--	----

# List of Figures

1.1	<b>(Left) Mines' Model of Anatomical Reentry.</b> Preparation of Mines made from a tortoise heart. Unidirectional block was induced and a reentrant anatomical reentry observed <b>(Right) Mines' Theory of Reentry.</b> The dark region represents a wavefront of depolarization which is in absolute refractory, the speckled region is in relative refractory, and the white region is excitable. The excitable gap is some combination of the excitable and relative refractory regions. In A absolute refractory persists too long for reentry to occur. In B either conduction velocity is slower or repolarization is faster. In either situation the wavefront never interacts with its tail and is able to persist. Adapted from Mines, 1913 [75]. . . . .	2
1.2	<b>Initiation of Reentrant Vortices.</b> <b>(1)</b> A wavefront approaches a non-excitable functional obstacle. <b>(2)</b> The wavefront breaks on the obstacle separating into two individual wavefronts. <b>(3)</b> When excitability is high enough the ends of the broken waves, often called phase singularities (PS), begin curling. <b>(4)</b> This curling can progress into counter rotating vortices. Adapted from Jalife, 2000 [50]. . . . .	3
1.3	<b>Early electrocardiogram.</b> Einthoven was the first to measure a cardiac electrogram without making direct contact with the heart. He did so by placing his hand and left foot in tubs of salt water that were attached to a string galvanometer. . . . .	4
1.4	<b>Theory of APDR induced alternans.</b> It is known that APD is a directly modulated by the DI that precedes it. It has been theorized that low APDR slopes <b>(A)</b> will result in modulation of the APD which approaches a steady state value, while high APRD slopes <b>(B)</b> will result in alternating APD which will become further and further removed from one another at shorter cycle lengths [116]. Image modified from Weiss et al 1999. . . . .	6

2.1	<b>Capacitively coupled silicon nanomembrane transistors (covered by a thermal SiO<sub>2</sub> layer) as active sensing nodes in actively multiplexed flexible electronic system for high resolution electrophysiological mapping.</b> (a) Exploded-view schematic illustration (left) and a photograph (right) of a completed capacitively-coupled flexible sensing system with 396 nodes in a slightly bend state. The arrows in the left illustration highlight the key functional layers. Inset on the right shows a magnified view of a few nodes. (b) Circuit diagram for a node in this capacitively coupled array, with annotations for each component (left), and an optical microscope image of the cell (middle). A schematic of the circuit cross-section (right) illustrates the mechanism for capacitively coupled sensing through a thermal SiO <sub>2</sub> layer to an underlying transistor. . . . .	15
2.2	<b>In vitro assessment of electrical performance.</b> (a) Average gain of a representative capacitively coupled transistor as a function of the input frequency (f) from 0.1 to 100 Hz. Inset shows the responses from this sensor node at 0.1 Hz (top) and 100 Hz (bottom), after band-pass filtering (0.05-568 Hz). (b) Power spectral density of a 5 mV AC signal at 10 Hz measured at a representative node, showing a typical 1/f relationship at low frequency. The input was a sine-wave of 5 mV at 10 Hz. (c) Histograms of noise (with Gaussian fitting) measured from all 396 nodes of the device in Fig. 1c. (d) Statistics of the threshold voltage (V <sub>T</sub> ) and peak effective mobility ( $\mu_{eff}$ ) of test transistors from 15 different arrays. (e) Statistics of yield (left) and gain (right) of 17 capacitively coupled, active sensing 18x22 electrode array. (f) Image of a device during a mechanical bending test. (g) Image of a device completely immersed in a saline solution, during a soak test. (h) Yield (Y, defined as the number of working nodes divided by the total number of nodes) as a function of cycles of bending to 5 mm bend radius, showing minimal changes up to 10000 cycles. (i) Electrical leakage current of 2 devices during soak testing. Minimal leakage appears over a period of 120 days at 37 °C. (j) Response of a representative node to a sine wave input (at 10 Hz) before, after 10000 cycles bending, and after saline immersion for 120 days. . . . .	18

2.3	<b>High density cardiac electrophysiological mapping on ex vivo rabbit heart models.</b> (a) A photograph of a flexible capacitively coupled sensing electronic system on a Langendorff-perfused rabbit heart (left). Magnified view, showing conformal contact of the device to the cardiac tissue, via the action of surface tension (right). (b) Representative single voltage trace from the electrode array without external pacing. Signatures related to the P, Q, R, S, and T waves in ECG traces, can be identified from the recordings. (c) Representative voltage data for all electrodes at four time points (indicated in B), showing normal cardiac wave-front propagation. The progress of the cardiac wave is consistent with the physical location of the array on heart, as illustrated in the diagram on the left (RA, LA, RV and LV stands for right atrium, left atrium, right ventricle, and left ventricle respectively). . . . .	20
2.4	<b>Signal morphology unaffected by experimental conditions.</b> Voltage traces from the same channel in the capacitively coupled sensing electronic system at the beginning and end of an ex vivo Langendorff perfused rabbit heart experiment. The amplitude and noise levels of the signal remain the same, demonstrating the stability of capacitive sensing over the entire course of the ex vivo experiment. . . . .	22
2.5	<b>Comparison of Conduction Velocity</b> Calculated conduction velocity vector from optical and electrical maps at pacing of 300 ms cycle length. The magnitude of the red arrows indicates the amplitude of the velocity. The background maps are activation in grayscale. . . . .	23
2.6	<b>In Vivo Recordings.</b> <i>In vivo</i> recording using a capacitively coupled sensing electronic system from a beating heart. (a) A photograph of a device laminated onto the left ventricle of a beating heart in an open chest experiment on a canine model. (b) Representative single voltage trace from the device (top), with representative voltage data map at four time points, showing normal cardiac wave-front propagation (bottom). . . . .	23

2.7	<b>Comparison of electrical mapping with optical fluorescence recording.</b> (a) Representative electrical and optical signals captured simultaneously on a Langendorff-perfused rabbit heart at multiple cycle lengths (300, 250, and 200 ms). (b) Interpolated spatial activation maps derived from these data. Top row shows activation as measured during sinus rhythm. The bottom row corresponds to 300 ms ventricular pacing. The activation maps from left to right are optical signals from the whole heart, optical signals from the device area, and electrical signals respectively. The dashed boxes in the whole heart illustrations depict the device area. (c) Comparison of activation and repolarization measurements in a single simultaneously measured electrical and optical signals. Left figure highlights a quantitative comparison of electrical and optical signals during one depolarization/repolarization cycle. Center figure shows the comparison of activation times measured across all electronic nodes and corresponding optical field of view. Right figure shows the comparison of optical and electrical restitution curves measured at various cycle lengths (300, 250, 225, 200, 175 ms). . . . .	24
2.8	<b>Comparison of Optical and Electrical Signals.</b> Sample equivalence test between the electrical and optical recordings. In order to demonstrate the accuracy of the bioelectric signals measured by the electrode a two sample equivalency test was performed using the electrode measurements as the test data and the optical measurements as the reference data. In the case of both (a) sinus rhythm and (b) 300 ms ventricular pacing, the isochronal maps of activation were found to be equivalent ( $p < 0.05$ ) for both upper and lower bounds. Here the CI, LEL, UEL stand for confidence interval, lower equivalence limit and upper equivalence limit respectively. . . . .	25
2.9	<b>Study of ventricular fibrillation (VF).</b> (a) Three representative electronic node signals taken from a heart during VF. The dashed box specifies the window of time corresponding to two reentrant cycles of VF. The labels $-\pi$ , 0, and $+\pi$ indicate the initial phase values of the respective signals at the beginning of the reentrant cycle. (b) Voltage, phase and phase singularity maps at six time points corresponding to the dash lines specified in (a). Number 1, 2, and 3 on the maps mark the locations where the signals in (a) were taken. Voltage and phase data indicate a reentrant cycle of VF. A phase singularity commonly refers to a point on a phase map around which all values of phase (i.e. $-\pi$ to $+\pi$ ) are represented. The phase singularities are identified as the $\pm 1$ values associated with regions of the phase map where this occurs. Optical signals from the sensing electronics area also match well with electrical recordings . . . . .	27
2.10	<b>Electrode Data Acquisition System.</b> A Photograph of the data acquisition system with the electrode array during in vitro bench testing. . . . .	33



2.11	<b>Electrode Array and Connector.</b> Photographs of an electrode array before (left) and after (right) being inserted into an interface PCB board through a zero- insertion-force (ZIF) connector. . . . .	33
3.1	<b>Panoramic optical mapping system.</b> (A) Panoramic optical mapping requires a more complex setup than optical mapping conducted with a single camera. In addition to increasing the number of optical cameras, we designed and 3D printed a number of experimental components to facilitate the experiments. (B) An upright chamber with four windows for optical cameras and four smaller windows for excitation LEDs. The chamber was waterproofed using a multiple smooth layers of latex based paint on both the interior and exterior surfaces. (C) A bubble trap mount to facilitate raising and lowering of the perfusion system with the rotational stage. (D) After administration of the excitation-contraction uncoupler, a suture is based through the eyelet in the base of the platform, passed through the apex, returned through the eyelet, and brought up and around the leveraging block. A clip is then used to anchor the suture in place. (E) Ag-AgCl electrodes are mounted to the cannula holder to maintain close and consistent pseudo ECG recordings during each experiment. . . . .	39
3.2	<b>Calibration of geometry and optical cameras.</b> (A) MATLAB graphical user interface to semi-automate the calibration of each camera needed to facilitate the projection of optical data onto the geometric surface. Detailed explanations and code are included in the addendum. (B) The cuboid is used to create a global coordinate system whose origin is at the cuboid's center. All grid junctions on the cuboid surface have known coordinates in the global coordinate system. Identification of these points in a 2D image provides the necessary number of known values to solve for the unknown components of the global-to-camera (i.e., transformation) and the camera-to-sensor (i.e., perspective projection) matrices. . . . .	43
3.3	<b>Geometric reconstruction.</b> (A) A MATLAB graphical user interface was developed to facilitate accurate identification of the heart silhouettes needed for geometric reconstruction. A detailed description and the code are included in the addendum. (B) The heart was rotated and binary silhouette images were collected every 5 degrees. (C) Using the occluding contours method paired with an octree algorithm a series of voxels are iteratively broken down to identify the heart volume. (D) This binary volume is passed by MATLAB as the input to a VTK program that creates a triangulated mesh representative of the binary volume. . . . .	47

3.4	<b>Data processing and projection</b> (A) A final MATLAB GUI was created to facilitate the processing of optical data and its projection onto the representative geometry. (B) Tools are provided to correct minor inaccuracies in projection. Camera facing centroids are first identified as those whose normals ( $\hat{N}_{\text{cell}}$ ) creates an angle greater than $90^\circ$ with the camera normal ( $\hat{N}_{\text{ic}}$ ). (C) The surface can then be visualized as a triangulated mesh (i), a map of the camera assignments made to each centroid (ii), texture (iii), and membrane potential (iv). (D) Tools are provided to rotate the heart using click-and-drag, to the view from each camera, and to specific viewing angles using azimuth and elevation angles. . . . .	48
3.5	<b>Geometric accuracy and signal-to-noise ratio (SNR).</b> (A) To validate the geometric accuracy, an object of known volume and geometry (i.e. the calibration cuboid) was reconstructed. The reconstructed volume was within 3% of the measured volume of the cuboid. (B) Signals from the left ventricular anterior, free wall, and posterior regions are shown on a SNR map. . . . .	51
3.6	<b>Time course of activation.</b> (A) The time course of activation is tracked using membrane potential. A paced beat starts on the left ventricular free wall and the divergent wavefronts are tracked over time around both the posterior and anterior sides to where they meet on the right ventricular free wall. Wavefronts are uninterrupted by artifact or discontinuity. (B) A 2D Mercator projection of the isochronal activation map generated using the processing GUI. (C) A 2D Hammer projection whose latitude and longitude divisions are the same as seen in the Mercator projection. . . . .	53
3.7	<b>Action potential duration and arrhythmia assessment.</b> (A) Action potential duration can be calculated using projected data and unwrapped into Mercator and Hammer 2D representations. (B) Arrhythmias like ventricular fibrillation can be analyzed using calculations of dominant frequency, phase, and phase singularities. . . . .	54
3.8	<b>Representative rat data.</b> A paced beat is shown propagating from the right ventricular free wall into the left ventricular apex. Action potential duration shortens as a function of distance from the paced region. . . . .	54
4.1	<b>Dynamic Restitution Protocol.</b> The heart was paced for 30 beats at 300, 270, 240, 210, 180, and 150 ms pacing cycle lengths in sequence. A MATLAB algorithm was written to separate the signals by pacing cycle length and calculate $\text{APD}_{80}$ and DI averages. . . . .	61

4.2	<b>Definition of APD, DI, and APD Restitution.</b> (A) APD was defined as the difference between the activation of the beat in question ( $A_n$ ) and the time at which the action potential returns to 80% of its maximum amplitude ( $R_n$ ). DI was defined as the difference between $APD_{80}$ and the activation of the subsequent beat ( $A_{n+1}$ ). (B) APD restitution describes how APD shortens as DI shortens. At each pixel a negative exponential was fit to the average $APD_{80}$ and DI values. Goodness of fit was calculated at each pixel as well. . . . .	62
4.3	<b>Heat Maps of APDR Max Slope and Goodness of Fit.</b> An exponential curve was fitted to the APDR values at each pixel and the (A) maximum slope and (B) goodness of fit at each pixel were calculated. Broadly speaking, maximum slope values were greater than 1 with the highest values being located near the pacing site on the RV. Similarly, goodness of fit values largely exceeded 0.8. . . . .	63
4.4	<b>Phase Singularity Tracking During Five Consecutive Cycles After induction of VF,</b> the phase and phase and associated phase singularities were calculated. The top left image is a heat map of the maximum slope of the APDR with the pacing site labelled in black. Progressing left-to-right and top-to-bottom are the trajectories the phase singularity takes over the course of the first five reentrant beats that occurred after the arrhythmia anchored in the region of high maximum slope. It meander in or around this region for 32 consecutive beats. . . . .	64
4.5	<b>Alternans present in regions of slope &gt; 1.</b> At the two shortest cycle lengths, (A)180 ms and (B) 150 ms, increasingly pronounced alternans were observed. The maximum slope at the pixel from which the representative signal was derived was 1.0552. . . . .	65
4.6	<b>Comparison of Maximum Slope of APDR and Average APD at 300 ms.</b> Qualitative comparison demonstrates that the maximum restitution slope (Left) and average $APD_{80}$ (Middle) at a near intrinsic heart rate (i.e., 300 ms) are similar. A more quantitative comparison (Right) shows a direct relationship between maximum APDR slope and average $APD_{80}$ in two different clusters with residual outliers at lower slope values. . . . .	65
4.7	<b>Normalization of restitution curve as a percentage of steady state APD abolishes differences in maximum slope.</b> (A) Representative optical action potentials from sham, post-transverse aortic constriction (TAC) and negative current injection (TAC-INJ). (B) Representative dynamic restitution curves from each cohort. (C) Mean effect on $APD_{90}$ . (D) Mean maximum slope of APDR. (E) Mean maximum slope of the normalized APDR. Modified from Shattock et al [96]. . . . .	67
B.1	<b>Human heart preparation.</b> (A) The wedges were taken from marginal vessels branching off of the circumflex in the LV. (B) Once cut and cannulated, wedges are laid on their side and paced from the endocardium. . . . .	75

B.2	<b>Measurment locations.</b> (Left) Averages of APD were taken from the endocardium, midmyocardium, and epicardium. (Right) Examples of signals from the previously specified regions. . . . .	75
B.3	<b>Prolongation due to <math>I_{Ks}</math> Block.</b> (Left) Prolongation was significant in the endocardium and midmyocardium. (Right) Prolongation was approximately 10% in all regions. . . . .	76
B.4	<b>Prolongation due to <math>I_{Kr}</math> Block.</b> (Left) Prolongation trends toward greater amounts of prolongation following $I_{Kr}$ block. (Right) While not significant, prolongation increased by another 10% following $I_{Kr}$ blockade. . . . .	77

# Acknowledgments

I must start by thanking my PhD advisor, Dr. Igor Efimov, for patiently helping me find the projects that fit best and seeing them through to completion. Your passion for science and history have left a permanent mark on how I approach problems and see the world. I will forever look back on my time in your lab as one of growth and self exploration.

I also want to thank the other members of my committee: Drs. Yoram Rudy, Philip Bayly, Stacey Rentschler, Jonathan Silva, and Richard Schuessler. Your ideas and insights have been invaluable. The academic environment at Washington University was exceptional and I found and enjoyed many collaborations with professors, teachers, and students alike. Megan Flake deserves special mention for being the best lab manager to grace academia. You were a source of counsel and advice, especially when I was fresh and inexperienced. Thank you. A special thanks must be given to Karen Teasdale and Glen Reitz for making sure I met all my deadlines and for helping me avoid the logistical pitfalls associated with navigating a graduate program. You guys are the best. Patricia Widder also deserves special mention. Apparently being a teaching assistant is supposed to be hard. You made it so easy that I actually wanted to try out new labs with you and the undergrads on my own time. Pretty impressive.

I need to thank all the Efimov Lab members past and present that helped me along the way. Thank you to Jake Laughner and Matt Sulkin for recruiting me during my program visit. A special thank you to Dr. Bas Boukens for hours spent trying to figure out human AVN nodal and wedge preparations as well as hours spent discussing various results and their meaning. A number of undergraduates helped me along the way, but there are two that warrant a special mention. Emily Widder was an amazing student an immensely helpful and designing and 3D printing my first panoramic chamber. Shubham Gupta was key in testing the panoramic imaging software suite and making them easier to use.

Four years into this our lab moved to George Washington University and there are many people from there that deserve thanks as well. Aaron Koppel, without you I don't know how we would have gotten the lab set up. Thank you for doing everything you did in spite of being pulled in so many directions. Dr. Kay, thank you for your mentorship in figuring out how to update the panoramic imaging system and make it more robust. Without your help I would not have been able to build a system of the quality we were able to accomplish together. Kara, Angel, and Jaclyn deserve thanks as well for being a second pair of hands at the beginning of so many of my experiments.

Lastly, I would like to thank my family. To my parents, thank you for instilling me with the belief that I can accomplish whatever I set my mind to and for believing in me throughout this process. The biggest thanks of all goes to my wife, Lana Gloschat. You moved across the country with me and then did it again. You struggled, I struggled, we struggled, but you

were always there to help me dust myself off and keep pushing to the end. Without your love and support this would not have been possible.

Christopher Reed Gloschat

*Washington University in Saint Louis*

*August 2017*

Dedicated to my wife. Without your love and support this would not have been possible.



## ABSTRACT OF THE DISSERTATION

Development of High Resolution Tools for Investigating Cardiac Arrhythmia Dynamics

by

Christopher Reed Gloschat

Doctor of Philosophy in Biomedical Engineering

Washington University in St. Louis, August 2017

Research Advisor: Dr. Igor Efimov

Every year 300,000 Americans die due to sudden cardiac death. There are many pathologies, acquired and genetic, that can lead to sudden cardiac death. Regardless of the underlying pathology, death is frequently the result of ventricular tachycardia and/or fibrillation (VT/VF). Despite decades of research, the mechanisms of ventricular arrhythmia initiation and maintenance are still incompletely understood.

A contributing factor to this lack of understanding is the limitations of the investigative tools used to study VT/VF. Arrhythmias are organ level phenomena that are governed by cellular interactions and as such, near cellular levels of resolution are needed to tease out their intricacies. They are also behaviors that are not limited by region, but dynamically affect the entirety of the heart. For these reasons, high-resolution methodologies capable of measuring electrophysiology of the whole entirety of the ventricles will play an important role in gaining a complete understanding of the principles that govern ventricular arrhythmia dynamics. They will also be essential in the development of novel therapies for arrhythmia management.

In this dissertation, I first present the validation and characterization of a novel capacitive electrode design that overcomes the key limitations faced by modern implantable cardiac devices. I then outline the construction, methodologies, and open-source tools of an improved optical panoramic mapping system for small mammalian cardiac electrophysiology studies. I conclude with a small mammal study of the relationship between action potential duration restitution dynamics and the mechanisms of maintenance in ventricular arrhythmias.

# Chapter 1

## Introduction

### 1.1 Origin and History of Arrhythmia Research

Ventricular fibrillation was first observed by Ludwig and Hoffa as they passed an electric current through a heart and saw its activity become strange and disorganized [47]. Their contemporary, Edmé Vulpian, would later coin the phrase fibrillation and set himself apart from his peers by hypothesizing that the heart itself, rather than nervous system, was responsible for the initiation and maintenance of VF [112]. While fibrillation is an extremely multifaceted phenomenon I will break it down into two concepts: reentry and initiation.

In 1913 George Ralph Mines established the foundation of the theory of anatomical reentry by creating a model of functional reentry in a tortoise heart (Figure 1.1 Left). In this model he was able to induce unidirectional block and observe a wavefront propagate around the ring of tissue. He observed (Figure 1.1 Right) that if the propagating "...wave is slower and shorter..." the tissue can become excitatory once more resulting in reentry [75]. This condition creates a space between the wavefront and its own tail which constitutes the excitable gap where in a stimulus could induce depolarization. Just a year later Walter

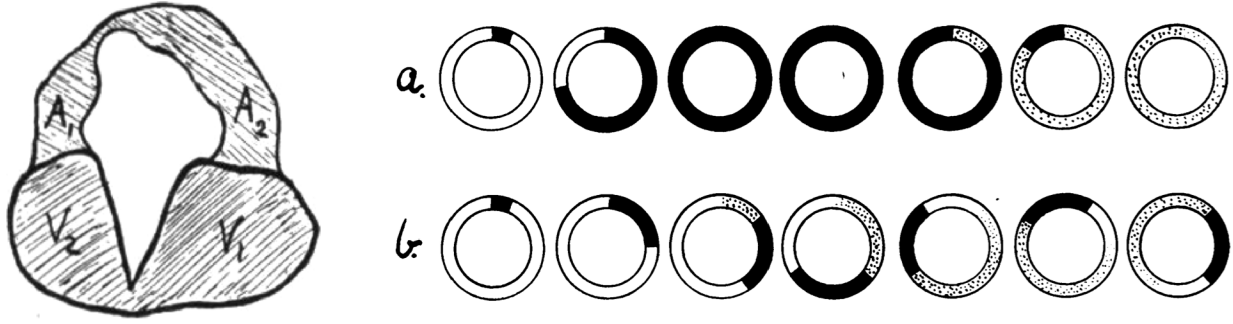


Figure 1.1: **(Left) Mines' Model of Anatomical Reentry.** Preparation of Mines made from a tortoise heart. Unidirectional block was induced and a reentrant anatomical reentry observed **(Right) Mines' Theory of Reentry.** The dark region represents a wavefront of depolarization which is in absolute refractory, the speckled region is in relative refractory, and the white region is excitable. The excitable gap is some combination of the excitable and relative refractory regions. In A absolute refractory persists too long for reentry to occur. In B either conduction velocity is slower or repolarization is faster. In either situation the wavefront never interacts with its tail and is able to persist. Adapted from Mines, 1913 [75].

Garrey published his "Critical Mass" hypothesis based on his observations that arrhythmias in smaller hearts (e.g. mouse, rat, guinea pig) typically self terminate while arrhythmias in larger mammals were self sustaining [37]. Contrary to Ludwig and Hoffa's observations that fibrillation is disorganized, Carl Wiggers would deduce from his cinematographic studies that VF was not entirely random and asynchronous, rather he observed that as VF progressed the regions of coordinated contraction in the myocardium increased in number while shrinking in size [119]. With the advent of tools for measuring epicardial potentials and optical action potentials our understanding of VF mechanics would grow in leaps and bounds. Studies using coherence analysis [92, 5], non-linear dynamics [38, 5], and analysis of vector loops [23] would be used in an attempt to understand the spatial distribution of VF and how it progresses in time. Subsequent studies by Gray et al. would develop a method for quantifying VF dynamics using phase analysis [40]. This method made it possible to identify the centers of reentrant waves (i.e. singularities) and observe their behavior over time. For example, in another study by Gray et al. they would show that despite electrocardiogram measurements

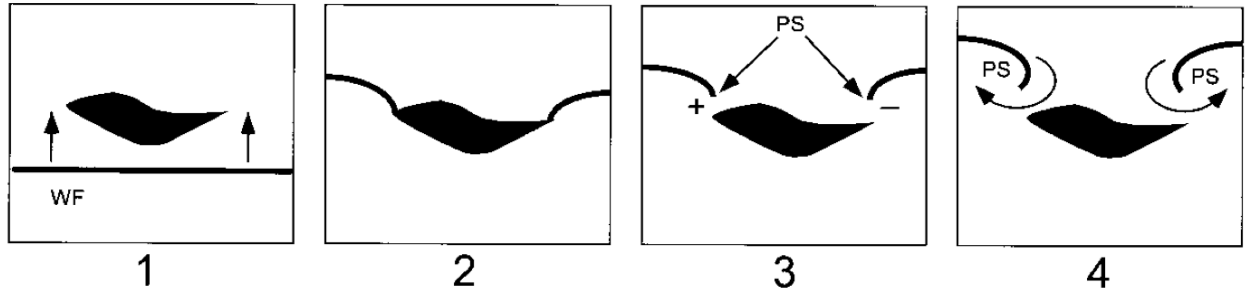


Figure 1.2: **Initiation of Reentrant Vortices.** (1) A wavefront approaches a non-excitable functional obstacle. (2) The wavefront breaks on the obstacle separating into two individual wavefronts. (3) When excitability is high enough the ends of the broken waves, often called phase singularities (PS), begin curling. (4) This curling can progress into counter rotating vortices. Adapted from Jalife, 2000 [50].

indicative of VF, phase analysis could use transmembrane potential values to show highly periodic behavior [39]. This body of work would produce substantial evidence that while VF behavior may change over time there are ways to quantify its spatio-temporal behavior [6], especially when assessed locally.

Initiation of arrhythmia can be separated by causality: anatomical and functional. Anatomical reentry occurs when inhomogeneities in cardiac tissue (e.g. fibrosis) create an obstacle for conduction like that described by Mines [75]. Many, like Wiener and Rosenblueth [118], believed that anatomical obstacles were necessary for fibrillation to occur. Functional reentry however can occur in healthy myocardium as the result of wave front-wave tail interactions. Wiggers and Wégria laid the groundwork for this when they discovered that VF was easily induced using short shocks timed during late systole, a period which would be dubbed the vulnerable phase [120]. The myocardium is vulnerable during this time frame because regions of the tissue are refractory while others have limited excitability. This creates a scenario similar to Fig. 2 adapted from Jalife [50] with the differences being two: 1) the anatomical structure would be replaced by a symbolic boundary between refractory and limited excitability tissue and 2) there would be a single phase singularity (PS) to form a vortex

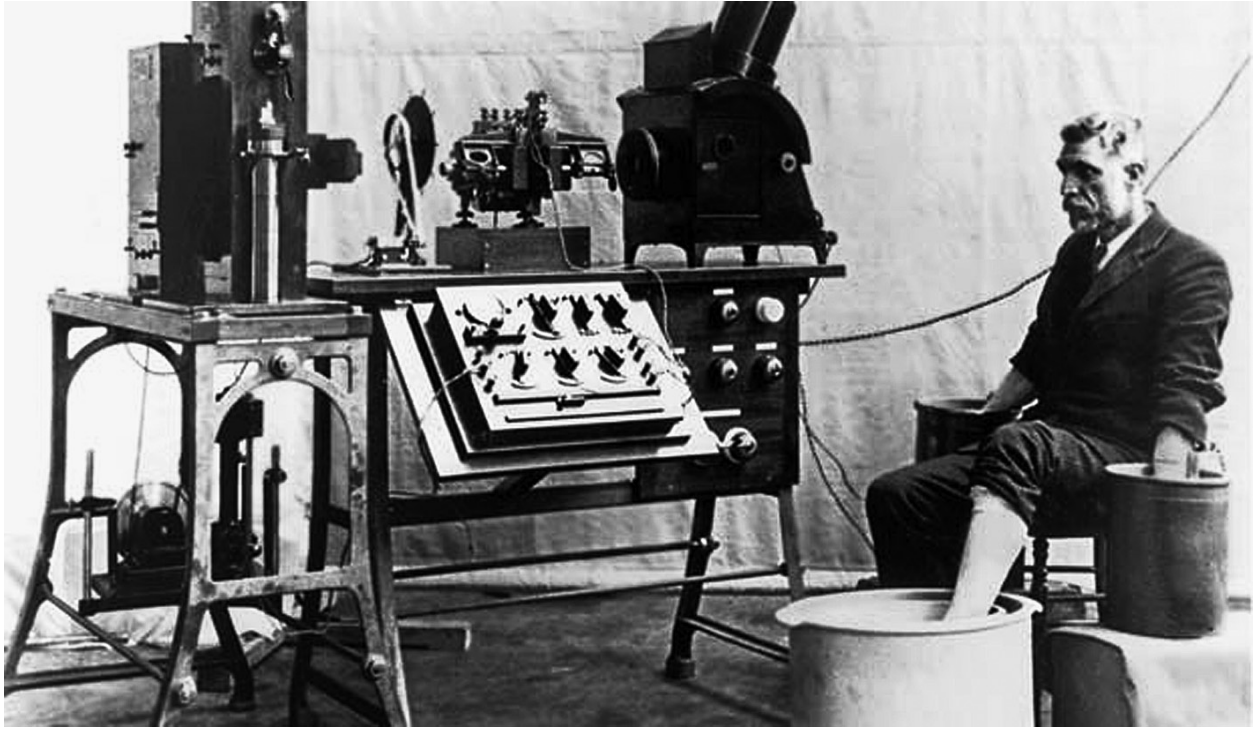


Figure 1.3: **Early electrocardiogram.** Einthoven was the first to measure a cardiac electrogram without making direct contact with the heart. He did so by placing his hand and left foot in tubs of salt water that were attached to a string galvanometer.

like reentry. Whether it's the result of an anatomical structure or a region of quiescent tissue the breaking of a wave front is the principal way reentry is initiated. Multiple protocols have been developed for initiating VF in this fashion.

## 1.2 Development of Modern Day Investigative Tools

Electrical mapping of the heart can be done both through indirect and direct contact. In 1901, Einthoven was the first to indirectly record the electrical activity of the heart using buckets of salt water as electrodes and a string galvanometer. This concept would later be turned into the first electrocardiogram device (Figure 1.3). As electrophysiologists sought to

better understand arrhythmic activity efforts were made to increase the spatial and temporal resolution of indirect and direct contact methods of recording electrical activity. To map explanted hearts, electrodes were sewn onto nylon meshes which were pulled over the heart to measure extracellular potentials in anatomically consistent locations [42]. Dense electrode arrays were built and placed on the epicardial surfaces to guide early efforts in the treatment of arrhythmias like atrial fibrillation [124]. In an effort to develop non-invasive methods for understanding local patterns of activation and repolarization, efforts were made to solve the inverse problem making it possible to reconstruct the epicardial activity of the heart from hundreds of body surface electrograms [16]. Sophisticated catheter systems have also been developed to reconstruct the cardiac anatomy and record from multiple sites simultaneously [103]. While these and many other methods for electrical mapping have improved dramatically in recent decades providing great insights into arrhythmia initiation and maintenance, their spatial resolution is still insufficient to tease out the intricacies of reentry, especially in explanted small mammal hearts. They are also unable to measure the immediate response of the heart during and after defibrillation.

In the last two decades, optical mapping has become an alternative methodology for measuring physiological characteristics. Optical mapping uses fluorescent dyes (e.g. di-4-ANBDQBS) that, for the purposes of this dissertation, bind the cell membrane. Their fluorescence intensity fluctuates with changes in membrane potential and can be separated from the excitation spectrum (630 nm) using a 700 nm long pass filter [74]. Key characteristics have been identified in these signal morphologies, among them are indicators of activation and repolarization [28]. In recent years the cameras used to measure fluorescence have increased their spatial resolution to sub millimeter resolutions. This combined with optical mappings' immunity to defibrillation artifacts, has made it a key tool in assessing arrhythmic response to therapy [88]. Creation of panoramic imaging systems capable of measuring optical action potentials

**A** *APD restitution slope  $< 1$*

**B** *APD restitution slope  $> 1$*

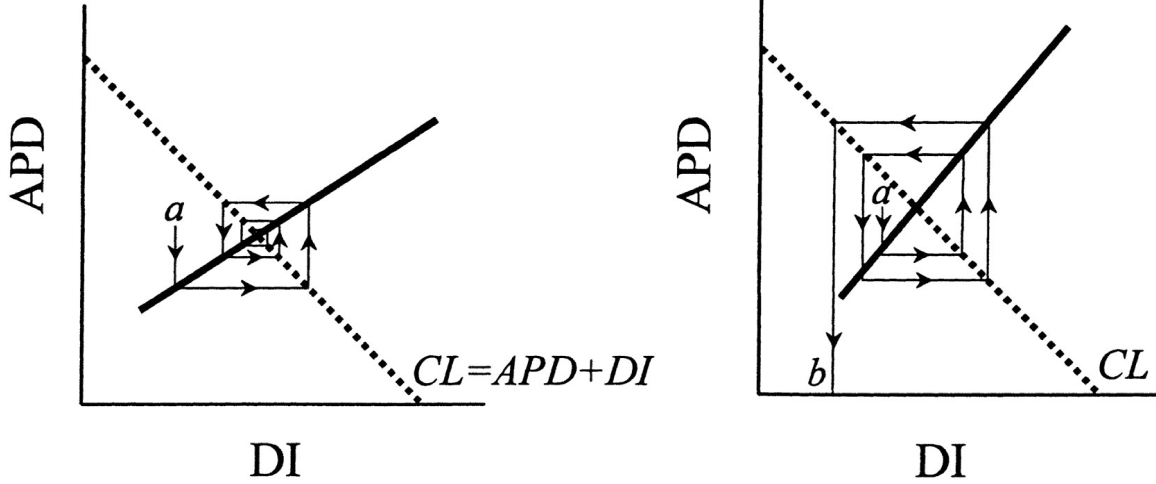


Figure 1.4: **Theory of APDR induced alternans.** It is known that APD is a directly modulated by the DI that precedes it. It has been theorized that low APDR slopes (**A**) will result in modulation of the APD which approaches a steady state value, while high APDR slopes (**B**) will result in alternating APD which will become further and further removed from one another at shorter cycle lengths [116]. Image modified from Weiss et al 1999.

across the entirety of the epicardial surface [54, 86] have made this methodology a key tool in tracking arrhythmia dynamics, especially the phenomenon like reentrant rotors of activity capable of meandering out of the field of view of a traditional monocular optical mapping systems [53].

### 1.3 The Role of Restitution Dynamics in VF

Cardiac restitution refers to the dependence of action potential duration (APD) and conduction velocity (CV) on the diastolic interval (DI) that preceded them, DI interval being the window of time between repolarization of an action potential (AP) and activation of the subsequent AP. The causal relationship between DI and APD is such that a small action



potential duration restitution (APDR) slope ( $< 1$ ) will cause APD to approach a steady state value (Figure 1.4 A) while a high slope will result in alternating and increasingly different APD values (Figure 1.4 B) which create an unstable substrate where repolarization alternans at short cycle lengths can create wavebreak and fibrillation [52, 58, 116]. Recent studies, however, have cast doubt on this hypothesis through observation, in *in vivo* human studies, of a high prevalence of APDR greater than 1 in what appears to electrically stable tissues [82]. Panoramic imaging provides a phenomenal tool for looking at restitution dynamics across the entire epicardium to identify regions of high APDR slope and identify whether those regions generate APD alternans at short pacing cycle lengths and whether these regions are more likely to initiate or maintain an arrhythmia.

## 1.4 Dissertation Scope and Procedure

A persistent challenge faced in both investigating and treating cardiac arrhythmias is characterizing microscopic electrophysiological phenomena with what are often low resolution and geometrically discontinuous measurement tools. The development of easily accessible tools that can measure with microscopic resolution at a continuous and macroscopic scale will help make meaningful steps in understanding the dynamics of cardiac arrhythmias. This dissertation encompasses my efforts in two areas of development and one area of application. First, the validation and characterization of a flexible high-resolution active capacitive electrode array. Second, the development of open source panoramic optical mapping with modern technology for studies of small mammal (e.g. mouse, rat, etc.). Finally, the use of panoramic imaging to investigate the validity of action potential duration restitution slope ( $> 1$ ) as an indicator of unstable regions susceptible to wavebreak and reentry.

First, I will conduct experiments with the active capacitive electrode device in an in vitro rabbit model and characterize the resultant signals to validate its utility in experimental and clinical diagnostic applications. Second, I will build and validate a modern panoramic imaging system, as well as develop a set of MATLAB and 3D printing tools that will be made publicly available upon publication. Finally, I will use these tools to investigate APDR dynamics in a rabbit model, specifically looking at the role of APDR maximum slope in the maintenance of ventricular arrhythmias.

# Chapter 2

## Capacitively Coupled Arrays of Multiplexed, Flexible Silicon Transistors for Cardiac Electrophysiology

### 2.1 Abstract

Advanced capabilities in electrical recording are essential to treatment of heart rhythm diseases and to progress in cardiac science. The most advanced technologies using flexible form of integrated electronics, however, pose significant risks arising from penetration of bio-fluids into the underlying electronics and electrochemical reactions at the interface. Here we present a solution to this challenge that uses an ultrathin, leakage-free, biocompatible dielectric layer to completely seal an underlying layer of flexible electronics, where electrophysiology occurs without any direct metal contact. The resulting current leakage levels

are factors of 10,000 smaller and operational lifetimes are between two and three orders of magnitude longer than those of any other related alternative or, more generally, any other flexible electronics technology. Systematic studies with normal, paced, and arrhythmic conditions in Langendorff hearts highlight the capabilities. The results form a realistic pathway towards flexible, biocompatible electronic implants, with potential for broad utility.

## 2.2 Key Terms

biomedical engineering, electrophysiology, materials for devices

## 2.3 Introduction

Tools for spatially mapping electrical activity on the surfaces of the heart are critically important to experimental cardiac electrophysiology and clinical therapy. The earliest systems involved micro-electrode arrays on flat, rigid substrates, with a focus on recording cardiac excitation in cultured cardiomyocytes and mapping signal propagation across planar cardiac slices [19, 49, 85, 100, 106]. More recent technologies exploit flexible arrays, in formats ranging from sheets, to baskets, balloons, socks and integumentary membranes, with the ability to integrate directly across large areas of the epicardium and endocardium in beating hearts [34, 57, 56, 123]. The most sophisticated platforms of this type include an underlying backplane of thin, flexible active electronics that performs local signal amplification and allows for multiplexed addressing [109, 110]. This latter feature is critically important because it enables scaling to high density, high speed measurements, in regimes that lie far beyond those accessible with simple, passively addressed systems without integrated electronics. The

measurement interface associated with all such cases relies on thin electrode pads in direct physical contact with the tissue, where electrical signals transport through via-openings to the electronics. Although this approach has some utility, bio-fluids can readily penetrate through the types of polycrystalline metal films used for the electrodes. Resultant leakage currents from the underlying electronics can cause potentially lethal events such as ventricular fibrillation (VF), and cardiovascular collapse [61, 102]; they also lead to degradation of the Si electronics and catastrophic failure of the measurement hardware. The electrochemical reaction with the electrolyte at the metal/tissue interface will also yield bio-corrosion of metal films [8]. By consequence, devices of with such designs are inherently unsuitable for human use, even in surgical contexts or other acute applications. Similar considerations prevent their application in any class of implant [7, 12, 122].

The results presented here provide a robust and scalable solution to these challenges by eliminating all direct metal interfaces and replacing them with capacitive sensing nodes integrated on high performance, flexible silicon electronic platforms for multiplexed addressing. Specifically, an ultrathin, thermally-grown layer of silicon dioxide covers the entire surface of the system, to serve both as a dielectric to enable direct capacitive coupling to the semi-conducting channels in arrays of silicon nanomembrane (Si NM) transistors and as a robust, biocompatible barrier layer to prevent penetration of bio-fluids. The co-integration of active electronic circuits affords built in signal conditioning and processing, as well as scalability via multiplexed addressing [55, 60, 94, 98, 104, 107, 121]. Although capacitive methods for sensing [20, 35, 125] and rigid platforms of large-scale active microelectrodes [3, 9, 30, 99] are known, our work combines two features that, viewed either individually or collectively, are important advances in technology for electrophysiological mapping at the organ level in living biological systems: (1) use of an ultrathin thermally grown layer of silicon dioxide

for capacitive sensing that simultaneously provides high-yield, defect-free encapsulation layers with chronic stability in bio-fluids; (2) combination of high fidelity capacitive sensing, chronic stability and mechanical flexibility in a fabrication process that yields thin active electronics with robust operation on dynamically evolving curved surfaces of biological tissue, as demonstrated in cardiac mapping on beating hearts. The technology introduced here is the first to incorporate all of the key features needed for use in high speed, high resolution cardiac electrophysiology: (1) large area formats with integrated active electronics for multiplexing and signal amplification on a per channel level, (2) thin, flexible device mechanics for integration and high fidelity measurement on the curved, moving surfaces of the heart, (3) cumulative levels of leakage current to the surrounding tissue that remain well below  $1\ \mu\text{A}$  (per ISO 14708 1:2014 standards for implantable devices), for safe operation, (4) long-lived, thin, bendable bio-fluid barriers as perfect, hermetic sealing of the underlying electronics for stable, reliable function and (5) biocompatible interfaces for chronic use, without direct or indirect contact to traditional electronic materials. Detailed studies of the materials and the combined electrical and mechanical aspects of the designs reveal the key features, and advantages, of this type of system. Application to epicardial mapping of ex vivo Langendorff heart models further quantitatively validates the capabilities in various contexts of clinical relevance. The resulting high levels of safety in operation and long-term, chronically stable measurement capabilities create unique, compelling opportunities in both cardiac science and translational engineering.

## 2.4 Results

### 2.4.1 Capacitively coupled silicon nanomembrane transistors as active sensing nodes

The overall system consists of 396 multiplexed capacitive sensors (18 columns, 22 rows), each with dimensions of  $500\text{ }\mu\text{m} \times 500\text{ }\mu\text{m}$ , as shown in Figure 2.1a, distributed uniformly over a total area of  $9.5\text{ mm} \times 11.5\text{ mm}$ . Each sensor consists of two underlying Si NM transistors, one of which connects to a metal pad from its gate electrode (Figure 2.1a and 2.1b). A layer of thermally grown silicon dioxide (900 nm, SiO<sub>2</sub>) covers the entire top surface of the system (Figure 2.1a). This ultrathin (comparing to the thickness of the layers used previously for encapsulation [18, 31, 97]) thermal SiO<sub>2</sub> layer serves not only as the dielectric for capacitive coupling of adjacent tissue to the semiconducting channels of the associated Si NM transistors, but also as a barrier layer that prevents penetration of bio-fluids to the underlying metal electrode and associated active electronics. The fabrication begins with definition of 792 Si NMOS transistors on a silicon on insulator (SOI) wafer. A sequence of deposition, etching and photolithographic patterning steps forms the necessary dielectric and metal layers for the interconnects and sensing electrodes. Bonding a layer of polyimide on top of this electronics yields a thin, flexible system upon removal of the silicon wafer. Here, the buried oxide (Box) layer of the SOI wafer serves as the capacitive interface and encapsulation layer. Detailed information on the device fabrication can be found in Fang et al. [32] **Methods**, Supplementary note 1 and Supplementary Figure 1. Supplementary Figure 2 and 3 show optical images at various stages of the fabrication and a corresponding cross sectional schematic illustration of the final device, respectively. This fabrication process is capable of scaling up to the largest silicon wafers available (currently 450-mm diameter),

allowing for systems that provides full area coverage across most of the internal organs of the human body.

As presented in the equivalent circuit, top and cross sectional views of Figure 2.1b, each sensor includes an amplifier and a multiplexer, with capacitive input. The amplifier consists of a Si NM transistor (channel length  $L_{\text{eff}} = 13.8 \mu\text{m}$ , width  $W = 80 \mu\text{m}$ , thickness  $t = 50 \text{ nm}$ ), with a gate that extends to a large metal pad ( $270 \mu\text{m} \times 460 \mu\text{m}$ ). The thermal  $\text{SiO}_2$  layer above the transistor and the metal pad physically contacts adjacent tissue during operation. The tissue/ $\text{SiO}_2$ /gate metal pad forms a large capacitor ( $C_{\text{CAP}}$ , tissue/ $\text{SiO}_2$ /gate metal pad) that couples with the gate that drives the transistor channel. This directly couples to the semiconductor channel of the amplifier, bypassing the effects of capacitance in the wiring to remote electronics, as an important distinction between the architecture presented here and traditional, passive capacitive sensors [20, 51]. This direct coupling provides immediate signal amplification and eliminates signal cross-talk along the pathway. Previously reported nanowire bio-sensors [25, 107] rely on similar coupling schemes, although difficulties in scaling prevent their use in the types of large-scale, multiplexed arrays introduced here. The capacitance,  $C_{\text{CAP}}$ , is configured to be over one order of magnitude larger than the top gate capacitance ( $C_{\text{TG}}$ ) of the transistor, thereby prevent forming a voltage divider and attenuating the signal. This design is important for high performance signal amplification and low noise levels [20]. Detailed electrical models of the operation are in the **Methods** section. The sensing system also utilizes an active multiplexing circuitry design similar that described elsewhere [110], where the electrical signal from the tissue at each given node in the array is selected in a rapid time sequence by the multiplexing transistors (with the same dimensions as the amplifier transistor) for external data acquisition. Additional details are in **Methods**.



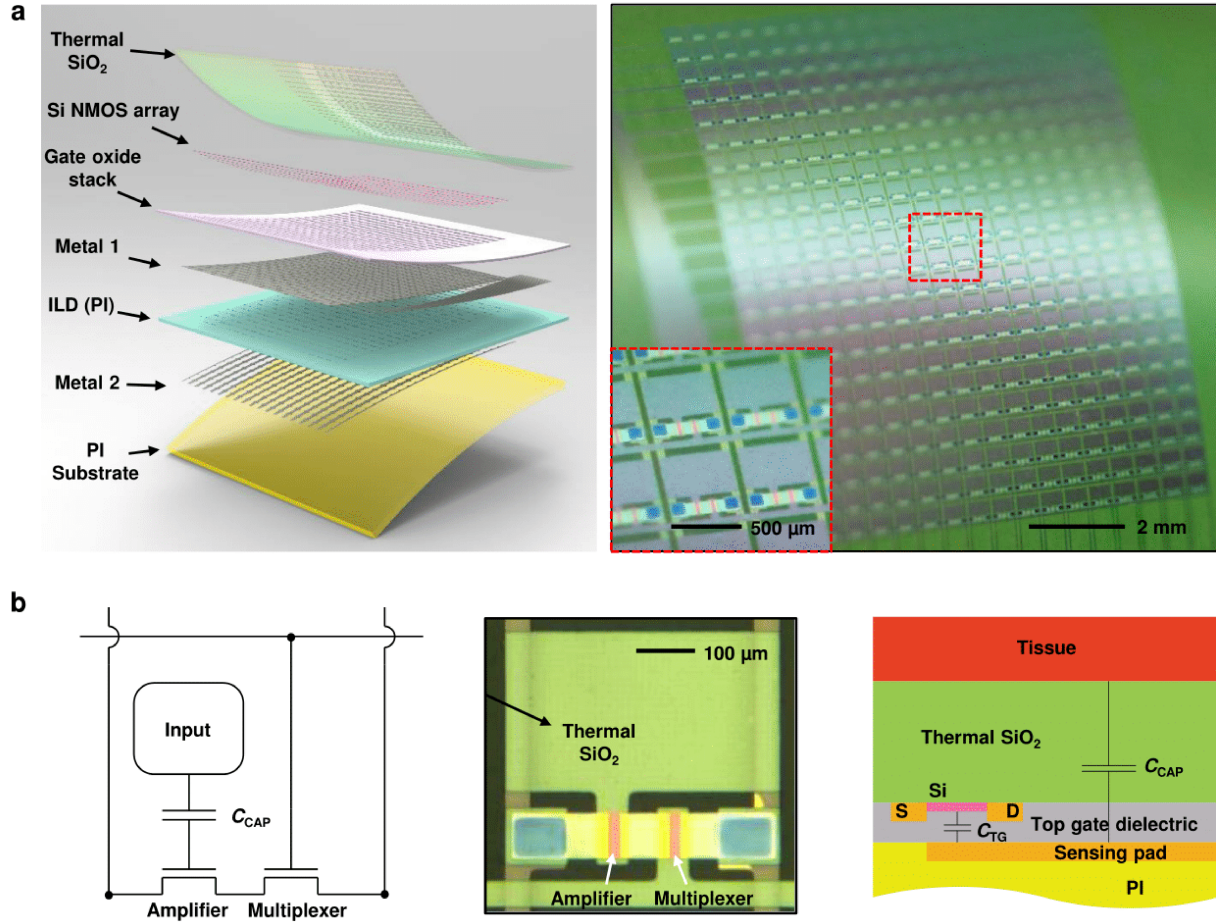


Figure 2.1: **Capacitively coupled silicon nanomembrane transistors (covered by a thermal SiO<sub>2</sub> layer) as active sensing nodes in actively multiplexed flexible electronic system for high resolution electrophysiological mapping.** (a) Exploded-view schematic illustration (left) and a photograph (right) of a completed capacitively-coupled flexible sensing system with 396 nodes in a slightly bend state. The arrows in the left illustration highlight the key functional layers. Inset on the right shows a magnified view of a few nodes. (b) Circuit diagram for a node in this capacitively coupled array, with annotations for each component (left), and an optical microscope image of the cell (middle). A schematic of the circuit cross-section (right) illustrates the mechanism for capacitively coupled sensing through a thermal SiO<sub>2</sub> layer to an underlying transistor.

Figure 2.1c illustrates the principle of the capacitive coupling to a Si NM transistor. Electrically biasing a droplet of phosphate buffered saline (PBS) solution placed in contact with the SiO<sub>2</sub> layer causes coupling to the gate pad of the transistor (while the gate pad was not directly biased), thereby allowing measurement of the transfer characteristic in a manner that simulates the effects of electrical potential generated from the contacting tissue (Figure 2.1c, left and middle). The resulting transconductances, threshold voltages, and subthreshold swings are similar to those measured by directly biasing the gate pad, thereby validating the capacitively coupled sensing design. (The minor discrepancies in the subthreshold swing and transconductance arise from slight differences in the overall capacitance to the channel.) The capacitively coupled transistor exhibits an on/off ratio of  $\sim 10^7$  and a peak effective electron mobility of  $\sim 800 \text{ cm}^2/\text{V.s}$  (Figure 2.1c), as calculated from standard field effect transistor models (see **Methods**). Figure 2.1c (right) shows the output characteristics, consistent with Ohmic source/drain contacts and well-behaved current saturation. This high performance operation is critically important for high fidelity amplification and fast, multiplexed addressing.

The operation and output characteristics of the amplifier appear in Figure 2.1d. Here, a current sink and a single-stage Si NM transistor with capacitively coupled input forms a common drain amplifier (source follower). As a result of the large capacitive coupling, this circuit offers high voltage gain (0.97, where 1 is the ideal value) for both DC (-2 to 2 V) and AC (5 mV, 10 Hz) inputs (Figure 2.1d, right), where the gain corresponds to the ratio between the output and input voltages ( $V_{\text{OUT}}/V_{\text{IN}}$ ). The presence of the thermal SiO<sub>2</sub> layer yields an ultra-high input impedance measurement interface (  $2.6 \text{ G}\Omega$  per sensing node at 10 Hz), and nearly perfect encapsulation of the electronics from the surroundings. This high input impedance at the SiO<sub>2</sub>/tissue interface transfers into a low output impedance ( $\sim 855 \text{ }\Omega$  per sensing node, detailed calculation in **Methods**) via the source follower circuits

current gain. Additional circuit level improvement such as input capacitance neutralization and circuit reference grounding, with reduced thermal SiO<sub>2</sub> thickness can further enhance the recording quality of bio-potentials [33].

Such sensing systems can be constructed with excellent uniformity in electrical responses across all sensing nodes. Figure 2.1e shows a histogram plot of the gain measured on all nodes of a 396-channel sensing matrix; the yield is 100% and the average gain is 0.99 (minimum: 0.9, maximum: 1, with a standard deviation of  $1.12 \times 10^{-4}$ ). The yield here defines the number of working (with gain above 0.6) sensing nodes divided by the total sensing nodes on the array. In testing and ex vivo experiments, the 22 row select signals cycle at 25 kHz, yielding a sampling rate of 1136 Hz per node. This rate can be further increased by improving the multiplexing rate in the back-end data acquisition (DAQ) system.

### 2.4.2 *In vitro* assessment of electrical performance

The performance of the capacitively coupled active sensing nodes is stable across a broad time dynamic range. Figure 2.2a shows high gain, low noise measurements for input signal frequencies between 0.1 and 100 Hz, with similar or better performance than simple, directly coupled metal sensing interfaces. The power spectral density (PSD) of the output signal, computed from the Fourier transform of the auto-correlation function, describes its frequency behavior. As an example, the PSD of the noise (Figure 2.2b, when measuring with a 5 mV, 10 Hz sine-wave input) indicates expected  $\sim 1/f$  behavior at low frequencies, consistent with circuit models (see Methods). Figure 2.2c displays a 396-channel sensing system with mean noise as low as  $\sim 55 \mu\text{V}$  and SNR over 42 dB, and excellent uniformity across the entire device. The transistor mobility, the sensing node gain, and the array yield are also superior,

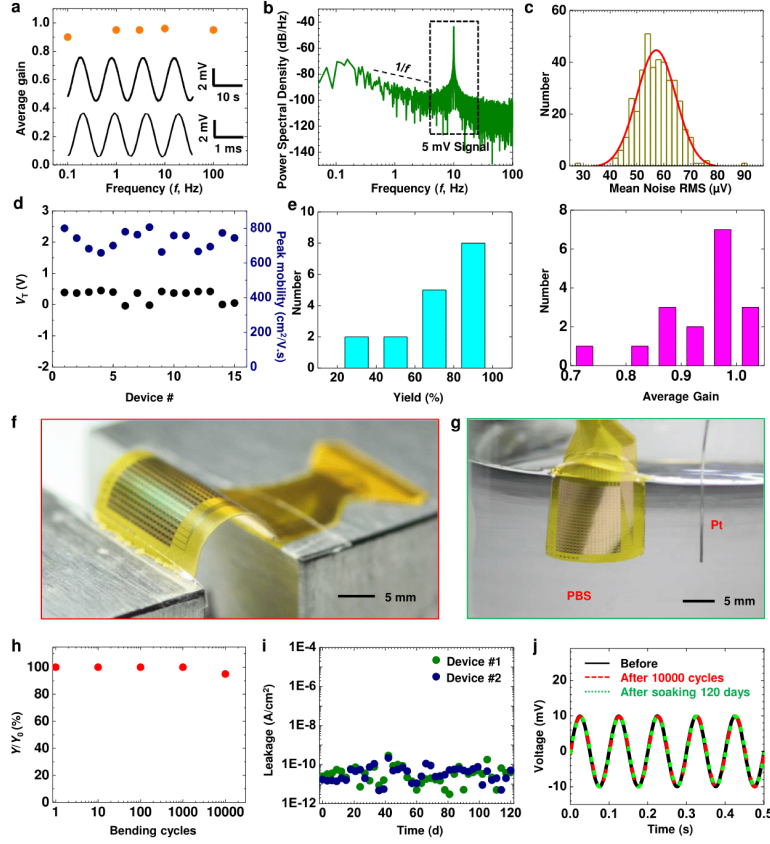


Figure 2.2: **In vitro assessment of electrical performance.** (a) Average gain of a representative capacitively coupled transistor as a function of the input frequency ( $f$ ) from 0.1 to 100 Hz. Inset shows the responses from this sensor node at 0.1 Hz (top) and 100 Hz (bottom), after band-pass filtering (0.05-568 Hz). (b) Power spectral density of a 5 mV AC signal at 10 Hz measured at a representative node, showing a typical  $1/f$  relationship at low frequency. The input was a sine-wave of 5 mV at 10 Hz. (c) Histograms of noise (with Gaussian fitting) measured from all 396 nodes of the device in Fig. 1c. (d) Statistics of the threshold voltage ( $V_T$ ) and peak effective mobility ( $\mu_{eff}$ ) of test transistors from 15 different arrays. (e) Statistics of yield (left) and gain (right) of 17 capacitively coupled, active sensing 18x22 electrode array. (f) Image of a device during a mechanical bending test. (g) Image of a device completely immersed in a saline solution, during a soak test. (h) Yield ( $Y$ , defined as the number of working nodes divided by the total number of nodes) as a function of cycles of bending to 5 mm bend radius, showing minimal changes up to 10000 cycles. (i) Electrical leakage current of 2 devices during soak testing. Minimal leakage appears over a period of 120 days at 37 °C. (j) Response of a representative node to a sine wave input (at 10 Hz) before, after 10000 cycles bending, and after saline immersion for 120 days.

likely due to the better interface from Si and thermal SiO<sub>2</sub>. Statistics on the test transistor threshold voltage, mobility, array yield and average gain from different devices show very small sample to sample and batch to batch variations (Figure 2.2d and 2.2e). Mechanical bending tests and *in vitro* soak tests highlight the flexibility and robustness of the system (Figure 2.2f and 2.2g). The device performance remains unchanged in the bent state and does not vary after bending to a radius of 5 mm for 1, 10, 100, 1000, and 10000 cycles (Figure 2.2h).

The system also demonstrates outstanding stability of continuous operation when completely immersed in saline solution and bio-fluids, due to the thermal SiO<sub>2</sub> encapsulation. Figure 2.2g depicts the set-up for the soak test, where phosphate-buffered saline (PBS) solution simulates the cardiac bio-fluid. Evaluations involve application of a 3 V DC bias between the sensing system and a Pt reference electrode throughout the test, at a temperature of 37 °C. The leakage current remains lower than 10<sup>-9</sup> A/cm<sup>2</sup> for at least 120 days (measured up to date) for two devices (Figure 2.2i). Figure 2.2j shows the device response to a 10-Hz sine wave input, before and after the bending and soaking experiments. All indications are consistent with reliable, invariant operation associated with conditions that mimic those for *in vivo* cardiac applications. The most compelling demonstrations are in leakage levels that are factors of 10,000 smaller than those of previous related cardiac mapping technologies (factors of 1000 smaller than the standard of safety limit for active implantable medical device in ISO 14708 1:2014, 1  $\mu$ A). Compared to previously reported devices with lifetimes of only a few hours in soak tests [109], the operational lifetimes here are between two and three orders of magnitude longer, with interfaces that consist of a uniform layer of a well-established material (thermal silicon dioxide) in traditional implants. This unprecedented device longevity highlights the pin hole free nature and robustness of the thermal SiO<sub>2</sub> layer, which is unachievable with films deposited using conventional methods.

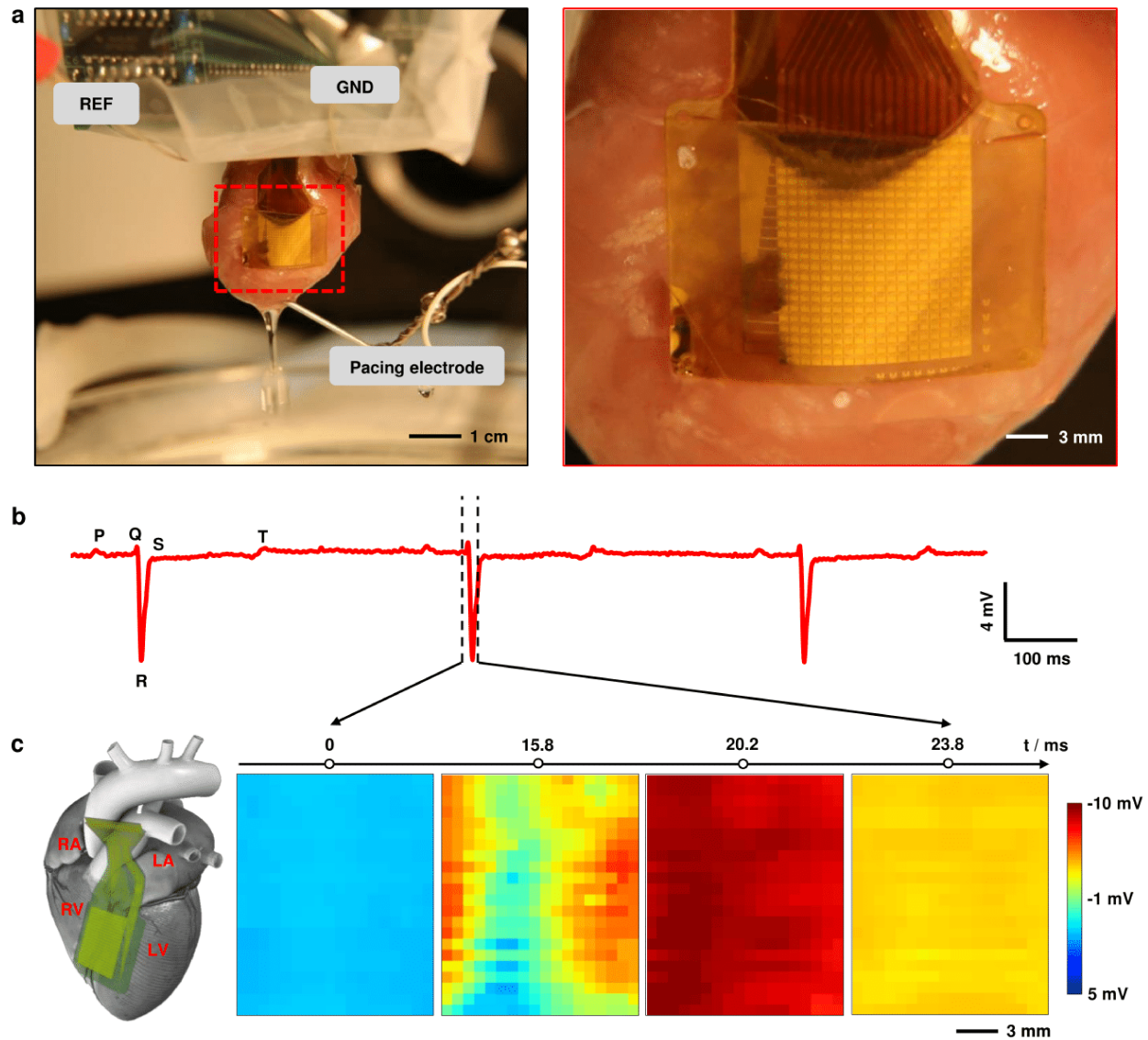


Figure 2.3: **High density cardiac electrophysiological mapping on ex vivo rabbit heart models.** (a) A photograph of a flexible capacitive coupled sensing electronic system on a Langendorff-perfused rabbit heart (left). Magnified view, showing conformal contact of the device to the cardiac tissue, via the action of surface tension (right). (b) Representative single voltage trace from the electrode array without external pacing. Signatures related to the P, Q, R, S, and T waves in ECG traces, can be identified from the recordings. (c) Representative voltage data for all electrodes at four time points (indicated in B), showing normal cardiac wave-front propagation. The progress of the cardiac wave is consistent with the physical location of the array on heart, as illustrated in the diagram on the left (RA, LA, RV and LV stands for right atrium, left atrium, right ventricle, and left ventricle respectively).



### 2.4.3 Cardiac mapping in animal heart models

Experiments that validate the function involve recording of unipolar voltage signals from all 396 nodes on multiple ex-vivo Langendorff perfused rabbit hearts [62]. Figure 2.3a shows a system placed on the anterior aspect of the heart with equal overlap on the right and left ventricles. The device conformally covers the curvilinear surface of the heart. Although capillary forces associated with the moist cardiac surface can fixate the device in place, the use of a thin PVC film wrapped around the heart further enhanced the robustness of the mechanical coupling. Samples of representative single node voltage tracings during sinus rhythm are in Figure 2.3b. Clear components, similar to the P wave, QRS complex, and T wave in clinical ECG recordings, are apparent. The low noise levels of are consistent with the in vitro results. The average heart beats at  $\sim 125$  beats per minute. Attaching the device on heart does not interfere with the heart's rhythm, based on experimental observations (Figure 2.4). The slowing of the sinus rhythm rate can be attributed to normal heart deterioration that results from the use of a blood substitute in the ex vivo Langendorff perfused model. High definition spatial temporal electrophysiology mapping results from plotting the signals from all 396 nodes as a function of time. Spatial voltage maps of all nodes at four sequential time points appear in Figure 2.3c, corresponding to phase 4 to phase 1 in the cardiac action potential (dashed lines in Figure 2.3b illustrate the time window where Figure 2.3c is taken). The wave of cardiac activation approaches the center of the anterior aspect of the heart from both the left and right sides, which matches well the physical location of the device. The extracted conduction velocities ( $0.9506 \pm 0.3340$  mm ms<sup>-1</sup>) are close to values inferred from optical data ( $0.8124 \pm 0.3438$  mm ms<sup>-1</sup>) as described in the following, for the 300 ms cycle length (Figure 2.5).



Figure 2.4: **Signal morphology unaffected by experimental conditions.** Voltage traces from the same channel in the capacitively coupled sensing electronic system at the beginning and end of an *ex vivo* Langendorff perfused rabbit heart experiment. The amplitude and noise levels of the signal remain the same, demonstrating the stability of capacitive sensing over the entire course of the *ex vivo* experiment.

This technology platform shows promise not only for *ex vivo* cardiac applications, but also for *in vivo* implantation. Briefly, we performed *in vivo* measurements in an open chest canine preparation (Figure 2.6a). A cocktail of midazolam, butorphanol, and ketamine anesthetized the animal. Isoflurane subsequently maintained surgical plane level anesthesia. A sternal thoracotomy opened the ribcage and exposed the thoracic cavity. An incision in the pericardium allowed access to the heart, while maintaining the structural support provided by the remainder of the pericardium. We placed the electrode array on the basal free wall of the left ventricle during sinus rhythm. We acquired data in two-minute intervals and subsequently analyzed the resultant patterns of activation (Figure 2.6b).

#### 2.4.4 Comparison of fluorescence imaging

The optical transparency of the system in the spaces between the metal electrodes and transistors allows validation of electrical measurements by means of simultaneous optical mapping [28]. In particular, comparison of electrical and optical recordings provides a robust method



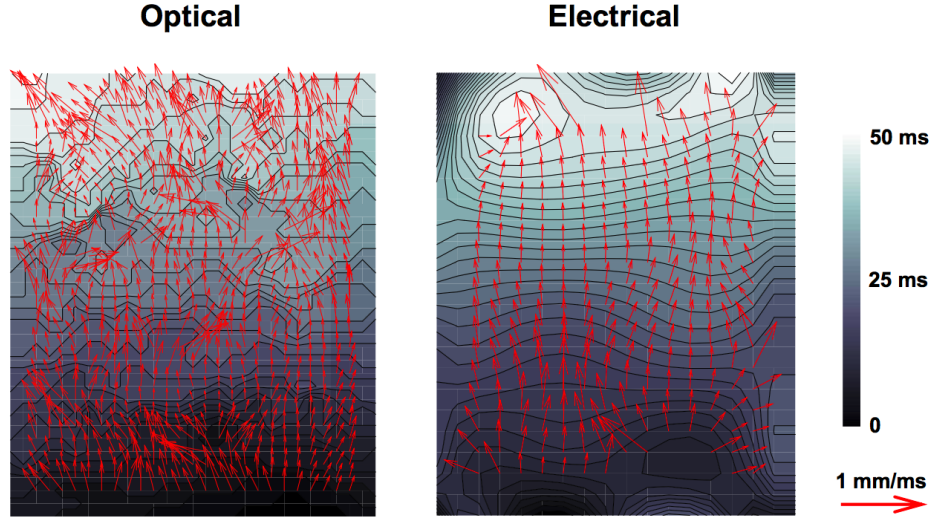


Figure 2.5: **Comparison of Conduction Velocity** Calculated conduction velocity vector from optical and electrical maps at pacing of 300 ms cycle length. The magnitude of the red arrows indicates the amplitude of the velocity. The background maps are activation in grayscale.

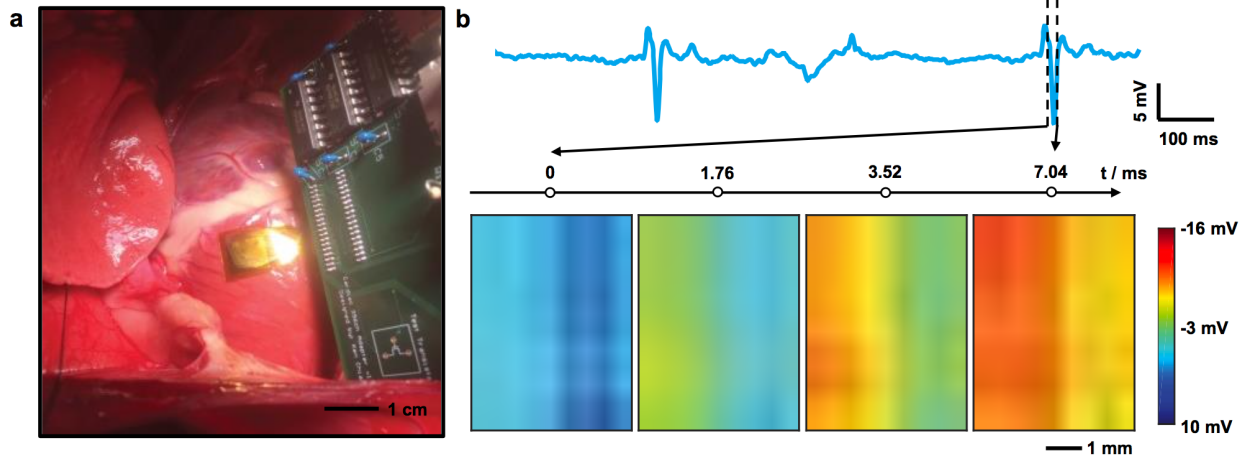


Figure 2.6: **In Vivo Recordings.** *In vivo* recording using a capacitively coupled sensing electronic system from a beating heart. (a) A photograph of a device laminated onto the left ventricle of a beating heart in an open chest experiment on a canine model. (b) Representative single voltage trace from the device (top), with representative voltage data map at four time points, showing normal cardiac wave-front propagation (bottom).

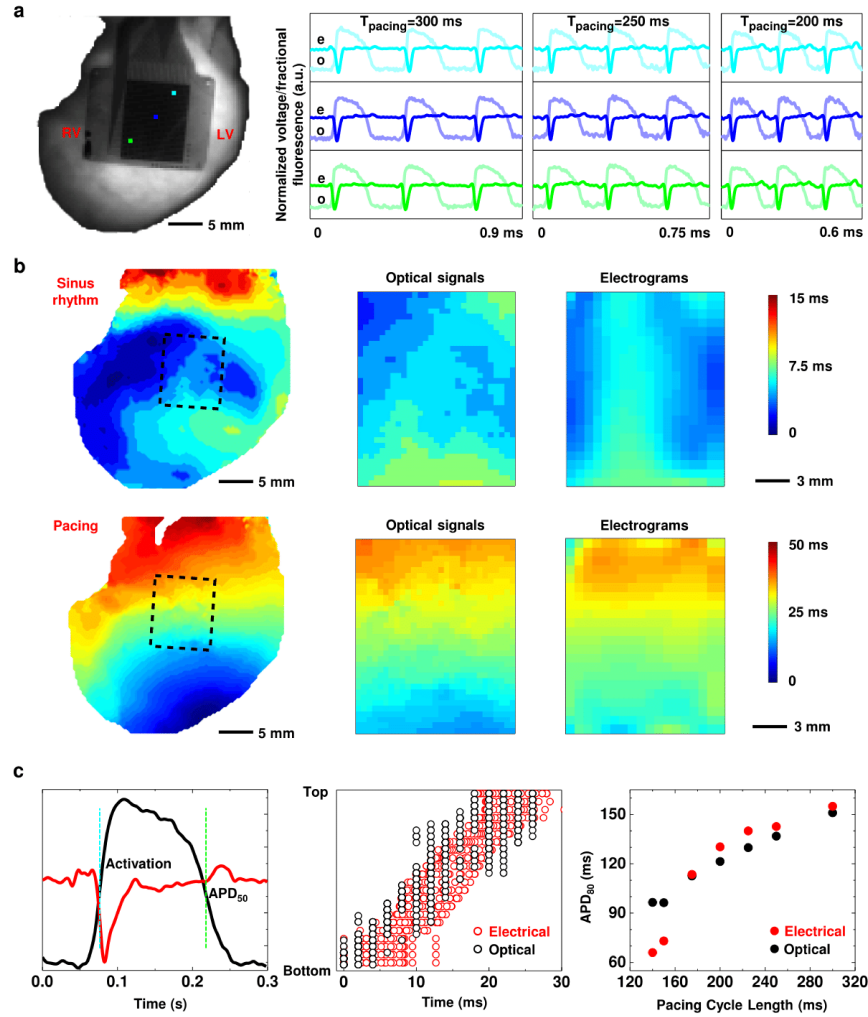
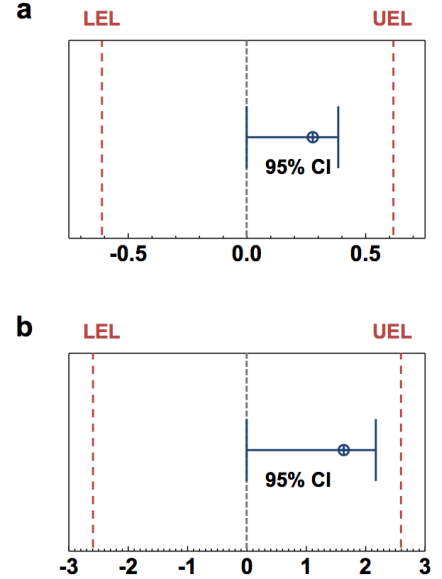


Figure 2.7: **Comparison of electrical mapping with optical fluorescence recording.** (a) Representative electrical and optical signals captured simultaneously on a Langendorff-perfused rabbit heart at multiple cycle lengths (300, 250, and 200 ms). (b) Interpolated spatial activation maps derived from these data. Top row shows activation as measured during sinus rhythm. The bottom row corresponds to 300 ms ventricular pacing. The activation maps from left to right are optical signals from the whole heart, optical signals from the device area, and electrical signals respectively. The dashed boxes in the whole heart illustrations depict the device area. (c) Comparison of activation and repolarization measurements in a single simultaneously measured electrical and optical signals. Left figure highlights a quantitative comparison of electrical and optical signals during one depolarization/repolarization cycle. Center figure shows the comparison of activation times measured across all electronic nodes and corresponding optical field of view. Right figure shows the comparison of optical and electrical restitution curves measured at various cycle lengths (300, 250, 225, 200, 175 ms).

**Figure 2.8: Comparison of Optical and Electrical Signals.** Sample equivalence test between the electrical and optical recordings. In order to demonstrate the accuracy of the bioelectric signals measured by the electrode a two sample equivalency test was performed using the electrode measurements as the test data and the optical measurements as the reference data. In the case of both (a) sinus rhythm and (b) 300 ms ventricular pacing, the isochronal maps of activation were found to be equivalent ( $p < 0.05$ ) for both upper and lower bounds. Here the CI, LEL, UEL stand for confidence interval, lower equivalence limit and upper equivalence limit respectively.



for establishing morphological criteria for phenomenon like activation and repolarization. Figure 2.7a shows a three-beat comparison of optical and electrical signals at three distinct pacing cycle lengths. Representative optical action potentials show an adequate SNR for this comparison despite the dense nature of the sensing circuits. Interpolated activation maps of both data types reveal a strong association during both sinus rhythm (Figure 2.7b, top) and pacing (Figure 2.7b, bottom). Close observation (Figure 2.7c, left) of the two signals types indicates a close correspondence of key morphologies associated with activation (QRS complex in electrogram vs.  $(dV/dt)_{max}$  in optical signal, where  $V$  is the optical signal, and  $t$  is the time) and repolarization (T wave in electrogram vs.  $APD_{90}$  in optical signal, where  $APD_{90}$  stands for the action potential duration at 90% of repolarization). Strong correlations in activation (Figure 2.7c, middle) and repolarization (Figure 2.7c, right) are also apparent. The electrical and optical recordings also demonstrate good accuracy as demonstrated via a two sample equivalency test (Figure 2.8).

### 2.4.5 Study of ventricular fibrillation

Previously reported flexible passive electrode arrays lacked sufficient spatial density to map and reconstruct patterns of activity associated with VF [123]. The capacitive high-density sensing electronics presented here overcome this limitation, to allow reliable tracking of reentrant patterns of activation (Figure 2.9a and 2.9b, top). Calculation of the signal phase values (Figure 2.9b, bottom), a common clinical method for assessing arrhythmias, corroborates these observations. Detecting a singularity in the phase map can identify a reentrant pattern of activation. This singularity is a location around which all values of phase from  $-\pi$  to  $\pi$  are represented [10, 27, 91] and can be seen in the first frame of the top two rows of Figure 2.9b. In clinical practice, the identification of phase singularities is commonly used to guide ablation therapy of arrhythmias[79, 67]. The location of the phase singularity in each frame (Figure 2.9b bottom) can be calculated using the methodology set forth by Bray et al [15]. The phase singularity is the most positive point on the map that wanders within the bottom right quadrant as the wave of activation passes through a single reentrant pattern. In a single second of recorded data six such reentrant patterns occur, with an average duration of  $8.089 \pm 2.734$  ms. This demonstration has significant implications for use of the electrode in diagnostic catheters and implantable devices aimed at treating patients with life threatening atrial and ventricular arrhythmias.

## 2.5 Discussion

The results presented here demonstrate a promising route toward safe, robust and high performance flexible electronics for high-density cardiac mapping in both clinical and research settings. Devices with larger area coverages and/or higher density can be readily achieved

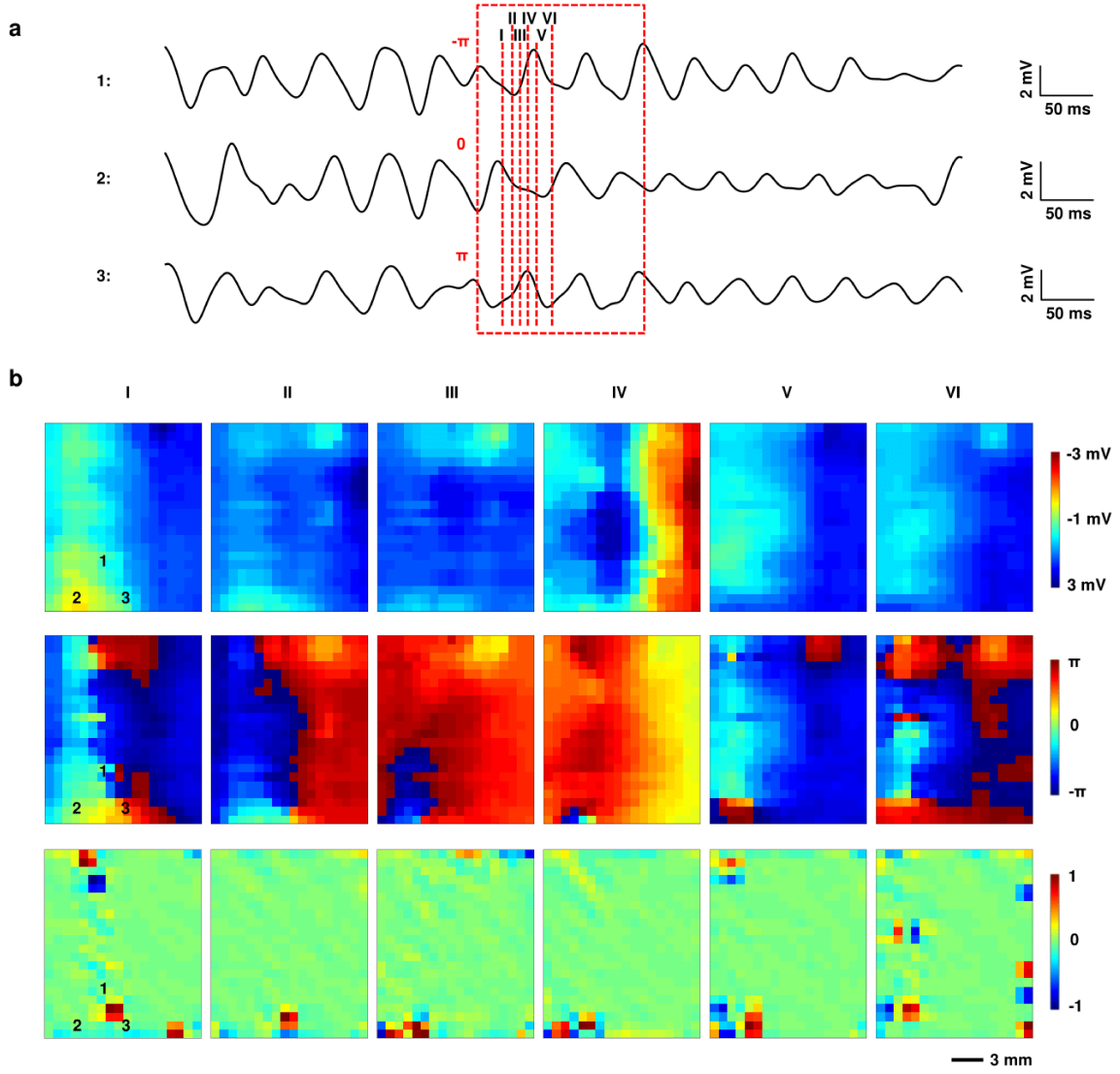


Figure 2.9: **Study of ventricular fibrillation (VF).** (a) Three representative electronic node signals taken from a heart during VF. The dashed box specifies the window of time corresponding to two reentrant cycles of VF. The labels  $-\pi$ ,  $0$ , and  $+\pi$  indicate the initial phase values of the respective signals at the beginning of the reentrant cycle. (b) Voltage, phase and phase singularity maps at six time points corresponding to the dash lines specified in (a). Number 1, 2, and 3 on the maps mark the locations where the signals in (a) were taken. Voltage and phase data indicate a reentrant cycle of VF. A phase singularity commonly refers to a point on a phase map around which all values of phase (i.e.  $-\pi$  to  $+\pi$ ) are represented. The phase singularities are identified as the  $\pm 1$  values associated with regions of the phase map where this occurs. Optical signals from the sensing electronics area also match well with electrical recordings

through scaling the same basic materials and architectures, in a way that leverages advanced processing techniques from the integrated circuit and information display industries. We see no fundamental hurdles, for example, in achieving systems with thousands or even hundreds of thousands of nodes. Autocorrelation methods can be used to identify the node spacing that will maximize acquisition of electrophysiological data while reducing unnecessary redundancy. Future efforts have the potential to yield advanced, stretchable variants of these kinds of systems, to allow coverage across the entire epicardium in a pericardium-like membrane or the entire endocardium by integrating the electronics on balloon catheters. Parallel efforts should also focus on mitigating the foreign body response from these flexible electronic systems. Though minimally invasive, in certain scenarios the devices could potentially induce inflammatory responses that could result in fibrotic tissue and associated impairment of the capacitive measurement interface [76, 81, 108, 114]. The addition of triazole modified hydrogels [108] and/or anti-inflammatory agents [76] could help to minimize such effects.

While the current work focuses on electrical sensing, energy delivery capabilities could stem from developing high definition capacitively coupled pace-making stimulators. In distinct contrast with optical mapping, the combination of actuators and sensing electrodes both using a capacitively coupled approach has the potential to enable clinically safe systems capable of diagnosing and treating patients with life threatening arrhythmias in real time. In addition, many sudden cardiac deaths occur due to abnormal repolarization caused by mutations in various genes, encoding ion channels governing repolarization. Lack of adequate technology to map repolarization has been a major obstacle in studies of so called long QT syndrome and short QT syndrome, which refer to duration of QT interval of electrocardiogram. The device platforms introduced in our manuscript provide a solution that is key to advancing research, diagnostics and treatment of these lethal cardiac syndromes. Future and on-going work focuses on the engineering development of power supply, data processing units

and data transmission interfaces for long-term recording in vivo, achieving systems beyond the realm of what can be envisioned from optical mapping and conventional multielectrode arrays.

## 2.6 Methods

### 2.6.1 Capacitively coupled active sensing node design

The basic node of the capacitively coupled, active sensing electronics consists of an NMOS source-follower amplifier with a capacitance input and an on-site NMOS multiplexer (Figure 2.1b). The area of the sensing pad is sufficiently large such that the capacitance between the sensing pad and the tissue is over one order of magnitude higher than the gate capacitance of the sensing transistor. For the 396-ch flexible Si active sensing electronic system in this study, the area of the sensing pad is  $270\ \mu\text{m} \times 460\ \mu\text{m}$ , while the transistor gate area is  $13.8\ \mu\text{m} \times 80\ \mu\text{m}$ . From a thin film capacitor,  $C = \epsilon_r \epsilon_0 A/t$  where  $\epsilon_r$  is the relative permittivity,  $\epsilon_0$  is the vacuum permittivity,  $A$  is the area of the capacitor and  $t$  is the thickness of the dielectric,  $C_{\text{CAP}} = 12.5C_{\text{TG}}$ . The total capacitance ( $C_{\text{T}}$ ) driving the Si NM channel in the amplifier transistor yields  $\sim 0.93C_{\text{TG}}$ , from combining  $C_{\text{CAP}}$  and  $C_{\text{TG}}$  in series. During sensing, the amplifier transistor operates in saturation (active mode). The transconductance ( $g_m$ ) can be extracted from the standard Square-Law model with the following equation,

$$g_m = \frac{\partial I_{\text{DS}}}{\partial V_{\text{GS}}} = \sqrt{2I_{\text{DS}}\mu_{\text{eff}}C_{\text{OX}}\frac{W}{L_{\text{eff}}}} \quad (2.1)$$

where  $\mu_{eff}$  is the effective mobility of electrons in the Si nanomembrane transistor and  $C_{OX}$  is the specific capacitance of the gate per unit gating area ( $C_T/WL_{eff}$ ). This high capacitance design can ensure high transconductance, which yields high gain and low output impedance from the amplifier.

The source input referred noise ( $\nu_{n,rms}$ , root-mean-squared) of the amplifier circuit can be characterized from the following analytical model [20]:

$$\nu_{n,rms}^2 = \frac{(g_{CAP} + g_i)^2 + \omega^2(C_{CAP} + C_i + C_s)^2}{g_{CAP}^2 + \omega^2 C_{CAP}^2} \nu_{i,rms}^2 + \frac{1}{g_{CAP}^2 + \omega^2 C_{CAP}^2} i_{i,rms}^2 \quad (2.2)$$

where  $\nu_i(j\omega)$  is the input referred amplifier voltage noise ( $\omega = 2\pi f$ ),  $i_i(j\omega)$  is the net current noise at the amplifier input,  $g_{CAP} + j\omega C_{CAP}$  is the tissue-electrode coupling admittance, and  $g_i + j\omega C_i$  is the amplifier input admittance, and the  $C_s$  is the active shield to electrode capacitance. This model clearly shows that high coupling capacitance is beneficial in achieving low-noise circuits. In the low frequency limit, the noise power density can be simplified to  $\sim 1/f^\alpha$ , where  $0 < \alpha < 2$ . An active shielding circuit further improves the recording gain and the SNR of the sensing. Here, each column input includes an adjustable active shield drive voltage, adjustable column bias current and an adjustable compliance voltage to limit the peak voltage on the column lines. The row select positive and negative voltages are also fully adjustable.



## 2.6.2 Device Fabrication

The fabrication began with grinding a p-type silicon-on-insulator (SOI) wafer (200-nm-thick Si layer, 1000-nm-thick Box layer, and 500- $\mu\text{m}$ -thick Si handle wafer, Soitec) to 200  $\mu\text{m}$  (Syagrus Systems). A 200-nm-thick layer of silicon dioxide grown at 1150 °C in a tube furnace served as a diffusion mask. Cleaning the wafer by RCA preceded high-temperature processing, including oxidation and doping. Conventional photolithography defined doping regions, followed by reactive ion etching (RIE) with  $\text{CF}_4/\text{O}_2$ . The diffusion of phosphorous occurred at 1000 oC in a tube furnace. Photolithography and RIE with  $\text{SF}_6$  isolated the source, drain, and channel regions of the Si. Tube furnace growth (1150 °C for 37 min) and Atomic Layer Deposition (ALD) yielded a gate oxide stack of silicon dioxide (100 nm) and  $\text{Al}_2\text{O}_3$  (15 nm). Buffered oxide etchant opened the contact regions for source and drain through photolithographically defined patterns of resist. Electron-beam evaporation yielded a layer of Cr/Au (5 nm/100 nm for the first metal layer; 10 nm/500 nm for the second), patterned by photolithography and wet etching to define the gate electrodes and metal interconnects. An interlayer of polyimide (PI; thickness of 1.6  $\mu\text{m}$ ) separated the metal layers. Connections between layers involved through holes defined by lithographically patterned exposure to RIE with  $\text{O}_2$ . Another coating of PI (thickness of 2  $\mu\text{m}$ ) isolated the second layer of metal. A layer of  $\text{Al}_2\text{O}_3$  (20 nm) coated this top PI surface. Separately, a PI film (Kapton; thickness of 13  $\mu\text{m}$ ) laminated on a glass substrate with a thin layer of cured poly(dimethylsiloxane) (PDMS) as a soft adhesive served as a handling substrate. Electron-beam evaporation formed a layer of Ti/ $\text{SiO}_2$  (5 nm/100 nm) on the Kapton film to facilitating bonding with an adhesive (Kwik-Sil, World Precision Instruments) to the devices. Bonding involved placing the device, with PI side facing down, onto the Kapton side, and

applying  $\sim 50$  kPa of pressure. Curing of the adhesive occurred at room temperature within 30 min.

Removal of the Si substrate began with exposure to RIE with  $\text{SF}_6$ , followed by Inductively Coupled Plasma Reactive Ion Etching (STS ICP-RIE). The high selectivity of etching of Si over  $\text{SiO}_2$  in the ICP-RIE prevented any significant removal of the Box layer during this process. Photolithography then defined areas for forming openings for contact leads via RIE with  $\text{CF}_4/\text{O}_2$  and buffered oxide etching. Finally, a laser-cutting procedure defined outer perimeter of the device, thereby allowing it to be peeled from the handling substrate. A Kapton stiffener ( $\sim 150\text{-}\mu\text{m}$ -thick) reinforced the backside of the contact region, to allow mounting of ZIF (zero-insertion-force) connectors as interfaces to the external data acquisition (DAQ) system.

### 2.6.3 Data acquisition

The electrical data acquisition (DAQ) system consists of a set of five PXI-6289 data acquisition cards (National Instruments) and a custom acquisition system interface board (Figure 2.10). The DAQ connects to the multiplexed arrays using flexible HDMI cables and an adapter PCB. The adapter PCB joins to the electrode interface PCB using two  $150\text{ }\mu\text{m}$  pitch connectors. The electrode interface PCB adapts from the ZIF connector used on the electrode array to a more durable connector that can be plugged and unplugged without damage (Figure 2.11). Custom LabVIEW software (National Instruments) controls the DAQ system. All recordings in this study used an over-sampling ratio of 4 to further reduce the noise. The optical mapping involved a sampling frequency of 1 kHz. A triggered TTL

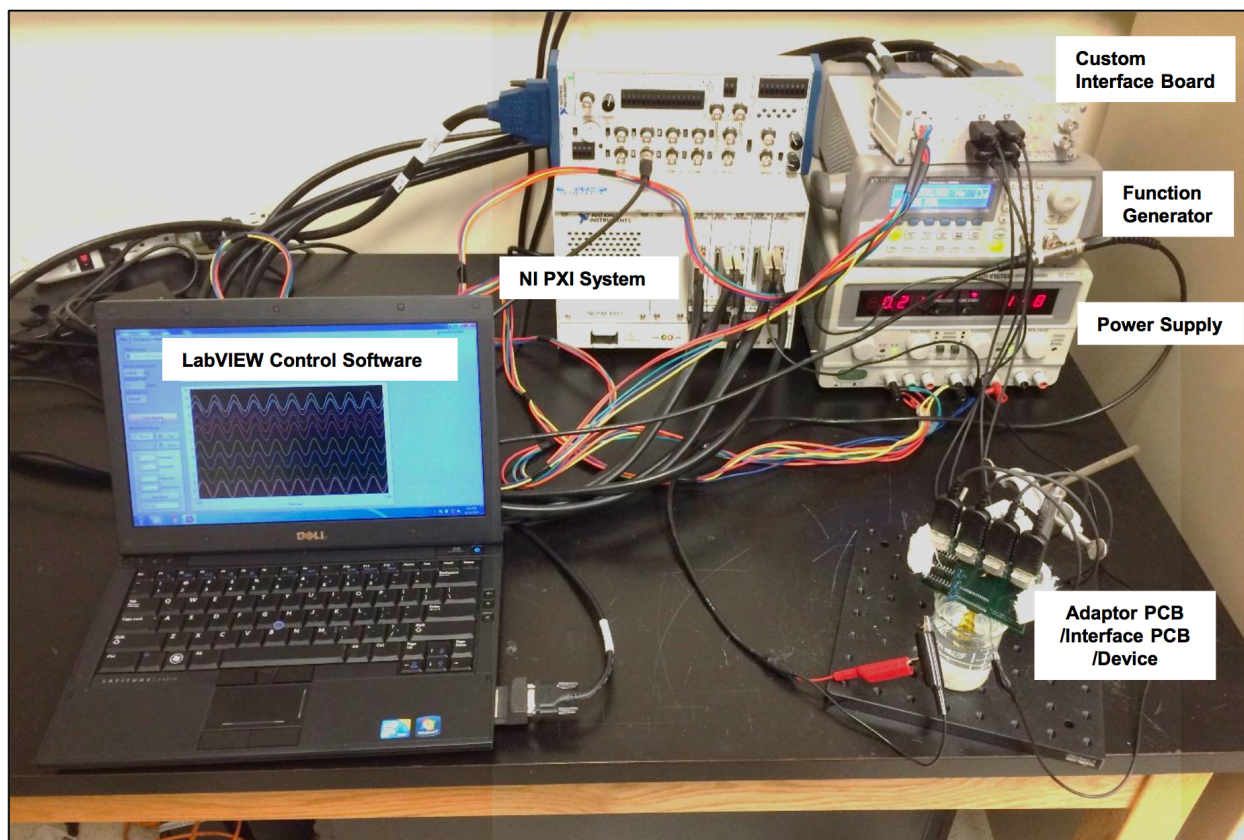
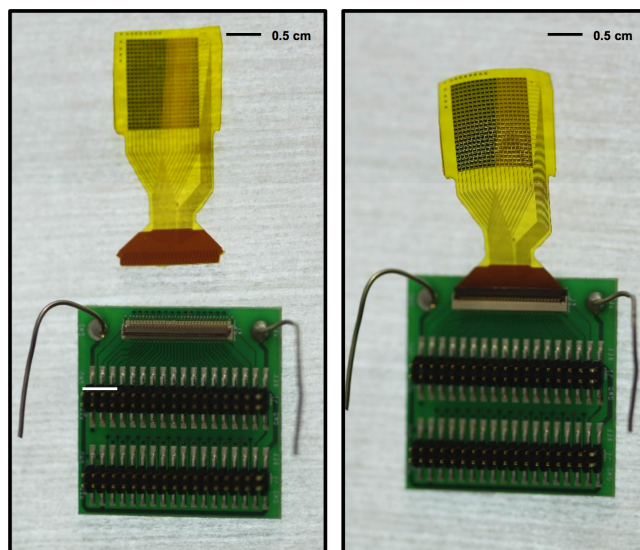


Figure 2.10: **Electrode Data Acquisition System.** A Photograph of the data acquisition system with the electrode array during in vitro bench testing.

Figure 2.11: **Electrode Array and Connector.** Photographs of an electrode array before (left) and after (right) being inserted into an interface PCB board through a zero- insertion-force (ZIF) connector.



pulse aligned the optical signal to electrical data through a direct input of this pulse into the DAQ.

#### **2.6.4 Signal processing**

MATLAB software (MathWorks) enabled offline filtering and analysis. Unless otherwise specified, electrical data from all channels passed through a notch filter at 60-Hz and a (1 Hz, 150Hz) band-pass filter. Calculation of the latency of the peak of each channel yielded the minimum latency, for the isochronal maps. Interpolated signals with a 16x enhancement of the sampling mesh allowed accurate location of peaks on a cubic-spline. A final channel mask, also applied based on the amplitude of the peak, eliminating spurious delays.

#### **2.6.5 Animal experiments**

The experiments were conducted in accordance with the ethical guidelines of the National Institutes of Health and with the approval of the Institutional Animal Care and Use Committee of the George Washington University in Washington DC. Six adult male New Zealand White rabbits were used over the course of device validation. No randomization or blinding was used since there was only a single group. Representative data from the final two experiments are presented here. Briefly, we injected 400 USP units  $\text{kg}^{-1}$  of sodium heparin via a lateral ear vein into the rabbit. Afterwards, a progression of 1%-3% isoflurane delivered via facemask anesthetized the rabbit. Once the animal was unconscious and unresponsive to pain, a midsternal incision removed the heart and the aorta cannulated to facilitate retrograde perfusion of oxygenated Tyrode's solution. The perfusate served as a blood substitute

for the heart to maintain its electrolyte balance and deliver an energy substrate for continued cardiac function. The solution was at a constant physiologic temperature ( $37\pm 1^\circ\text{C}$ ) and  $\text{pH}(7.4\pm 0.05)$  throughout the experiment. The heart was continuously under a constant pressure of 60-80 mm Hg with oxygenated Tyrode’s solution. We administered the excitation-contraction uncoupler Blebbistatin (Cayman Chemical, Ann Arbor, MI) to limit motion artifact in the optical mapping signals. A bolus injection of di-4 ANEPPS (Life Technologies, Grand Island, NY, USA) facilitated fluorescent measurement of membrane potential ( $V_m$ ). A plastic band wrapped the active cardiac sensing array and extended around the heart, facilitating mechanical conformity by capillary force from the moisturized heart surface. The data acquisition system connected with PCB board to the array and performed data acquisition. For optical mapping, A 520 nm excitation light elicited optical action potentials and a CMOS camera (SciMedia Ltd, Costa Mesa, CA, USA) recorded them with a long pass emission filter with a 650 nm cutoff. Finally, to induce VF in a rabbit model, we administered a 20 nM ATP-dependent potassium channel opener pinacidil (Sigma-Aldrich, St. Louis, MO, USA) to shorten action potential duration and create a substrate for induction of VF. Optical data was analyzed using a custom MATLAB software that can be downloaded from <http://www.efimovlab.org/research/resources>.

## 2.7 Acknowledgements

Hui Fang and Ki Jun Yu from University of Illinois Urbana-Champaign did all of the bench top testing of the electrode performance. Zijian Yang and Jianing Zhao, also of University of Illinois Urbana-Champaign, helped with the animal experiments. Michael Trumpis helped with data analysis.

# Chapter 3

## Improved Panoramic Imaging for Small Mammal Hearts

### 3.1 Abstract

In the early 2000s there was a concentrated effort to extend the benefits of fluorescence imaging of explanted hearts (i.e. optical mapping) to the entirety of the epicardial surface. The resulting experimental systems made it possible to record electrophysiological data via optical mapping and project that data onto geometric reconstructions derived from the same heart. As a result, numerous studies were done investigating the nature of ventricular arrhythmias and novel methods of defibrillation. In the last decade and a half both the quality and accessibility of imaging technology have increased. In light of this, we found it necessary to both update our panoramic imaging system and provide an open source solution for analyzing the resulting data.

## 3.2 Key Terms

panoramic imaging, optical mapping, electrophysiology, 3D printing, arrhythmia

## 3.3 Introduction

Optical mapping is a fluorescence based imaging modality which uses parameter specific probes to characterize cellular and tissue level physiological phenomenon like membrane potential [93, 26, 28]. It has been used to great effect in studies of cardiac electrophysiology due to high spatial and temporal resolution, immunity to stimulation artifacts, and the ability to measure multiple parameters simultaneously. Most recently, we have shown that it is also an effective tool for validating novel epicardial interfacing device designs [123, 41, 32].

While many physiological questions can be answered using a monocular setup, there are some that necessitate a whole surface approach to data acquisition. Of particular relevance are ventricular and atrial arrhythmias. It has been observed that meandering reentrant rotors of activity perpetuate arrhythmias [24, 89]. Assessment of these rotors of activity would be limited to those localized in the monocular view that do not meander outside the field of view. In order to accurately track and assess these phenomena, it is necessary to both visualize the entirety of the heart surface and eliminate discontinuities in the data by projecting data onto a representative geometry.

This concept was first proposed and attempted by Lin and Wikswo [68] who started by simply mapping the heart from positions equally spaced around the heart. This was accomplished using a single camera and a set of mirrors to see the backsides of the heart. Bray et al

[14] later combined this method with geometric computing algorithms that generated an anatomically accurate geometry onto which the camera data was projected. Kay et al [54] improved on this arrangement in a porcine model by increasing the number of cameras to two and finally to four, rendering the use of a mirror unnecessary. Qu et al similarly increased the number of cameras, but implemented it in a setup suitable for a rabbit heart in a superfusion chamber [86].

In the last decade panoramic imaging has been used to investigate wavefront dynamics during ventricular fibrillation [53, 90, 11], low-voltage electrotherapy approaches [88, 66], and drug induced arrhythmia maintenance [70]. In that same period of time a number of events have necessitated an update to this methodology. Camera technology has improved dramatically with the creation of complimentary metal-oxide-semiconductor (CMOS) imaging sensors that have the spatial resolution of a charge-coupled device (CCD) camera and the temporal resolution of a photo-diode array (PDA) detector. Additive manufacturing techniques (i.e. 3D printing) have made the creation of experimental setups more accessible and customizable [101]. Finally, an increase in the investigation of atrial fibrillation (AF) initiation and maintenance using transgenic mouse models [65, 113, 78] has created the need for setups that are easily scalable to accommodate small rodent hearts. Here we present our efforts to meet this increasing need in a way that is both accessible and simple to implement.



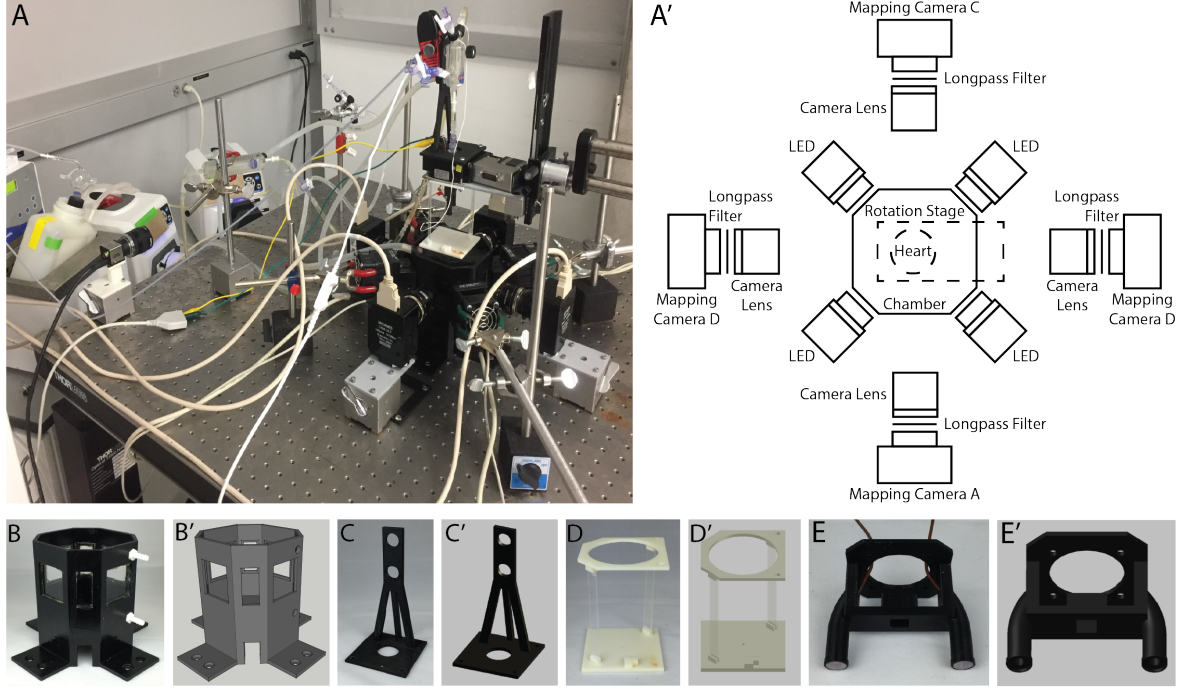


Figure 3.1: **Panoramic optical mapping system.** (A) Panoramic optical mapping requires a more complex setup than optical mapping conducted with a single camera. In addition to increasing the number of optical cameras, we designed and 3D printed a number of experimental components to facilitate the experiments. (B) An upright chamber with four windows for optical cameras and four smaller windows for excitation LEDs. The chamber was waterproofed using a multiple smooth layers of latex based paint on both the interior and exterior surfaces. (C) A bubble trap mount to facilitate raising and lowering of the perfusion system with the rotational stage. (D) After administration of the excitation-contraction uncoupler, a suture is based through the eyelet in the base of the platform, passed through the apex, returned through the eyelet, and brought up and around the leveraging block. A clip is then used to anchor the suture in place. (E) Ag-AgCl electrodes are mounted to the cannula holder to maintain close and consistent pseudo ECG recordings during each experiment.

# Methods

## 3.3.1 Experimental Setup

Optical mapping systems have been described previously in detail [93, 28, 71]. We limit our description to the characteristics unique to this system. Our panoramic imaging setup (Figures 3.1A and 3.1A' consists of four CMOS Ultima cameras attached to a MiCAM05 acquisition system (SciMedia Ltd, Costa Mesa, CA). These cameras are mounted to magnetic bases and outfitted with 35mm C-mount lenses (MLV35M1, Thor Labs, Newton, NJ) and 655 nm long pass filters (ET655lp, Chroma Technology Corporation, Bellow Falls, VT). At 45° angles between the cameras are four 630 nm red LEDs (UHP-T-LED-630, Prizmatix Ltd, Givat-Shmuel, Israel). The perfusion system runs into a cannula mounted to a rotational stage (URS50, Newport Corporation, Irvine, CA). The stage is powered and rotated using a custom Labview interface, arduino, and stepper driver. A parts list, code, and assembly instructions are included in the addendum.

Building a panoramic optical mapping setup is a non-trivial task. Being able to customize a system to a specific set of criteria is extremely useful in accomplishing this. However, professional customization is expensive and not all labs have access to cost reducing resources like institutional machine shops. Recently, multiple labs have published on their efforts to use 3D printing to address this issue [101, 2]. Similarly, we have used computer-aided design (CAD) and 3D printing to reduce the cost and increase the customizability of our panoramic imaging approach.

Here we present but a few of the potential applications of 3D printing in customizing a panoramic imaging system. We use a hanging Langendorff perfused preparation in a 3D

printed superfused chamber (Figure 3.1B). The tissue chamber was designed (Figure 3.1B') to maximize accessibility to heart for cameras and LEDs, while minimizing the volume in an effort to minimize the quantity of drug required to reach desired concentrations. Because we use a superfused chamber, it is necessary to rotate the heart rather than the camera when collecting images for geometric reconstruction. To prevent the perfusion tubing from becoming tangled, we designed and printed a cannula mount (Figure 3.1E) that attaches to the rotating face of the rotational stage directly above the heart and a bubble trap mount (Figure 3.1C) to be positioned on the opposite side of the stage. Connecting the bubble trap and the cannula is a female-to-female leir lock connector with an o-ring and swivel that allows the two ends of the connector to spin independent of one another, thus preventing entanglement. Additionally, a platform (Figure 3.1D) was designed and printed to facilitate anchoring of the cardiac apex without obscuring the field of view of the cameras or LEDs. Items not highlighted include camera mounts, positioning brackets, and a backdrop for increasing image contrast during rotation of the heart.

Design of all components was either done in entirely free (e.g. Autodesk Student Version, Autodesk Inc, San Rafael, CA) or well-discounted (e.g. SketchUp Pro Academic License, Trimble Inc, Sunnyvale, CA) CAD software packages. Once completed, the designs were exported to the stereolithography format (i.e. \*.stl) and a printer path was created using either the Stratasys Insight 10.8 or Stratasys Control Center 10.8 software packages. Printing was done on both a Stratasys Fortus 250mc and a Stratasys uPrint SE Plus (Stratasys, Eden Prairie, MN) using acrylonitrile butadiene styrene (ABS) plastic. Print time varied widely from 2 hours for the smallest components to over 30 hours for the chamber. All designs and their 3D printing specifications will be made available at the time of publication. It should be noted that sophisticated 3D printers can themselves be cost prohibitive. Similar designs

can still be accomplished using entry-level 3D printers, but different design approaches must be used to compensate for their general lack of dissolvable support materials.

### 3.3.2 Camera Calibration

We established the camera calibrations before conducting the experiments. The geometry camera (UI-322XCP-M, IDS Imaging Development Systems, Obersulm, Germany) uses the same window as Camera A. To maintain the integrity of these cameras' calibrations the geometry camera was first calibrated from a bracketed position and then moved to the side. Optical mapping camera A was then calibrated and left in place for the duration of the experiment. During calibration, white LEDs (Joby Gorillatorch, DayMen US Inc, Petaluma, CA) were positioned at the illumination windows to increase the contrast between the cuboid and the calibration grid. These were later replaced by the red LEDs for the optical mapping study. Upon terminating the experiment, the geometry camera is returned the bracketed position for collection of the silhouette images (see Geometric Reconstruction).

The method for establishing pixel-to-geometry correspondence has already been described in detail [14, 54]. Briefly, we first solve for the unknown parameters of a perspective camera model [45]. This is done by first imaging an object of known dimensions with easily identifiable landmarks whose positions on the object's surface are also known. In our case we used a rectangular cuboid with 1x1x2 (LxWxH) inch dimensions. A grid was placed on the outward facing surfaces providing each camera with sixty-four visible intersections when the cuboid is placed such that two faces are visible from each camera.

We created a graphical user interface (GUI) to ease the process of establishing the calibration (Figure 3.2A). In the ideal scenario (i.e., all intersections visible) an automated algorithm

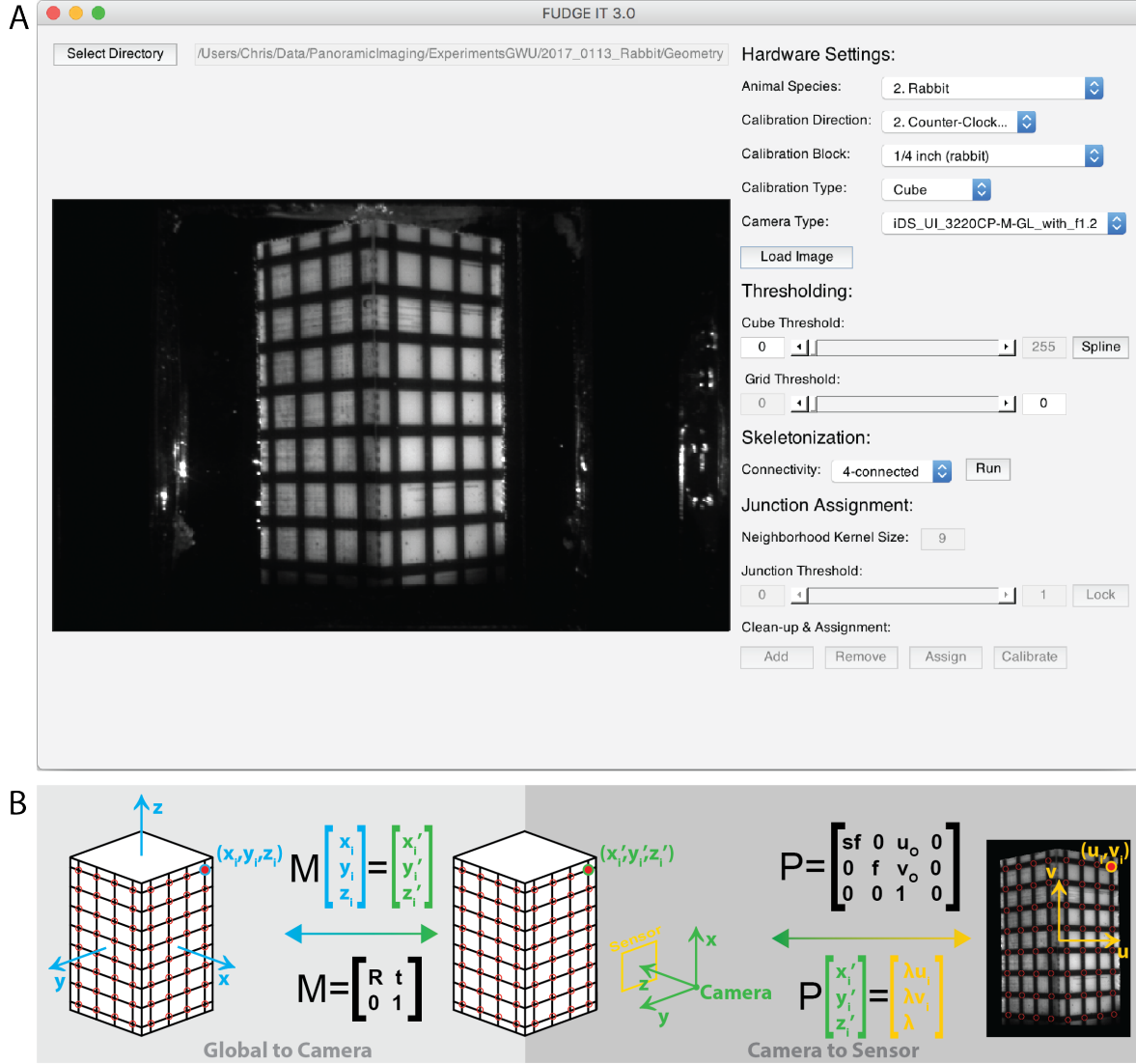


Figure 3.2: **Calibration of geometry and optical cameras.** (A) MATLAB graphical user interface to semi-automate the calibration of each camera needed to facilitate the projection of optical data onto the geometric surface. Detailed explanations and code are included in the addendum. (B) The cuboid is used to create a global coordinate system whose origin is at the cuboid's center. All grid junctions on the cuboid surface have known coordinates in the global coordinate system. Identification of these points in a 2D image provides the necessary number of known values to solve for the unknown components of the global-to-camera (i.e., transformation) and the camera-to-sensor (i.e., perspective projection) matrices.

identifies and appropriately labels all intersections based on a user created mask of the cube and its grid. Tools are provided that allow the user to correct poorly identified junctions prior to labeling. In the non-ideal situation (i.e., all intersections not visible) the user is queried for the number of a visible junction and all other visible junctions are then automatically labeled. Detailed descriptions of the algorithms used to accomplish this can be found in the addendum. A Levenberg-Marquardt nonlinear optimization algorithm receives the 2D junction locations for each camera and the corresponding 3D intersection values and iteratively solves for the unknown extrinsic and intrinsic camera parameters needed to create transformation matrices to connect the two data sets.

The extrinsic camera parameters include the camera position ( $t$ ) and rotation ( $R$ ) with regards to the global coordinate system created by the cuboid. These translation and rotation values comprise the transformation matrix ( $M$ ) as seen in Figure 3.2B. The transformation matrix from the camera coordinate system to the imaging plane, also known as the perspective transformation ( $P$ ), utilizes the intrinsic parameters focal length ( $f$ ), aspect ratio ( $s$ ), and the image center values ( $u_o, v_o$ ). The final component of the transformation corrects for lens distortion. Our setup, as described above, experiences little to no lens distortion, however, this component of the algorithm is still included in the calibration GUI and is described in detail in previous work. The optimization algorithm is run for all four optical cameras and the geometric camera, providing each with a unique set of transformation matrices that will later be used for projection of data onto the reconstructed geometry.

### 3.3.3 Optical Mapping

The rabbits were initially anesthetized using a ketamine and xylazine cocktail. We administered a dose of heparin and brought them to a deeper level of anesthesia using isofluorene. Once a reflex test failed to illicit a response, we excised the heart using a sternal thoracotomy and immediately cannulated the aorta on a secondary Langendorff perfusion setup. We allowed 3-5 minutes for the beating heart to clear remaining traces of blood before placing it on the panoramic perfusion system and lowering it into the tissue chamber.

Once in the chamber, we allowed 10 minutes for the heart to recover from explantation and cannulation. After the recovery period we added approximately 0.5 mL of the excitation-contraction uncoupler blebbistatin (Sigma-Aldrich, St. Louis, MO) into the perfusate and brought the perfusate up to the final concentration (10  $\mu$ M) by slowly injecting blebbistatin into a drug port just up stream from the cannula bubble trap. Once contraction was suppressed, we added the voltage sensitive dye di-4-ANBDQBS (University of Connecticut, Storrs, CT) to the bubble trap up to a final concentration of 35  $\mu$ M before beginning the experimental protocol.

We first conducted a standard restitution protocol at 300, 270, 240, 210, 180, and 150 ms cycle lengths (CL). We then administered a 30  $\mu$ M dose of the ATP channel activator Pinacidil (Sigma-Aldrich, St. Louis, MO) to create a substrate that could sustain a reentrant ventricular arrhythmia. After allowing 10 minutes for the drug to take full effect we induced VF using a 1 second 60 Hz pacing burst. Initialization and maintenance of the arrhythmia were imaged at multiple time points.

### 3.3.4 Surface Generation

Upon completion of the optical mapping studies, we removed Camera A and returned the geometry camera to its bracketed position. The LEDs nearest the geometry camera were replaced with white LEDs and a backdrop was placed behind the heart to improve contrast. Using a custom built LabView program, we rotated the rotational stage, to which the cannula was attached, three hundred sixty degrees collecting an image of the heart every five degrees. We then uploaded these images to our custom written MATLAB GUI (Figure 3.3A) that facilitates identification of the heart silhouette in each image using a combination of thresholding and polyline tools. Heart pixels are represented as ones and background pixels as zeros (Figure 3.3B).

We then used the occluding contour method [73, 80] in conjunction with an octree algorithm to efficiently identify the volume represented by the silhouettes in similar fashion to previously described work [54]. Briefly, an octree is used to deconstruct a volume, slightly larger than that of the heart and centered at the world coordinate system origin, into eight constituent voxels stacked on top of one another as seen in the first iteration of Figure 3.3C. The vertices of each voxel are projected onto each of the silhouettes in succession by rotating the volume five degrees between silhouettes. Voxels whose vertices are either completely inside the heart (i.e. all assigned a one) or outside the heart (i.e. all assigned a zero) remain unchanged. Voxels who lie along the border (i.e. whose pixels are a mix of ones and zeros) are broken down using the octree. The process is repeated until the desired resolution is reached.

Once this was accomplished, the resulting volume was input into an updated version of the triangular mesh generating Visualization Toolkit (v7.1, Kitware Inc., Clifton Park, NY)



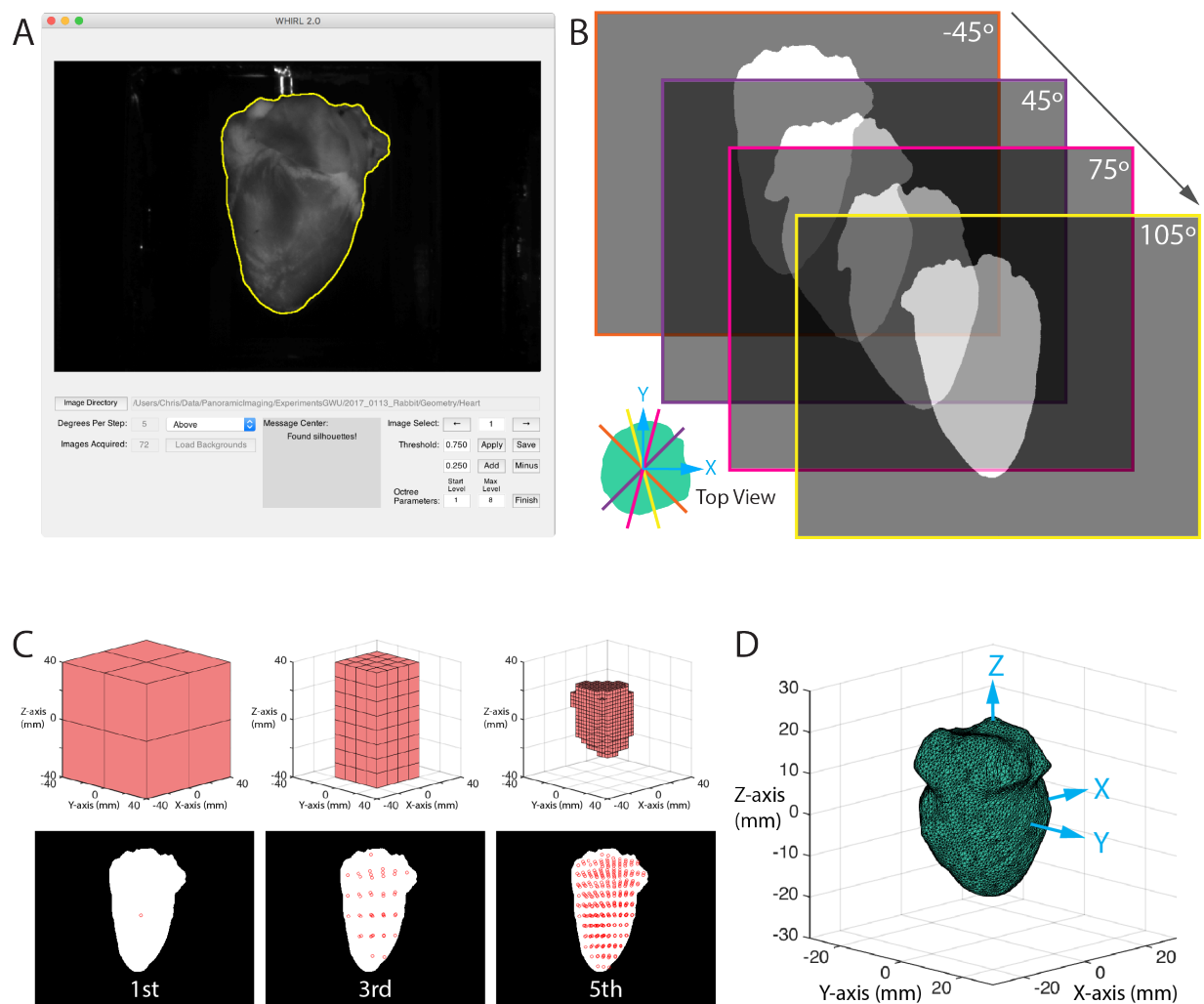


Figure 3.3: **Geometric reconstruction.** (A) A MATLAB graphical user interface was developed to facilitate accurate identification of the heart silhouettes needed for geometric reconstruction. A detailed description and the code are included in the addendum. (B) The heart was rotated and binary silhouette images were collected every 5 degrees. (C) Using the occluding contours method paired with an octree algorithm a series of voxels are iteratively broken down to identify the heart volume. (D) This binary volume is passed by MATLAB as the input to a VTK program that creates a triangulated mesh representative of the binary volume.

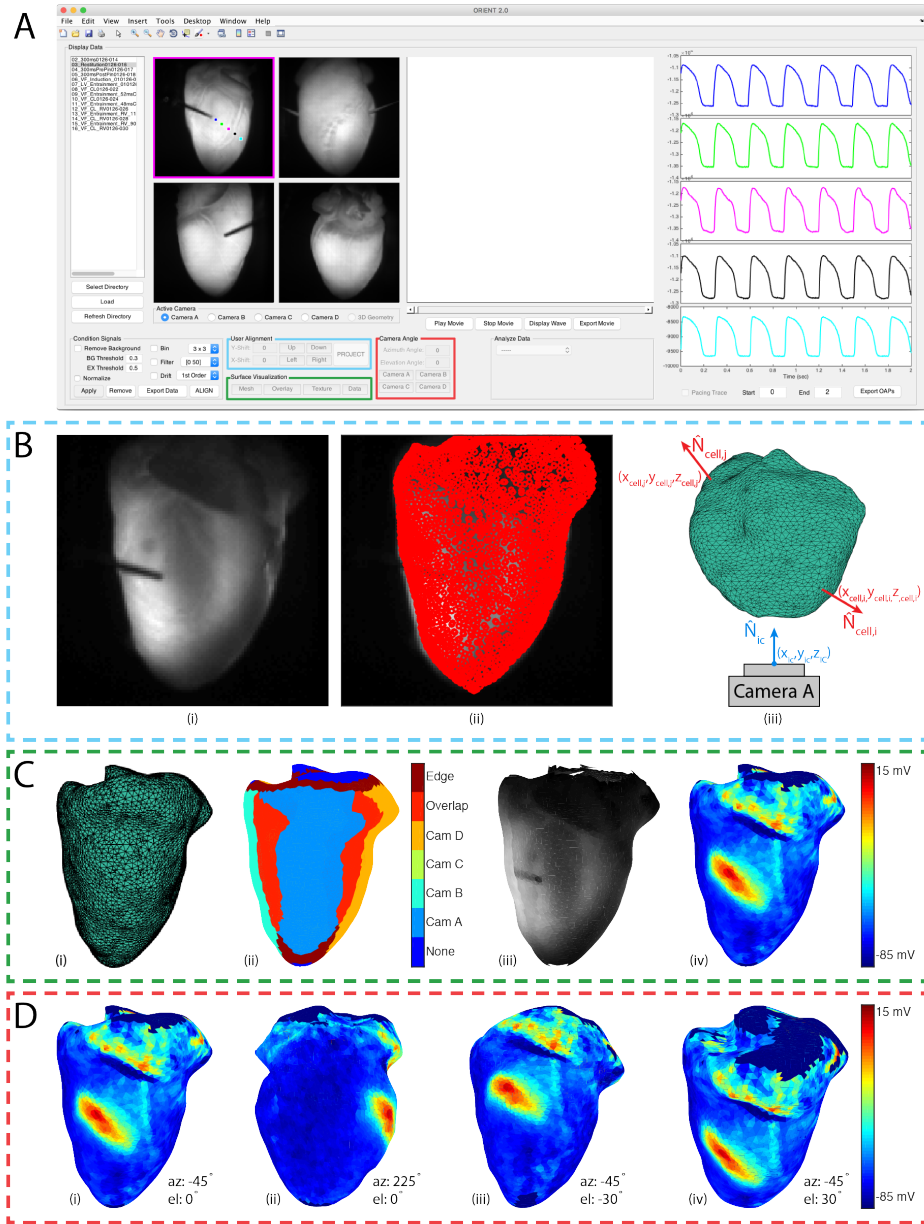


Figure 3.4: **Data processing and projection** (A) A final MATLAB GUI was created to facilitate the processing of optical data and its projection onto the representative geometry. (B) Tools are provided to correct minor inaccuracies in projection. Camera facing centroids are first identified as those whose normals ( $\hat{N}_{cell}$ ) creates an angle greater than  $90^\circ$  with the camera normal ( $\hat{N}_{ic}$ ). (C) The surface can then be visualized as a triangulated mesh (i), a map of the camera assignments made to each centroid (ii), texture (iii), and membrane potential (iv). (D) Tools are provided to rotate the heart using click-and-drag, to the view from each camera, and to specific viewing angles using azimuth and elevation angles.

algorithm developed by Kay et al. The algorithm first extracts an isosurface from the volume data using a marching cubes algorithm [69] and then refines the surface using a Delaunay triangulation [13, 115]. The result is a triangular mesh (Figure 3.3D) representative of the epicardium with  $N_{\text{cells}}$  cells (i.e. triangles) and  $N_{\text{verts}}$  vertices.

### 3.3.5 Projection and Visualization

Projection of the data onto the heart surface by texture mapping [44] and subsequent analysis was facilitated with a final GUI (Figure 3.4A) that builds on the foundation of our previously published work on the analysis of optical mapping signals [64]. We first load in a complete data set and remove background pixels lacking physiological data. We then normalized the optical action potentials, performed spatial filtering by binning with a 3x3 box shaped averaging kernel, applied a 100<sup>th</sup> order FIR temporal filter with a lowpass of 0-100 Hz, and performed 1st order drift removal as necessary. We have also included a polyline tool to facilitate the removal of undesired regions (e.g. the atria when the focus of the study is the ventricles). The final step before projection is the creation of an image mask. Since surface curvature at the edge of each image results in a decrease in the signal-to-noise (SNR) ratio and introduces artifacts [4], a weighted gradient was created for each mask with center pixels being assigned values of 1 and the outermost edge pixels being assigned values of 0.5.

Once conditioned and masked, the centroids of the triangles on the mesh are projected onto each optical mapping camera using the transformation matrices derived from previously described camera calibrations (Figure 3.4B(i) and 3.4B(ii)). Assignments are made using the methodology of Kay et al [54]. Briefly, for each camera the angle between the camera view ( $\hat{N}_{\text{ic}}$ ) and each of the mesh cells ( $\hat{N}_{\text{cell}}$ ) is calculated (Fig 4B (iii)). Minor inaccuracies

in projection can be adjusted using the User Alignment tools in the GUI. All centroids with angles less than  $90^\circ$  are excluded from assignment at that camera. Centroids with angles greater than  $115^\circ$  are assigned the signal from the closest pixel of that particular camera (e.g. Cam A, B, C, or D). Centroids assigned to multiple cameras are considered Overlap pixels. The signals at these locations are calculated as a weighted average of the two assignments using the weighted gradient mask described earlier. Finally, the outermost edge cells, with angles  $90^\circ$  and  $115^\circ$ , are assigned the Edge identifier and signals are calculated as an edge weighted average.

Once, projected the geometry surface visualization tools (Figure 3.4A) can be used to view the 3D surface as a triangulated un textured mesh (Figure 3.4C(i)), an assignment map (Figure 3.4C(ii)), a anatomical texture map (Figure 3.4C(iii)), or a texture map of raw fluorescence (Figure 3.4C(iv)). The axes where the 3D surface is visualized will automatically set to allow the user to rotate the model. Azimuth and elevation angles will automatically be updated in the Camera Angle tool bar as the user rotates the heart or can be entered manually (Figure 3.4D (i-iv)). Additionally, buttons have been provided to take the user directly to the view from each of the optical mapping cameras.

## 3.4 Results

When conducting panoramic studies both the resolution of the mapping camera and the generated geometry must be taken into consideration. For each study the mapping resolution of each optical mapping camera is calculated. The average of these values (Table 3.1) becomes the target for the inter-centroidal distance of the mesh generated using occluding contours. We started with a voxel that measured 6 inches on each side. The average intercentroidal

	Rabbit-5	Rabbit-6	Rabbit-7	Rat-6
Average Mapping Resolution ( <i>mm</i> )		0.451±0.017		0.279±0.002
Geometric Resolution ( <i>mm</i> )		0.132		0.080
Final Voxel Resolution ( <i>mm</i> )	4.76	2.38	1.19	0.79
Number of Faces	1,392	5,966	24,342	20,112
Average Inter-Centroidal Distance ( $\mu\text{m}$ )	1.180±0.0702	0.563±0.314	0.282±0.164	0.317±0.199

Table 3.1: **Camera and Mesh Resolutions.** Mapping and geometric camera resolutions were calculated by measuring the number of pixels across the cuboid in each calibration image. Final voxel resolution is that of the smallest voxels in the octree volume. The number of faces is that of the triangulated mesh output from the VTK code. Average inter-centroidal distance is the average distance between each centroid projected onto a mapping camera and it’s nearest neighbor on that 2D plane.

distance was calculated as the average distance of each centroid to its next nearest neighbor. As can be seen in Table 3.1, the sixth iteration of octree occluding contours algorithm generates a mesh with an average inter-centroidal distance, 0.563 mm, closest to that of our mapping camera resolution, 0.451 mm. For the rat and mouse geometries, we reduced the size of the starting voxel and found a similar number of iterations accomplished the desired average inter-centroidal distance.

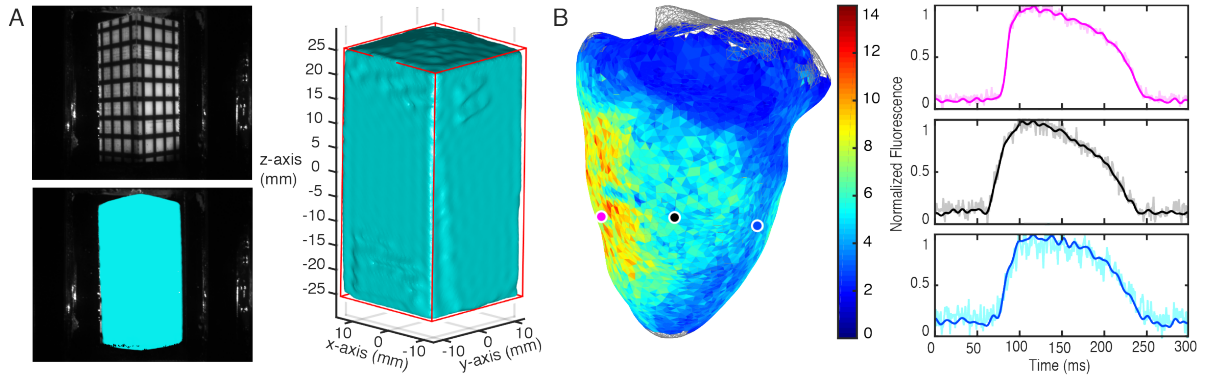
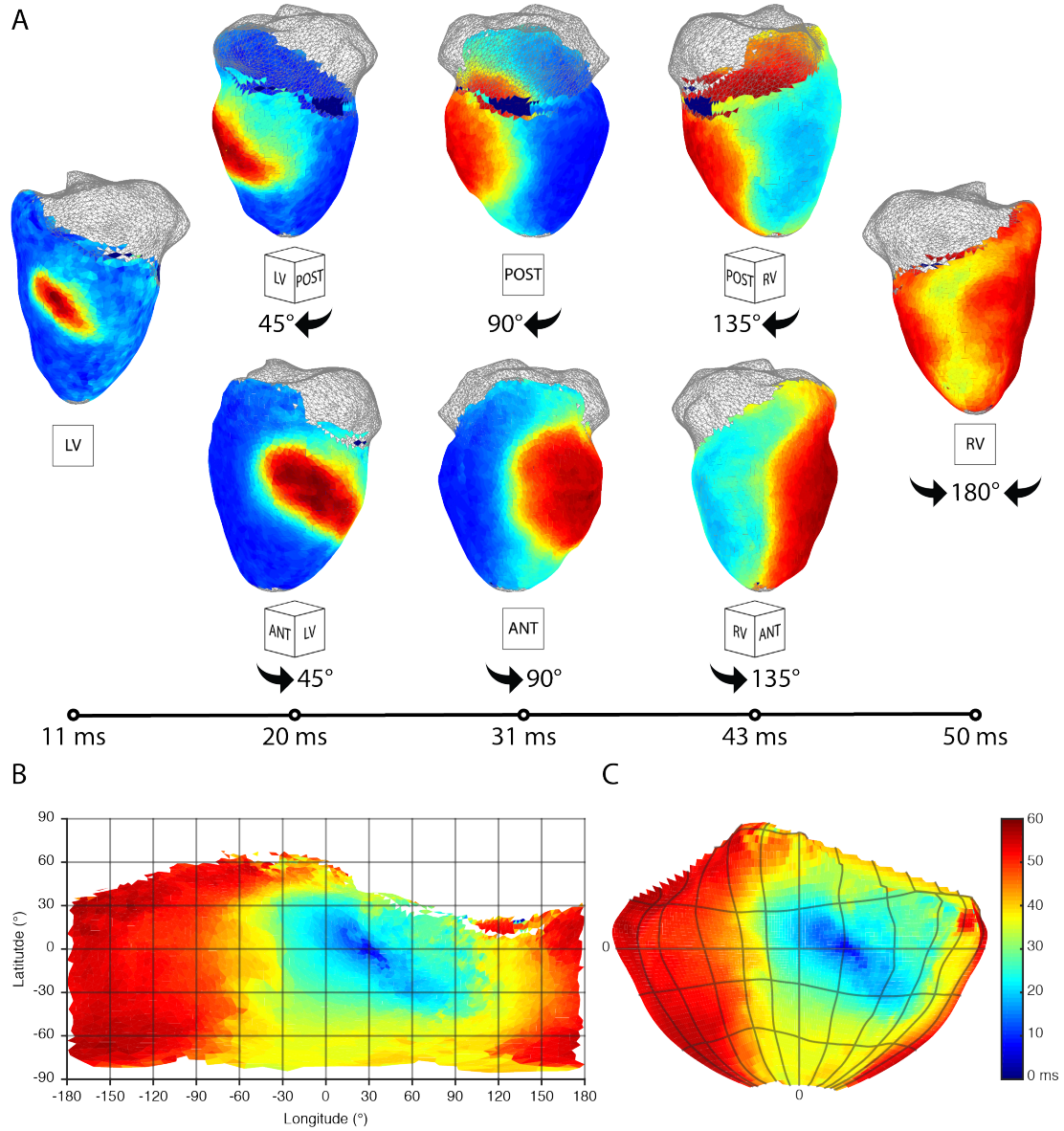


Figure 3.5: **Geometric accuracy and signal-to-noise ratio (SNR).** (A) To validate the geometric accuracy, an object of known volume and geometry (i.e. the calibration cuboid) was reconstructed. The reconstructed volume was within 3% of the measured volume of the cuboid. (B) Signals from the left ventricular anterior, free wall, and posterior regions are shown on a SNR map.

In order to verify the accuracy of the system we reconstructed an object of known geometry. The calibration cube measures 1x1x2 (LxWxH) inches and it's reconstruction can be seen in 3.5A. The volume of the resultant mesh was 2.0108 cubic inches which is a difference of only 0.5%. We also wanted to investigate the reproducibility of the method. We repeated the silhouette collection three times in a row in sequence on the same heart and reconstructed each geometry. We then used a calculation the Hausdorff distance at each vertex to compare the geometries to one another. The Hausdorff distance calculates how similar two subsets within the same metric space are to one another by identifying the greatest distance that can be traveled from a point on one subset to the nearest point on the other subset. Of the three reconstructions the greatest average Hausdorff distance was between the first and third at 0.346 mm and the smallest was between the second and third at 0.142 mm (See Figure 1 addendum).

Properly illuminating the entirety of the epicardial surface is a non-trivial task. Although the post-processing tools are effective, Figure 3.5B demonstrates the variance that can occur in SNR if even illumination is not attained. SNR was calculated as the amplitude of the unfiltered signal over the amplitude of the diastolic interval.

To demonstrate continuity of the projection we tracked a paced beat originating in the left ventricular free wall around both the anterior and posterior sides to their collision on the right ventricular free wall (Figure 3.6A). A 3D isochronal map of activation was then calculated and unwrapped in a 2D format using both the Mercator (Figure 3.6B) and Hammer (Figure 3.6C) projections. We similarly incorporated tools for looking at action potential duration (APD). Figure 3.7A shows the  $APD_{80}$  of a paced beat origination in the basal right ventricle and terminating in the apical left ventricle. Investigation of cardiac arrhythmias is a key interest in the development of panoramic imaging. The analysis tools include methods for



**Figure 3.6: Time course of activation.** (A) The time course of activation is tracked using membrane potential. A paced beat starts on the left ventricular free wall and the divergent wavefronts are tracked over time around both the posterior and anterior sides to where they meet on the right ventricular free wall. Wavefronts are uninterrupted by artifact or discontinuity. (B) A 2D Mercator projection of the isochronal activation map generated using the processing GUI. (C) A 2D Hammer projection whose latitude and longitude divisions are the same as seen in the Mercator projection.



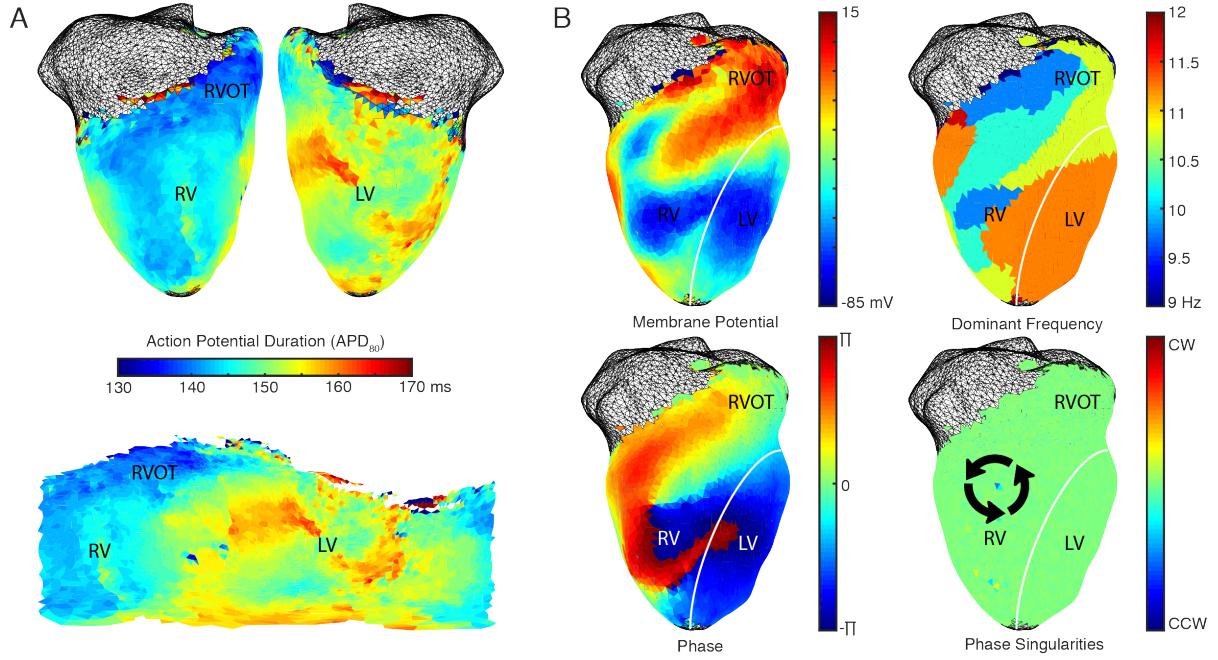


Figure 3.7: **Action potential duration and arrhythmia assessment.** (A) Action potential duration can be calculated using projected data and unwrapped into Mercator and Hammer 2D representations. (B) Arrhythmias like ventricular fibrillation can be analyzed using calculations of dominant frequency, phase, and phase singularities.

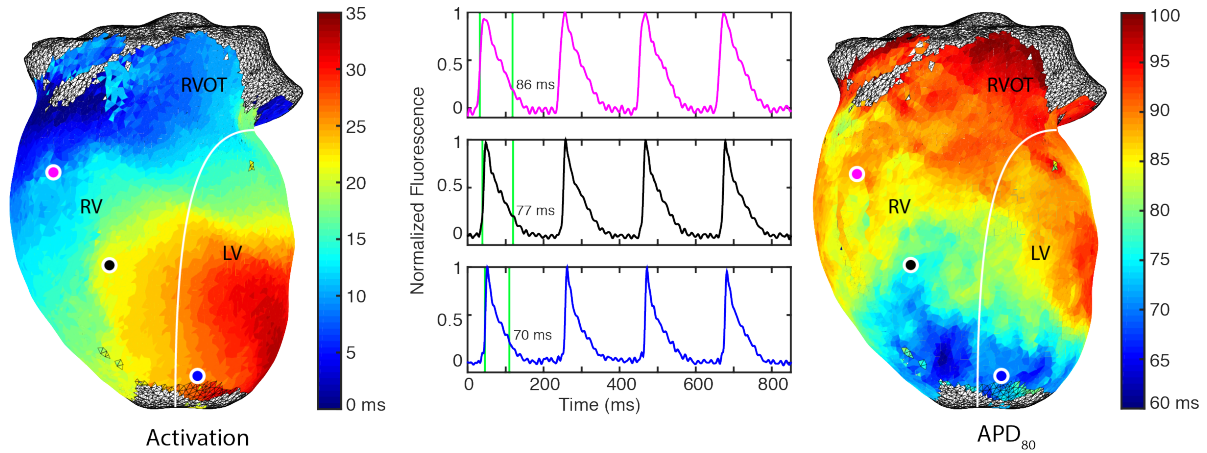


Figure 3.8: **Representative rat data.** A paced beat is shown propagating from the right ventricular free wall into the left ventricular apex. Action potential duration shortens as a function of distance from the paced region.



looking at arrhythmia parameters like dominant frequency, phase and phase singularities (Figure 3.7B).

Using the same cameras and lenses we were able to reconstruct the geometry of various small mammal models. Figure 8 shows the range of geometries the system is able to reconstruct. Figure 3.8 shows a paced beat originating in the right ventricle of a rat and terminating in the apical left ventricle. Representative signals show shortening of  $APD_{80}$  at greater distances from the pacing site.

## Discussion

In this study, we developed a novel CMOS-based panoramic imaging system for the imaging of small mammalian hearts. While panoramic imaging was initially developed over a decade ago, few studies of actual physiology have been performed and none by groups that were not part of the methodologies initial development. Experience has shown us that this is not from a lack of interest in the methodology, but rather is due, in large part, to the complexity of creating a panoramic imaging system and processing the resultant data. In updating our system we sought to make panoramic imaging more accessible by incorporating 3D printing into setup design and construction. We also condensed all the algorithms for camera calibration, geometry reconstruction, and data processing and projection into intuitive graphical user interfaces. Additionally, we have demonstrated the systems ability to image small rodent hearts (e.g., rat) and have discussed subtle changes to the system that would facilitate extending this to imaging of even smaller mouse hearts.

## 3.5 Acknowledgements

Dr Matthew Kay provided me with libraries of MATLAB code that he had written a number of years ago for analyzing panoramic optical mapping data. These served as the foundation for the graphical user interfaces presented here. Drs. Jack Rogers and Hanyu Zhang provided LABVIEW code that served as the foundation for the automatic image acquisition software. Shubham Gupta tested the GUIs for ease of use and made them both easier to use and better to look at.

# Chapter 4

## Role of Restitution Dynamics in Initiation and Maintenance of Ventricular Arrhythmias

### 4.1 Abstract

It has been shown through computational models and experimentation that action potential duration restitution dynamics play an important role in arrhythmia susceptibility. Its exact role, however, remains incompletely understood. Panoramic optical mapping provides a unique tool for looking at arrhythmia initiation and maintenance as it facilitates assessment of the entire epicardium simultaneously. Using this tool, we induced a ventricular arrhythmia in a rabbit model to further investigate the role of action potential duration dynamics in ventricular fibrillation, in particular looking at its role in arrhythmia maintenance.

## 4.2 Key Terms

action potential duration, restitution dynamics, ventricular fibrillation, arrhythmia maintenance

## 4.3 Introduction

Every year, in the United States alone, 300,000 people lose their lives to sudden cardiac death (SCD) [59]. In many instances, this is the result of ventricular tachycardia and/or fibrillation [48]. Years of research have revealed the multiplicity of circumstances that can create a substrate vulnerable to the onset of these types of arrhythmias. Whether a patient is at risk due to a progressive disease ischemic cardiomyopathy [72, 29] or due to an otherwise benign genetic mutation like Long QT syndrome [127], the most successful form of modern treatment is implantation of a defibrillation device [77, 1, 17]. This is accomplished by delivering a single defibrillating biphasic shock with a defibrillation threshold (DFT) of approximately 800V, a mode of defibrillation relatively unchanged since its inception in the late 1970s. While this proves life saving in most situations, a DFT of this magnitude has a number of drawbacks. It decreases the quality of life of the patient and their significant others [95, 46, 84], causes myocardial damage, can be proarrhythmic [43, 111], and results in the device having a limited life time.

Recent advances in material science have resulted in the creation of a flexible stretchable electronics platform capable of interfacing with the dynamic and curvilinear surface of the heart [123, 41, 32]. This platform can be outfitted with sensors (e.g. potential, pH, and temperature) as well as actuators for delivering therapy. While the ramifications for reducing

DFT by delivering therapy in a more targeted fashion are exciting, having a better understanding of the factors that contribute to the initiation and maintenance of arrhythmias will be key to developing algorithms for such an approach.

Many studies have shown that a steep restitution curve can be an indicator for substrates that are susceptible to repolarization alternans at fast pacing rates [58, 36, 105]. Such alternans are indicative of electrical instability which can result in the induction of fibrillation via wavebreak [117, 126]. Additionally, recent findings suggest a heterogenous distribution of restitution slope could be indicative of a proarrhythmic substrate [83, 87]. Studies also seem to indicate a relationship between steep restitution curves and the maintenance of fibrillation by reentry [22, 21]. While current research has established a set of predictive criteria based on restitution dynamics, the mechanism whereby a steep restitution curve leads to arrhythmia is only partially understood.

Panoramic mapping is a unique methodology whereby arrhythmia initiation and maintenance can be studied with high spatial and temporal resolution by using multiple cameras to image the entirety of the epicardial surface [14, 54, 86]. In particular, panoramic imaging makes possible the tracking over time and space of wandering epicenters of reentrant activity [53]. We propose such epicenters of activity will occur with greater frequency and longer duration in regions of high restitution curve slope. To answer this hypothesis we have studied restitution dynamics and their relationship with the initiation and maintenance of VF in a rabbit model.

## 4.4 Methods

### 4.4.1 Animal Experiments

The rabbit was initially anesthetized using a ketamine and xylazine cocktail. We administered a dose of heparin and brought them to a deeper level of anesthesia using isofluorene. Once a reflex test failed to illicit a response, we excised the heart using a sternal thoracotomy and immediately cannulated the aorta on a secondary Langendorff perfusion setup. We allowed 3-5 minutes for the beating heart to clear remaining traces of blood before placing it on the panoramic perfusion system and lowering it into the tissue chamber.

Once in the chamber, we allowed 10 minutes for the heart to recover from explantation and cannulation. After the recovery period we added approximately 0.5 mL of the excitation-contraction uncoupler blebbistatin (Sigma-Aldrich, St. Louis, MO) into the perfusate and brought the perfusate up to the final concentration ( $10\ \mu\text{M}$ ) by slowly injecting blebbistatin into a drug port just up stream from the cannula bubble trap. Once contraction was suppressed, we elevated the heart out of the bath and fixated the heart in an upright positions by passing a suture through the apex and clamping it to the platform (Figure 3.1A). I then oriented the heart with the LV facing Camera A and positioned pacing electrodes on the LV and RV free walls. Upon submerging the heart again, I added the voltage sensitive dye di-4-ANBDQBS (University of Connecticut, Storrs, CT) to the bubble trap up to a final concentration of  $35\ \mu\text{M}$  before beginning the experimental protocol.

The experimental protocol consisted of collecting optical measurements of 30 paced beats at cycle lengths (CL) of 300ms, 270, 240, 210, 180, and 150 ms (Figure 4.1). This was done first on the LV and then on the RV. VF/VT induction was attempted at baseline, however

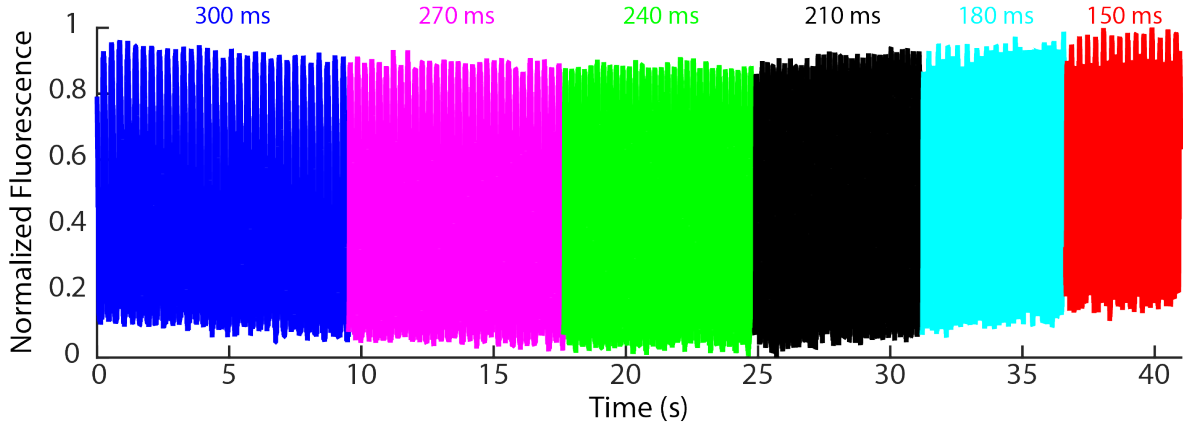


Figure 4.1: **Dynamic Restitution Protocol.** The heart was paced for 30 beats at 300, 270, 240, 210, 180, and 150 ms pacing cycle lengths in sequence. A MATLAB algorithm was written to separate the signals by pacing cycle length and calculate  $APD_{80}$  and DI averages.

the rabbit heart usually lacks sufficient tissue volume to sustain arrhythmia. To create a substrate to sustain arrhythmia I used the  $K_{ATP}$  opener pinacidil (Sigma-Aldrich, St. Louis, MO) at a concentrations of  $30 \mu\text{M}$  and a 1 second 60 Hz sine wave or 20 ms burst pacing. Shortening of APD at this concentration is usually dramatic enough to produce arrhythmia, however, it attempts failed on both the LV and RV the concentration was increased to  $60 \mu\text{M}$  and induction was attempted again.

#### 4.4.2 Data Analysis

Dynamic restitution data was analyzed using a set of custom MATLAB functions. The data was first filtered and conditioned using the techniques described in Chapter 3 (Figure 3.4). Following signal conditioning the pacing output was used to separate the beats into groups based on their CL. These individual groups were subjected to drift removal and baseline zeroing in preparation for calculation of  $APD_{80}$  and DI (Figure 4.2A).  $APD_{80}$  was defined

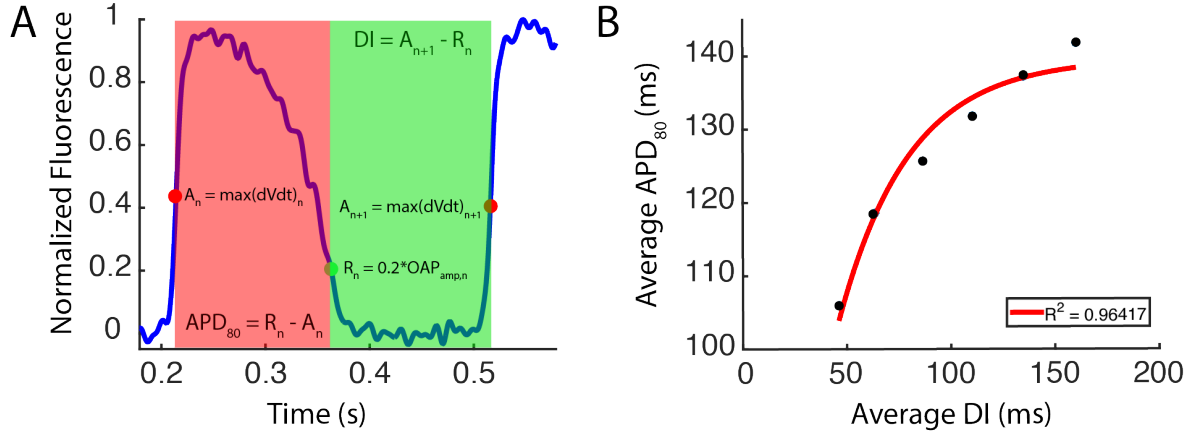


Figure 4.2: **Definition of APD, DI, and APD Restitution.** (A) APD was defined as the difference between the activation of the beat in question ( $A_n$ ) and the time at which the action potential returns to 80% of its maximum amplitude ( $R_n$ ). DI was defined as the difference between  $APD_{80}$  and the activation of the subsequent beat ( $A_{n+1}$ ). (B) APD restitution describes how APD shortens as DI shortens. At each pixel a negative exponential was fit to the average  $APD_{80}$  and DI values. Goodness of fit was calculated at each pixel as well.

as the time between the max  $dVdt$  ( $A_n$ ) of a signal and its repolarization ( $R_n$ ) time (i.e. the time point at which it drops below 80% of its amplitude). DI was defined as the time between repolarization ( $R_n$ ) and the max  $dVdt$  ( $A_{n+1}$ ) of the following beat. The first five beats of each group of thirty were removed and the averages of APD and DI were calculated at each pacing CL at each pixel (Figure 4.2B). A negative exponential curve was fit to each set of APDR values and the maximum slope (Figure 4.3A) and goodness of fit (Figure 4.3B) were calculated.



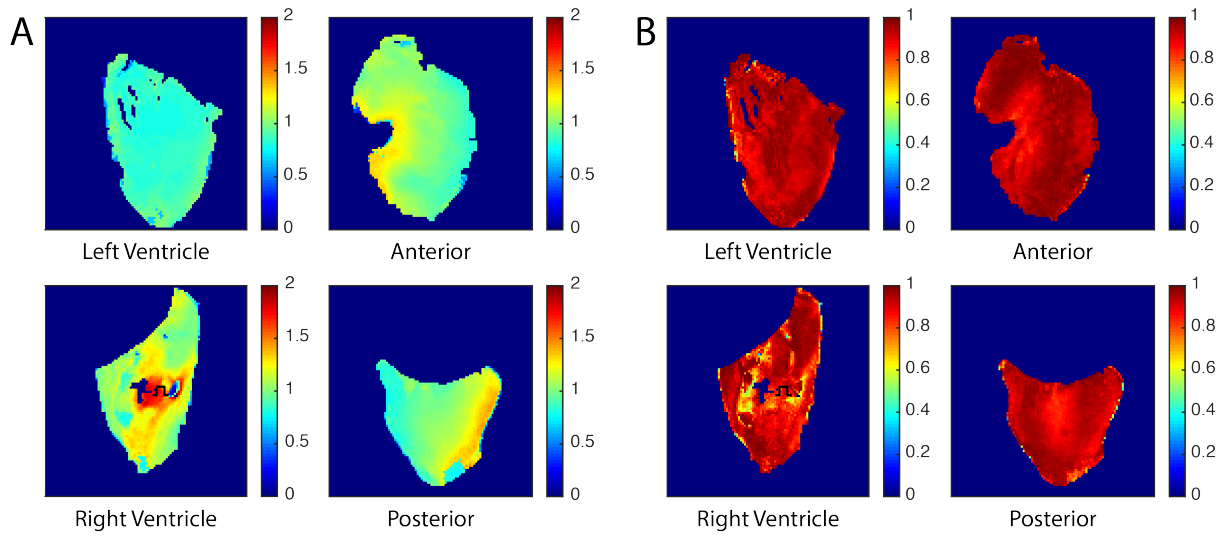


Figure 4.3: **Heat Maps of APDR Max Slope and Goodness of Fit.** An exponential curve was fitted to the APDR values at each pixel and the (A) maximum slope and (B) goodness of fit at each pixel were calculated. Broadly speaking, maximum slope values were greater than 1 with the highest values being located near the pacing site on the RV. Similarly, goodness of fit values largely exceeded 0.8.

## 4.5 Results

In this case study, the reentry was induced in the right ventricular outflow tract (RVOT) where it persisted for three rotations before migrating to the region of high slope located on the RV free wall near the pacing electrode (Figure 4.3A). The reentrant pattern of activity anchored in the RV with the phase singularity of the rotor meandering in or near the region of high slope as can be seen in the five consecutive beats tracked in Figure 4.4. This reentrant pattern of activity persisted for eight consecutive beats, was briefly interrupted, and was initiated again for another thirty-two cycles which lasted for the remainder of the recording. Alternans were noted during the two shortest cycle lengths (Figure 4.5)

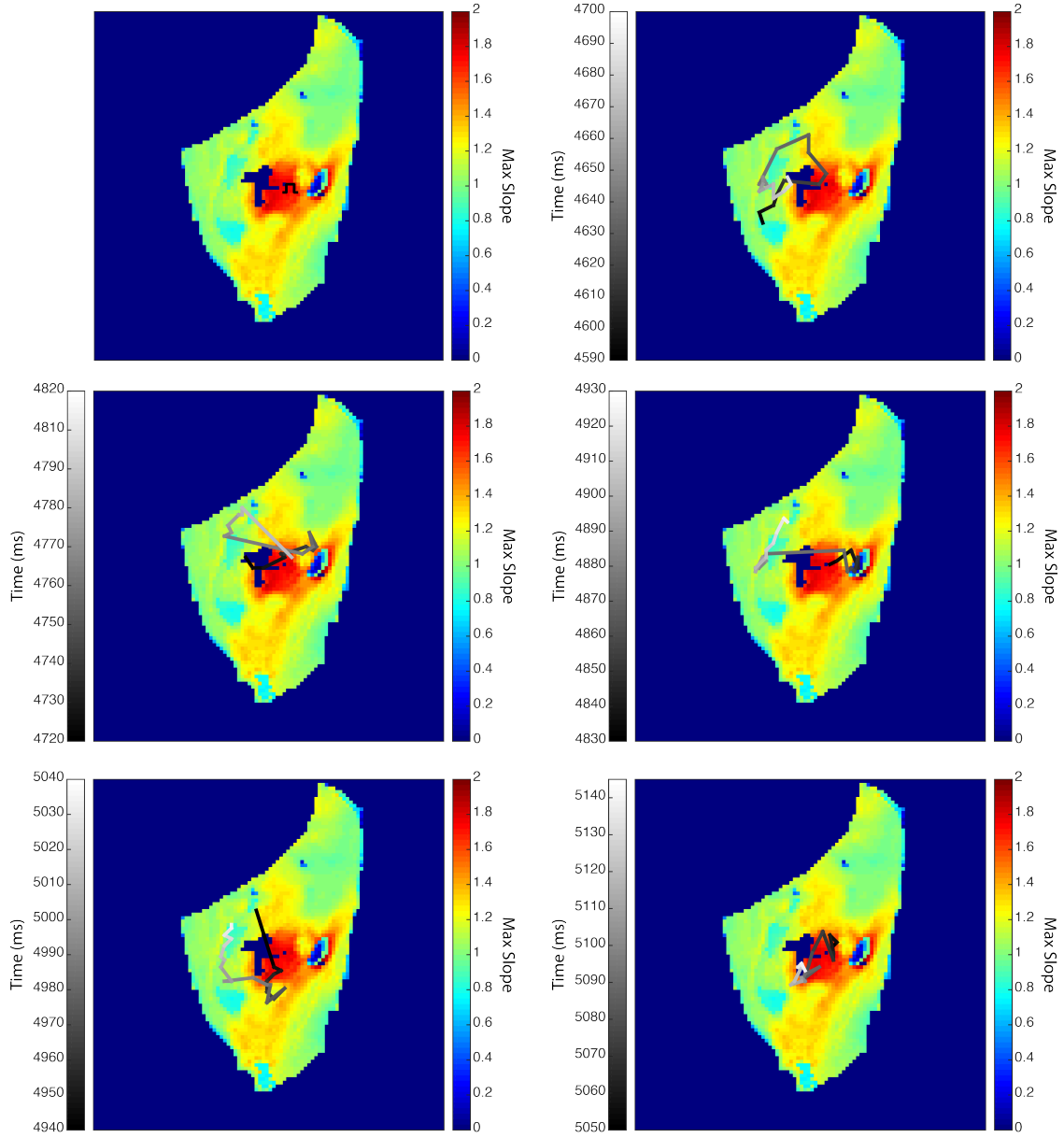


Figure 4.4: **Phase Singularity Tracking During Five Consecutive Cycles** After induction of VF, the phase and phase and associated phase singularities were calculated. The top left image is a heat map of the maximum slope of the APDR with the pacing site labelled in black. Progressing left-to-right and top-to-bottom are the trajectories the phase singularity takes over the course of the first five reentrant beats that occurred after the arrhythmia anchored in the region of high maximum slope. It meander in or around this region for 32 consecutive beats.

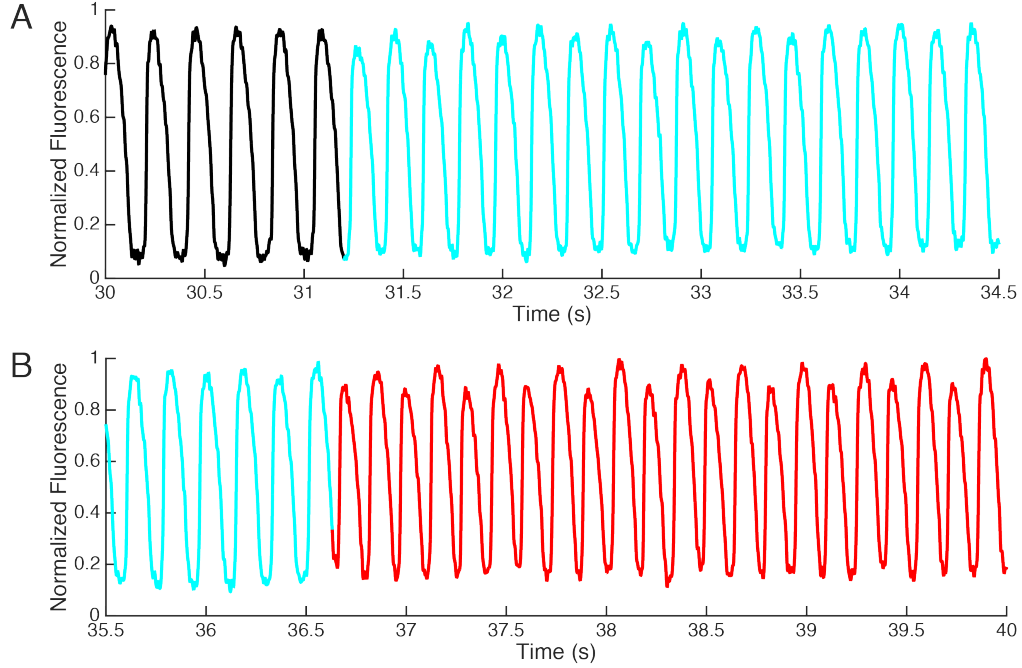


Figure 4.5: **Alternans present in regions of slope  $> 1$ .** At the two shortest cycle lengths, (A) 180 ms and (B) 150 ms, increasingly pronounced alternans were observed. The maximum slope at the pixel from which the representative signal was derived was 1.0552.

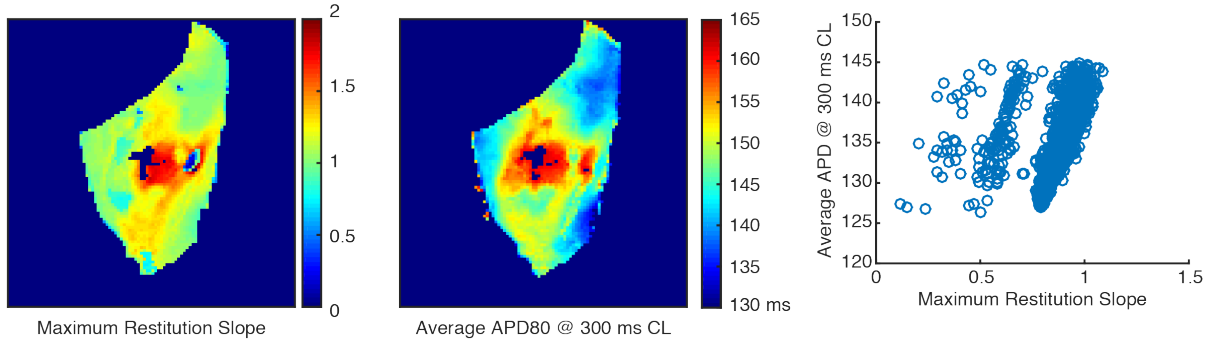


Figure 4.6: **Comparison of Maximum Slope of APDR and Average APD at 300 ms.** Qualitative comparison demonstrates that the maximum restitution slope (Left) and average APD<sub>80</sub> (Middle) at a near intrinsic heart rate (i.e., 300 ms) are similar. A more quantitative comparison (Right) shows a direct relationship between maximum APDR slope and average APD<sub>80</sub> in two different clusters with residual outliers at lower slope values.

## 4.6 Discussion

An arrhythmia requires two things: a trigger and a substrate within which it can be maintained. As stated previously it has been hypothesized and demonstrated through various models that when the slope of the APDR is  $> 1$  that alternans arise creating an electrically unstable substrate. These alternans (Figure 4.5) and their prevalence in the tissue at high pacing rates could create instances of functional block resulting in reentry at high pacing rates. A practical example of this would be a patient who initially has ventricular tachycardia (VT) that then devolves into VF. This rapid pacing combined with the alternans would act as the trigger, while the elevated maximum slope would act as a region of refractory around which propagating waves must travel (i.e. persistent functional block). As the wavefronts travel around this region of high maximum slope it slowly becomes excitable, allowing the wavefront in. Variations in DI cycle-to-cycle could explain the way in which the phase singularity of the rotor wanders in and around the region of high maximum slope taking a different path with each rotation (Figure 4.4).

Interestingly, I noted that qualitatively the maximum APDR slope heat map (Figure 4.6 - Left) looks similar to the average  $APD_{80}$  (Figure 4.6 - Middle) heat map at the intrinsic cycle length of 300 ms. When compared quantitatively there appears to be a direct correlation in two clusters with outliers a lower values of maximum APDR slope (Figure 4.6 - Right). This would suggest that the maximum slope of the APDR is really just a function of how high the intrinsic APD value is. High slopes could therefore be the result of these regions having a greater degree of change possible and therefore steeper APDR slopes. This conclusion was recently corroborated by Shattock et al [96](Figure 4.7) who showed that when APDR is normalized as a percentage of the intrinsic APD the significant differences in APDR slope between sham and TAC mice (Figure 4.7D) are abolished entirely (Figure 4.7E). They

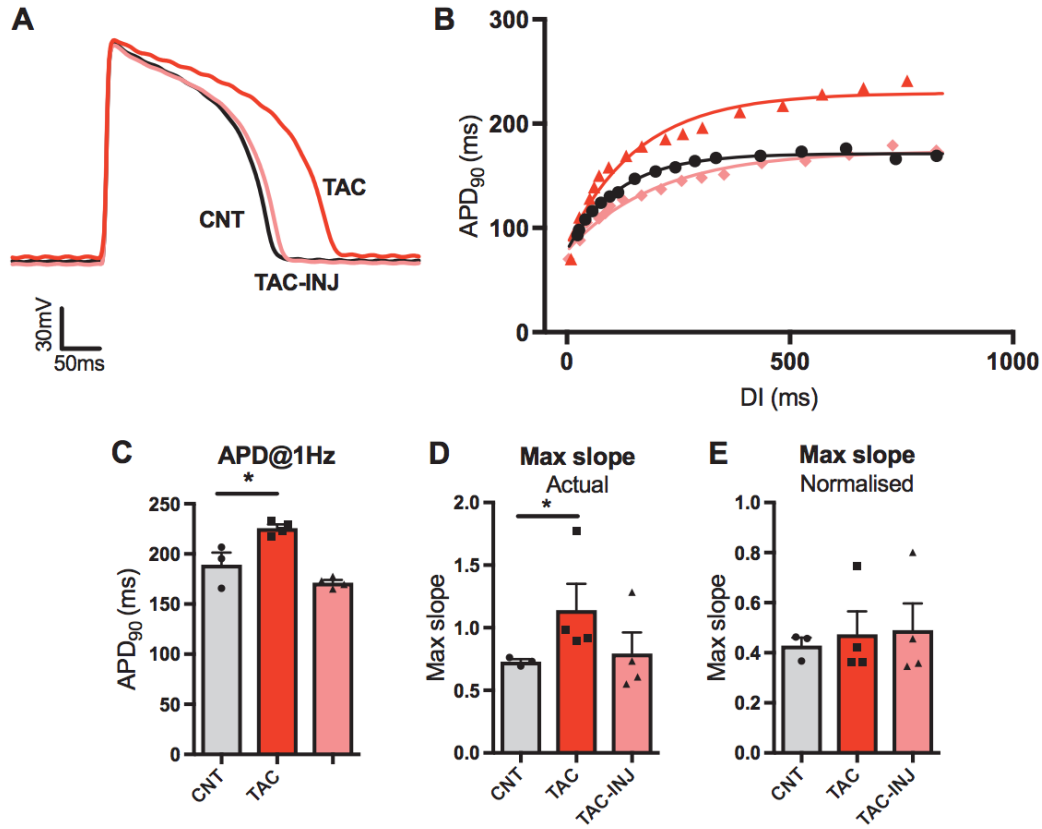


Figure 4.7: **Normalization of restitution curve as a percentage of steady state APD abolishes differences in maximum slope.** (A) Representative optical action potentials from sham, post-transverse aortic constriction (TAC) and negative current injection (TAC-INJ). (B) Representative dynamic restitution curves from each cohort. (C) Mean effect on APD<sub>90</sub>. (D) Mean maximum slope of APDR. (E) Mean maximum slope of the normalized APDR. Modified from Shattock et al [96].

demonstrated this was consistent across various conditions that showed differences in APDR slope. They concluded that susceptibility to VF paralleled changes in APD, and therefore refractoriness, rather than APDR slope. Our case study, suggests that this is especially important in the maintenance of the arrhythmia. It should be noted, however, that this is true in the absence of other factors which effect the substrate. For example, fibrosis could create a complicated substrate in which resulting anatomical reentries could supersede any sort of functional reentry.

## 4.7 Future Work

Future work should first seek to increase the sample size to verify that anchoring of the reentry in regions of high APD is a consistent occurrence. It would also be interesting to compare right versus left ventricular induction to see if rotor anchoring occurs in both types as the LV substrate is different than that of the RV, especially with the RVOT being adjacent to the RV free wall pacing site. Additionally, studies could be done using an S1-S2 method of induction to investigate other types of arrhythmia induction and the resulting arrhythmia maintenance.

## 4.8 Acknowledgements

Drs. Matthew Kay and Bas Boukens helped me extensively in identifying how to analyze and present this data.

# Chapter 5

## Summary and Future Directions

Cardiac arrhythmias, in their various forms, contribute significantly to the death rate, reduced patient quality of life, and the ever increasing economic burden of health care. Being able to properly treat these pathologies is dependent upon tools with high spatial resolution that can be used in both diagnostic and basic research applications. In this dissertation, I have presented a body of work that strives to fulfill this unmet need through the development and validation of technologies that have the potential to help accomplish this goal. Namely, active capacitive electrodes and improved panoramic optical mapping with scalability for small rodent hearts. While I have presented work that validates these tools, there is still substantial work that can be done to bring these technologies to their full potential.

### 5.1 Active Capacitive Electrodes

Previous work done by our collaborators demonstrated their capacitive design's ability to overcome the current leakage and biofluid permeability of traditional exposed metal oxide electrodes. The results from Chapter 1 validate and characterize the signals derived from

the same design in an *in vitro* rabbit model. Signals are comparable to those derived from monopolar surface recordings with easily identifiable morphologies that correspond to the activation and repolarization of the underlying tissue. The quality of these signals is such that methodologies like the tracking of phase singularities can be performed on the data.

Future work, necessarily, will include producing models of the electrode's capacitive function in order to better understand the range of tissue, as a function of distance, that contributes to the signal at each electrode. In application, this will be a necessary step in identifying the density of electrodes necessary to produce first generation prototypes of a chronic epicardial device capable of detecting initiation and tracking maintenance of arrhythmias in patients at high risk of SCD. Additionally, low-voltage defibrillation methodologies using the data derived from such a device could be attempted by incorporating actuators the design. While a novel and exciting idea, defibrillating using the electrode design as it exists may not be possible. Despite being only 900 nm thick, the thermal silicon dioxide layer that encapsulates the electrode creates enough impedance to severely limit it's ability to deliver current to the underlying tissue. If a method for keeping the necessary voltage within a reasonable range is not found, a prototype like the one previously described may have to rely on exposed metal oxide electrodes for delivering therapy.

## 5.2 High Resolution Panoramic Optical Mapping

While many methodologies for panoramic optical mapping have been published, none have picked up and reproduced by other labs as a tool for investigating cardiac electrophysiology. The inability of previous work to bridge the gap between development and adoption in other labs inspired the work in Chapters 3. By developing an extensive GUI based MATLAB



library for camera calibration, geometric reconstruction, and data processing and projection we aim to make panoramic optical mapping more accessible to more scientist in the biomedical engineering community. In line with this goal, I also presented a number of 3D printed designs to help make the system more customizable and less of an economic burden. A motivating factor to this project was also the ever increasing number of mouse models of various types of fibrillation that could directly benefit from panoramic mapping. In an effort to meet this growing need we created an easily scalable system capable of imaging small rodent hearts with minimal modifications.

While the work presented here is effective, there are a number of things that could be done to improve it. The current system relies on an occluding contour algorithm for generation of the heart geometry. This method is effective when applied to the ventricles because it easily reconstructs convex surfaces. If applied to the atria, this methodology could breakdown due to the more dynamic surface of the atria which frequently includes concavities. In order to overcome this limitation other methods of surface reconstruction could be explored. Structured light imaging has already been demonstrated as a viable method for reconstructing the epicardial surface of the heart [63]. If paired with the optical mapping camera configuration and synchronized, a 3D method for reconstructing the cardiac geometry could be derived using structured light imaging techniques. Not only could this handle convex surfaces, but it could also facilitate motion correction of optical mapping making it possible to optically map without using an excitation-contraction uncoupler like blebbistatin.

### 5.3 Action Potential Duration Restitution

Finally, chapter 5 detailed the use of the panoramic optical mapping system to look at the role of APDR in arrhythmia dynamics. The case study demonstrated the alternans were in fact created in regions with slope  $> 1$ . It also revealed that the phase singularity of the reentrant rotor migrated to and anchored in the region of greatest slope. Finally, I discovered a strong correlation between regions of high APDR maximum slope and regions with high APD at intrinsic pacing rates. This was corroborated by recent findings from Shottock et al [96].

Future work will necessarily add samples to the case study to verify that anchoring of phase singularities in regions of high APDR/high intrinsic APD is a repeatable phenomenon. Using an S1-S2 method of stimulation could assess the induction of arrhythmias using a different mode more similar to an early after depolarization. Additionally, induction needs to be effected from the left side as well to see how differences between the left and right side contribute to arrhythmia induction and maintenance.

# Appendix A

## MATLAB Code for Panoramic Optical Mapping Graphical User Interfaces

An extensive library of functions was created for the three graphical user interfaces (GUI) developed for streamlining the process of conducting, processing, and analyzing panoramic optical mapping data. The first GUI, titled FIT, facilitates the calibration of each of the cameras used in the study. The second GUI, entitled WHIRL, takes the user through the process of identifying the silhouettes needed to reconstruct the geometry of the heart. It then runs the occluding contours algorithm and sends the output to the C++ VTK function that generates an isosurface. The third GUI, entitled ORIENT, allows the user to process the signals, project the data onto the resultant surface, and then analyze the signals. These three GUIs equate to thousands of lines of code and are not included in the printed version of this dissertation. A link to the MATLAB suite of functions for the GUIs can be found at [www.efimovlab.org](http://www.efimovlab.org).

# Appendix B

## $I_{Ks}$ Regulates Action Potential Duration in a Rate Dependent Manner

### B.1 Introduction

The slowly delayed rectifier current  $I_{Ks}$  is a major determinant of ventricular repolarization in many species. The importance of  $I_{Ks}$  in human is illustrated by the detrimental effect of mutations in its encoding genes, *KCNQ1* and *KCNE1*, which cause long QT 1 syndrome and predispose patients to fatal cardiac arrhythmias. However, the magnitude of  $I_{Ks}$  in human ventricular cardiomyocytes remains poorly understood due to limited experimental access to healthy intact human tissue. The latter hampers the development of accurate computer models and simulations of cardiac disease. Here we investigate the role of  $I_{Ks}$  in ventricular repolarization in an intact tissue preparation derived from the human left ventricle.

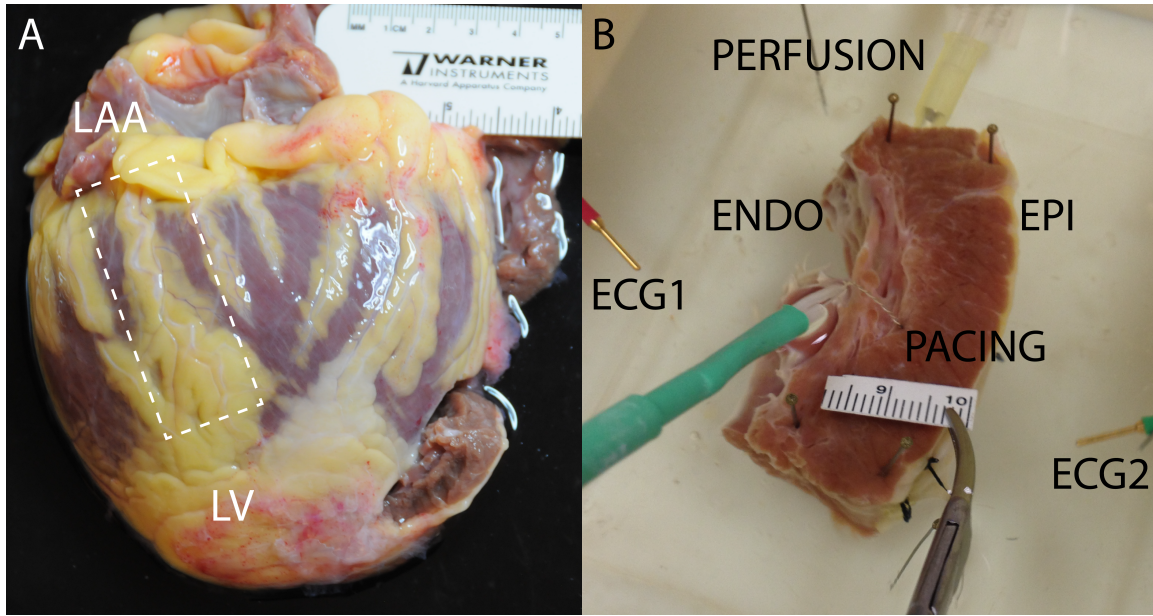


Figure B.1: **Human heart preparation.** (A) The wedges were taken from marginal vessels branching off of the circumflex in the LV. (B) Once cut and cannulated, wedges are laid on their side and paced from the endocardium.

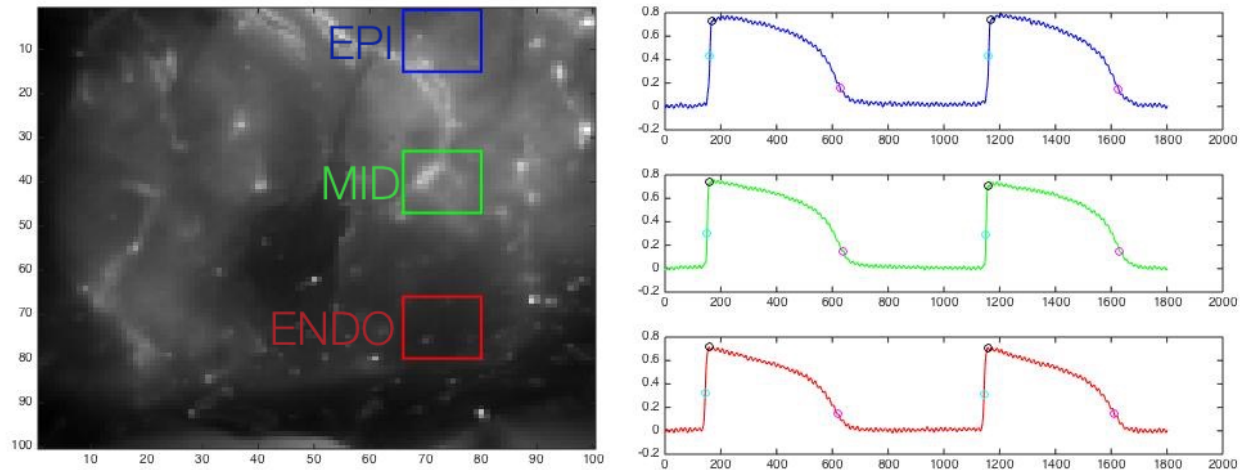


Figure B.2: **Measurement locations.** (Left) Averages of APD were taken from the endocardium, midmyocardium, and epicardium. (Right) Examples of signals from the previously specified regions.

## B.2 Methods

Non-failing hearts are collected from Mid American Transplant services. Immediately upon removal the heart is arrested via coronary perfusion of ice cold cardioplegia. The heart is then transported to lab for tissue collection and functional sample preparation. In an ice cold bath of cardioplegia a marginal artery branching off the circumflex in the LV is identified. A region approximated by the dashed white line in (Figure B.1A) is cut with a razorblade and cannulated with a custom cannula.

During the experiment the heart was perfused with 37° Tyrode's solution at 60-80 mmHg. Blebbistatin was added to arrest contraction and di-4-ANEPPS was added to measure membrane voltage ( $V_m$ ). Restitution at cycle lengths (CL) of 1000, 800, 500, 350 ms was measured paced from the endocardium (Figure B.1B). Then, the  $I_{Ks}$  blocker JNJ-303 was added and the restitution measurement repeated at 40 nM, 200 nM, and 400 nM. Finally the  $I_{Kr}$  blocker E-4031 was added to measure additional prolongation. Average APD and change in APD was measured in the subendocardium, myocardium, and subepicardium (Figure B.2).

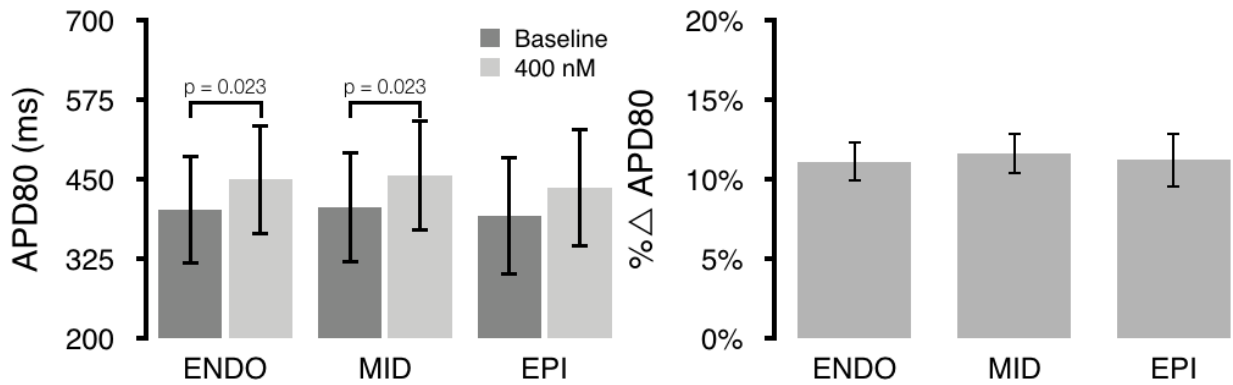


Figure B.3: **Prolongation due to  $I_{Ks}$  Block.** (Left) Prolongation was significant in the endocardium and midmyocardium. (Right) Prolongation was approximately 10% in all regions.

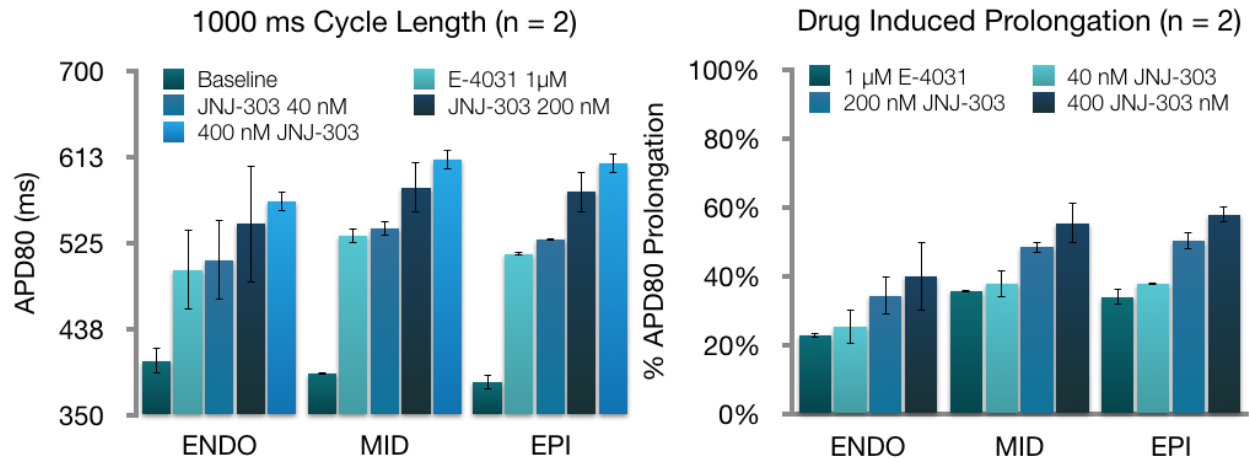


Figure B.4: **Prolongation due to  $I_{Kr}$  Block.** (Left) Prolongation trends toward greater amounts of prolongation following  $I_{Kr}$  block. (Right) While not significant, prolongation increased by another 10% following  $I_{Kr}$  blockade.

## B.3 Results

The  $IC_{50}$  of JNJ-303 was 64 nM. Average APD prolonged by 47.2207 ms, 49.7233 ms, 44.4716 ms in the endocardium, midmyocardium, and epicardium respectively. This prolongation was significant ( $p < 0.05$ ) in the endocardium and midmyocardium (Figure B.3) The relative APD prolongation due to  $I_{Ks}$  blockade was approximately 10%.  $I_{Kr}$  blockade resulted in an additional 10% prolongation (Figure B.4).

## B.4 Conclusion

Our data indicate that the contribution of  $I_{Ks}$  to ventricular repolarization in the healthy human heart is approximately 10%. However,  $I_{Ks}$  function is most likely dependent on sympathetic stimulation. Future experiments will include the addition of isoproterenol and

the use of  $I_{Kr}$  blocker E-4031 to investigate sympathetic dependence and the interaction and redundancy of  $I_{Kr}$  and  $I_{Ks}$ .

## **B.5 Acknowledgements**

Dr. Bas Boukens helped me conduct all of these experiments. His help and advice were invaluable.



# References

- [1] Antiarrhythmics versus Implantable Defibrillators (AVID) Investigators. A comparison of antiarrhythmic-drug therapy with implantable defibrillators in patients resuscitated from near-fatal ventricular arrhythmias. *The New England journal of medicine*, 337(22):1576–83, nov 1997.
- [2] Tom Baden, Andre Maia Chagas, Greg Gage, Timothy Marzullo, Lucia L. Prieto-Godino, Thomas Euler, Lucia L Prieto-Godino, and Thomas Euler. Open Labware: 3-D Printing Your Own Lab Equipment. *PLOS Biology*, 13(3):e1002086, mar 2015.
- [3] Douglas J. Bakkum, Urs Frey, Milos Radivojevic, Thomas L. Russell, Jan Müller, Michele Fiscella, Hirokazu Takahashi, and Andreas Hierlemann. Tracking axonal action potential propagation on a high-density microelectrode array across hundreds of sites. *Nature Communications*, 4:17–24, jul 2013.
- [4] I Banville, R A Gray, R E Ideker, and W M Smith. Shock-induced figure-of-eight reentry in the isolated rabbit heart. *Circulation research*, 85(8):742–52, oct 1999.
- [5] P V Bayly, E E Johnson, P D Wolf, H S Greenside, W M Smith, and R E Ideker. A quantitative measurement of spatial order in ventricular fibrillation. *Journal of cardiovascular electrophysiology*, 4(5):533–46, oct 1993.
- [6] P. V. Bayly, B. H. KenKnight, J. M. Rogers, E. E. Johnson, R. E. Ideker, and W. M. Smith. Spatial organization, predictability, and determinism in ventricular fibrillation. *Chaos: An Interdisciplinary Journal of Nonlinear Science*, 8(1):103–115, mar 1998.
- [7] Kateryna Bazaka and Mohan Jacob. Implantable Devices: Issues and Challenges. *Electronics*, 2(1):1–34, dec 2012.
- [8] Iwona B Beech and Jan Sunner. Biocorrosion: towards understanding interactions between biofilms and metals. *Current Opinion in Biotechnology*, 15(3):181–186, 2004.
- [9] Luca Berdondini, Kilian Imfeld, Alessandro Maccione, Mariateresa Tedesco, Simon Neukom, Milena Koudelka-Hep, and Sergio Martinoia. Active pixel sensor array for high spatio-temporal resolution electrophysiological recordings from single cell to large scale neuronal networks. *Lab on a Chip*, 9(18):2644, 2009.
- [10] L. L. BOSSAERT. *British journal of anaesthesia : BJA.*, volume 79. [Macmillan Journals].

- [11] E. B. Bourgeois, H. D. Reeves, G. P. Walcott, and J. M. Rogers. Panoramic optical mapping shows wavebreak at a consistent anatomical site at the onset of ventricular fibrillation. *Cardiovascular Research*, 93(2):272–279, feb 2012.
- [12] Lyn Bowman and James D. Meindl. The Packaging of Implantable Integrated Sensors. *IEEE Transactions on Biomedical Engineering*, BME-33(2):248–255, feb 1986.
- [13] A. Bowyer. Computing Dirichlet tessellations. *The Computer Journal*, 24(2):162–166, feb 1981.
- [14] M A Bray, S F Lin, and J P Wikswo. Three-dimensional surface reconstruction and fluorescent visualization of cardiac activation. *IEEE transactions on bio-medical engineering*, 47(10):1382–91, oct 2000.
- [15] MARK-ANTHONY BRAY, SHIEN-FONG LIN, RUBIN R. ALIEV, BRADLEY J. ROTH, and JOHN P. WIKSWO. Experimental and Theoretical Analysis of Phase Singularity Dynamics in Cardiac Tissue. *Journal of Cardiovascular Electrophysiology*, 12(6):716–722, jun 2001.
- [16] John E. Burnes, Bruno Taccardi, Robert S. MacLeod, and Yoram Rudy. Noninvasive ECG Imaging of Electrophysiologically Abnormal Substrates in Infarcted Hearts. *Circulation*, 101(5), 2000.
- [17] A E Buxton, K L Lee, J D Fisher, M E Josephson, E N Prystowsky, and G Hafley. A randomized study of the prevention of sudden death in patients with coronary artery disease. Multicenter Unsustained Tachycardia Trial Investigators. *The New England journal of medicine*, 341(25):1882–90, dec 1999.
- [18] Charles Byers, James Beazell, Joseph Schulman, and Ali Rostami. Hermetically sealed ceramic and metal package for electronic devices implantable in living bodies, 1989.
- [19] Patrizia Camelliti, Sara Abou Al-Saud, Ryszard T. Smolenski, Samha Al-Ayoubi, Alexandra Bussek, Erich Wettwer, Nicholas R. Banner, Christopher T. Bowles, Magdi H. Yacoub, and Cesare M. Terracciano. Adult human heart slices are a multicellular system suitable for electrophysiological and pharmacological studies. *Journal of Molecular and Cellular Cardiology*, 51(3):390–398, 2011.
- [20] Y M Chi, Tzyy-Ping Jung, and G Cauwenberghs. Dry-Contact and Noncontact Biopotential Electrodes: Methodological Review. *IEEE Reviews in Biomedical Engineering*, 3:106–119, 2010.
- [21] Nicholas Child, Martin J Bishop, Ben Hanson, Ruben Coronel, Tobias Opthof, Bastiaan J Boukens, Richard D Walton, Igor R Efimov, Julian Bostock, Yolanda Hill, Christopher A Rinaldi, Reza Razavi, Jaswinder Gill, and Peter Taggart. An activation-repolarization time metric to predict localized regions of high susceptibility to reentry. *Heart rhythm*, 12(7):1644–53, jul 2015.

- [22] Ruben Coronel, Francien J.G. Wilms-Schopman, Tobias Opthof, and Michiel J. Janse. Dispersion of repolarization and arrhythmogenesis. *Heart Rhythm*, 6(4):537–543, apr 2009.
- [23] R S Damle, N M Kanaan, N S Robinson, Y Z Ge, J J Goldberger, and A H Kadish. Spatial and temporal linking of epicardial activation directions during ventricular fibrillation in dogs. Evidence for underlying organization. *Circulation*, 86(5):1547–58, nov 1992.
- [24] Jorge M. Davidenko, Arcady V. Pertsov, Remy Salomonsz, William Baxter, and José Jalife. Stationary and drifting spiral waves of excitation in isolated cardiac muscle. *Nature*, 355(6358):349–351, jan 1992.
- [25] Xuexin Duan, Yue Li, Nitin K. Rajan, David A. Routenberg, Yorgo Modis, and Mark A. Reed. Quantification of the affinities and kinetics of protein interactions using silicon nanowire biosensors. *Nature Nanotechnology*, 7(6):401–407, may 2012.
- [26] I R Efimov, D T Huang, J M Rendt, and G Salama. Optical mapping of repolarization and refractoriness from intact hearts. *Circulation*, 90(3):1469–80, sep 1994.
- [27] Igor R. Efimov, Yuanna Cheng, David R. Van Wagoner, Todor Mazgalev, and Patrick J. Tchou. Virtual ElectrodeInduced Phase Singularity. *Circulation Research*, 82(8), 1998.
- [28] Igor R. Efimov, Vladimir P. Nikolski, and Guy Salama. Optical Imaging of the Heart. *Circulation Research*, 95(1), 2004.
- [29] A E Epstein, M D Carlson, R N Fogoros, S L Higgins, and F J Venditti. Classification of death in antiarrhythmia trials. *Journal of the American College of Cardiology*, 27(2):433–42, feb 1996.
- [30] B. Eversmann, M. Jenkner, F. Hofmann, C. Paulus, R. Brederlow, B. Holzapfl, P. Fromherz, M. Merz, M. Brenner, M. Schreiter, R. Gabl, K. Plehnert, M. Steinhäuser, G. Eckstein, D. Schmitt-Landsiedel, and R. Thewes. A 128 x 128 cmos biosensor array for extracellular recording of neural activity. *IEEE Journal of Solid-State Circuits*, 38(12):2306–2317, dec 2003.
- [31] Fan-Gang Zeng, S. Rebscher, W. Harrison, Xiaolan Sun, and Haihong Feng. Cochlear Implants: System Design, Integration, and Evaluation. *IEEE Reviews in Biomedical Engineering*, 1:115–142, 2008.
- [32] Hui Fang, Ki Jun Yu, Christopher Gloschat, Zijian Yang, Enming Song, Chia-Han Chiang, Jianing Zhao, Sang Min Won, Siyi Xu, Michael Trumpis, Yiding Zhong, Seung Won Han, Yeguang Xue, Dong Xu, Seo Woo Choi, Gert Cauwenberghs, Matthew

- Kay, Yonggang Huang, Jonathan Viventi, Igor R. Efimov, and John A. Rogers. Capacitively coupled arrays of multiplexed flexible silicon transistors for long-term cardiac electrophysiology. *Nature Biomedical Engineering*, 1(3):0038, mar 2017.
- [33] Pouria Fattahi, Guang Yang, Gloria Kim, and Mohammad Reza Abidian. A Review of Organic and Inorganic Biomaterials for Neural Interfaces. *Advanced Materials*, 26(12):1846–1885, mar 2014.
- [34] Paul A Friedman. Novel mapping techniques for cardiac electrophysiology. *Heart (British Cardiac Society)*, 87(6):575–82, jun 2002.
- [35] P Fromherz, A Offenhausser, T Vetter, and J Weis. A neuron-silicon junction: a Retzius cell of the leech on an insulated-gate field-effect transistor. *Science*, 252(5010), 1991.
- [36] A. Garfinkel, Y.-H. Kim, O. Voroshilovsky, Z. Qu, J. R. Kil, M.-H. Lee, H. S. Karagueuzian, J. N. Weiss, and P.-S. Chen. Preventing ventricular fibrillation by flattening cardiac restitution. *Proceedings of the National Academy of Sciences*, 97(11):6061–6066, may 2000.
- [37] Walter E Garrey. The nature of fibrillary contraction of the heart.-its relation to tissue mass and form. *American Journal of Physiology–Legacy Content*, 33(3):397–414, 1914.
- [38] Ary L. Goldberger, Valmik Bhargava, Bruce J. West, and Arnold J. Mandell. Some observations on the question: Is ventricular fibrillation chaos? *Physica D: Nonlinear Phenomena*, 19(2):282–289, mar 1986.
- [39] R A Gray, J Jalife, A V Panfilov, W T Baxter, C Cabo, J M Davidenko, and A M Pertsov. Mechanisms of cardiac fibrillation. *Science (New York, N.Y.)*, 270(5239):1222–3; author reply 1224–5, nov 1995.
- [40] Richard A. Gray, Arkady M. Pertsov, and José Jalife. Spatial and temporal organization during cardiac fibrillation. *Nature*, 392(6671):75–78, mar 1998.
- [41] Sarah R. Gutbrod, Matthew S. Sulkin, John A. Rogers, and Igor R. Efimov. Patient-specific flexible and stretchable devices for cardiac diagnostics and therapy. *Progress in Biophysics and Molecular Biology*, 115(2-3):244–251, aug 2014.
- [42] L Harrison, R E Ideker, W M Smith, G J Klein, J Kasell, A G Wallace, and J J Gallagher. The sock electrode array: a tool for determining global epicardial activation during unstable arrhythmias. *Pacing and clinical electrophysiology : PACE*, 3(5):531–40, sep 1980.
- [43] Edward Healy, Tachapong Ngarmukos, and Lawrence Rosenthal. A case of bad timing: inappropriate implantable cardioverter defibrillator therapy due to a critically placed

- premature ventricular contraction. *Pacing and clinical electrophysiology : PACE*, 25(9):1403–5, sep 2002.
- [44] Paul S. Heckbert. Survey of Texture Mapping. *IEEE Computer Graphics and Applications*, 6(11):56–67, nov 1986.
  - [45] J. Heikkilä. Geometric camera calibration using circular control points. *IEEE Transactions on Pattern Analysis and Machine Intelligence*, 22(10):1066–1077, 2000.
  - [46] Adam T Hirsh, Samuel F Sears, and Jamie B Conti. Cognitive and behavioral treatments for anxiety and depression in a patient with an implantable cardioverter defibrillator (ICD): a case report and clinical discussion. *Journal of clinical psychology in medical settings*, 2009.
  - [47] Moritz Hoffa and Carl Ludwig. Einige neue versuche uber herzbewegung. *Zeitschrift Rationelle Medizin*, 9:107–144, 1850.
  - [48] Heikki V. Huikuri, Agustin Castellanos, and Robert J. Myerburg. Sudden Death Due to Cardiac Arrhythmias. *New England Journal of Medicine*, 345(20):1473–1482, nov 2001.
  - [49] Roeland Huys, Dries Braeken, Danny Jans, Andim Stassen, Nadine Collaert, Jan Wouters, Josine Loo, Simone Severi, Frank Vleugels, Geert Callewaert, Kris Verstreken, Carmen Bartic, and Wolfgang Eberle. Single-cell recording and stimulation with a 16k micro-nail electrode array integrated on a 0.18  $\mu\text{m}$  CMOS chip. *Lab on a Chip*, 12(7):1274, 2012.
  - [50] J Jalife. Ventricular fibrillation: mechanisms of initiation and maintenance. *Annual review of physiology*, 62(1):25–50, mar 2000.
  - [51] Jae-Woong Jeong, Min Ku Kim, Huanyu Cheng, Woon-Hong Yeo, Xian Huang, Yuhao Liu, Yihui Zhang, Yonggang Huang, and John A. Rogers. Capacitive Epidermal Electronics for Electrically Safe, Long-Term Electrophysiological Measurements. *Advanced Healthcare Materials*, 3(5):642–648, may 2014.
  - [52] Alain Karma. Electrical alternans and spiral wave breakup in cardiac tissue. *Chaos (Woodbury, N. Y.)*, 4(3):461–472, sep 1994.
  - [53] M. W. Kay, Gregory P Walcott, James D Gladden, Sharon B Melnick, and Jack M Rogers. Lifetimes of epicardial rotors in panoramic optical maps of fibrillating swine ventricles. *AJP: Heart and Circulatory Physiology*, 291(4):H1935–H1941, jun 2006.
  - [54] M.W. Kay, P.M. Amison, and J.M. Rogers. Three-Dimensional Surface Reconstruction and Panoramic Optical Mapping of Large Hearts. *IEEE Transactions on Biomedical Engineering*, 51(7):1219–1229, jul 2004.

- [55] Dion Khodagholy, Jennifer N Gelinias, Thomas Thesen, Werner Doyle, Orrin Devinsky, George G Malliaras, and György Buzsáki. NeuroGrid: recording action potentials from the surface of the brain. *Nature Neuroscience*, 18(2):310–315, dec 2014.
- [56] Dae-Hyeong Kim, Roozbeh Ghaffari, Nanshu Lu, Shuodao Wang, Stephen P Lee, Hohyun Keum, Robert D’Angelo, Lauren Klinker, Yewang Su, Chaofeng Lu, Yun-Soung Kim, Abid Ameen, Yuhang Li, Yihui Zhang, Bassel de Graff, Yung-Yu Hsu, Zhuangjian Liu, Jeremy Ruskin, Lizhi Xu, Chi Lu, Fiorenzo G Omenetto, Yonggang Huang, Moussa Mansour, Marvin J Slepian, and John A Rogers. Electronic sensor and actuator webs for large-area complex geometry cardiac mapping and therapy. *Proceedings of the National Academy of Sciences of the United States of America*, 109(49):19910–5, dec 2012.
- [57] Dae-Hyeong Kim, Nanshu Lu, Roozbeh Ghaffari, Yun-Soung Kim, Stephen P. Lee, Lizhi Xu, Jian Wu, Rak-Hwan Kim, Jizhou Song, Zhuangjian Liu, Jonathan Viventi, Bassel de Graff, Brian Elolampi, Moussa Mansour, Marvin J. Slepian, Sukwon Hwang, Joshua D. Moss, Sang-Min Won, Younggang Huang, Brian Litt, and John A. Rogers. Materials for multifunctional balloon catheters with capabilities in cardiac electrophysiological mapping and ablation therapy. *Nature Materials*, 10(4):316–323, apr 2011.
- [58] M L Koller, M L Riccio, and R F Gilmour. Dynamic restitution of action potential duration during electrical alternans and ventricular fibrillation. *The American journal of physiology*, 275(5 Pt 2):H1635–42, nov 1998.
- [59] C. Y. Kong, K. J. Nattinger, T. J. Hayeck, Z. B. Omer, Y. C. Wang, S. J. Spechler, P. M. McMahon, G. S. Gazelle, and C. Hur. The Impact of Obesity on the Rise in Esophageal Adenocarcinoma Incidence: Estimates from a Disease Simulation Model. *Cancer Epidemiology Biomarkers & Prevention*, 20(11):2450–2456, nov 2011.
- [60] S.P. Lacour, J. Jones, S. Wagner, Teng Li, and Zhigang Suo. Stretchable Interconnects for Elastic Electronic Surfaces. *Proceedings of the IEEE*, 93(8):1459–1467, aug 2005.
- [61] Michael M. Laks, Robert Arzbaecher, James J. Bailey, David B. Geselowitz, and Alan S. Berson. Recommendations for Safe Current Limits for Electrocardiographs. *Circulation*, 93(4), 1996.
- [62] O. Langendorff. Untersuchungen am überlebenden Säugethierherzen. *Pflüger, Archiv für die Gesamte Physiologie des Menschen und der Thiere*, 61(6):291–332, aug 1895.
- [63] J. I. Laughner, S. Zhang, H. Li, C. C. Shao, and I. R. Efimov. Mapping cardiac surface mechanics with structured light imaging. *AJP: Heart and Circulatory Physiology*, 303(6):H712–H720, sep 2012.

- [64] Jacob I. Laughner, Fu Siong Ng, Matthew S. Sulkin, R. Martin Arthur, and Igor R. Efimov. Processing and analysis of cardiac optical mapping data obtained with potentiometric dyes. *American Journal of Physiology - Heart and Circulatory Physiology*, 303(7), 2012.
- [65] Mark D. Levin, Min Min Lu, Nataliya B. Petrenko, Brian J. Hawkins, Tara H. Gupta, Deborah Lang, Peter T. Buckley, Jeanine Jochems, Fang Liu, Christopher F. Spurney, Li J. Yuan, Jason T. Jacobson, Christopher B. Brown, Li Huang, Friedrich Beermann, Kenneth B. Margulies, Muniswamy Madesh, James H. Eberwine, Jonathan A. Epstein, and Vickas V. Patel. Melanocyte-like cells in the heart and pulmonary veins contribute to atrial arrhythmia triggers. *Journal of Clinical Investigation*, 119(11):3420–36, oct 2009.
- [66] Wenwen Li, Crystal M Ripplinger, Qing Lou, and Igor R Efimov. Multiple monophasic shocks improve electrotherapy of ventricular tachycardia in a rabbit model of chronic infarction. *Heart rhythm : the official journal of the Heart Rhythm Society*, 2009.
- [67] Han S. Lim, Stephan Zellerhoff, Nicolas Derval, Arnaud Denis, Seigo Yamashita, Benjamin Berte, Saagar Mahida, Darren Hooks, Nora Aljefairi, Frédéric Sacher, and Pierre Jais. Noninvasive Mapping to Guide Atrial Fibrillation Ablation. *Cardiac Electrophysiology Clinics*, 7(1):89–98, 2015.
- [68] Shien-Fong Lin and John P. Wikswo. Panoramic Optical Imaging of Electrical Propagation in Isolated Heart. *Journal of Biomedical Optics*, 4(2):200, apr 1999.
- [69] William E. Lorensen, Harvey E. Cline, William E. Lorensen, and Harvey E. Cline. Marching cubes: A high resolution 3D surface construction algorithm. In *Proceedings of the 14th annual conference on Computer graphics and interactive techniques - SIGGRAPH '87*, volume 21, pages 163–169, New York, New York, USA, 1987. ACM Press.
- [70] Q. Lou, W. Li, and I. R. Efimov. The role of dynamic instability and wavelength in arrhythmia maintenance as revealed by panoramic imaging with blebbistatin vs. 2,3-butanedione monoxime. *AJP: Heart and Circulatory Physiology*, 302(1):H262–H269, jan 2012.
- [71] Qing Lou, Wenwen Li, and Igor R. Efimov. Multiparametric Optical Mapping of the Langendorff-perfused Rabbit Heart. *Journal of Visualized Experiments*, (55), sep 2011.
- [72] M Luu, W G Stevenson, L W Stevenson, K Baron, and J Walden. Diverse mechanisms of unexpected cardiac arrest in advanced heart failure. *Circulation*, 80(6):1675–80, dec 1989.

- [73] Worthy N. Martin and J. K. Aggarwal. Volumetric Descriptions of Objects from Multiple Views. *IEEE Transactions on Pattern Analysis and Machine Intelligence*, PAMI-5(2):150–158, mar 1983.
- [74] Arvydas Matiukas, Bogdan G Mitrea, Maochun Qin, Arkady M Pertsov, Alexander G Shvedko, Mark D Warren, Alexey V Zaitsev, Joseph P Wuskell, Mei-de Wei, James Watras, and Leslie M Loew. Near-infrared voltage-sensitive fluorescent dyes optimized for optical mapping in blood-perfused myocardium. *Heart rhythm*, 4(11):1441–51, nov 2007.
- [75] George Ralph Mines. On dynamic equilibrium in the heart. *The Journal of physiology*, 46(4-5):349–383, 1913.
- [76] Jacqueline M. Morais, Fotios Papadimitrakopoulos, and Diane J. Burgess. Biomaterials/Tissue Interactions: Possible Solutions to Overcome Foreign Body Response. *The AAPS Journal*, 12(2):188–196, jun 2010.
- [77] Arthur J. Moss, W. Jackson Hall, David S. Cannom, James P. Daubert, Steven L. Higgins, Helmut Klein, Joseph H. Levine, Sanjeev Saksena, Albert L. Waldo, David Wilber, Mary W. Brown, and Moonseong Heo. Improved Survival with an Implanted Defibrillator in Patients with Coronary Disease at High Risk for Ventricular Arrhythmia. *New England Journal of Medicine*, 335(26):1933–1940, dec 1996.
- [78] Rangarajan D Nadadur, Michael T Broman, Bastiaan Boukens, Stefan R Mazurek, Xinan Yang, Malou van den Boogaard, Jenna Bekeny, Margaret Gadek, Tarsha Ward, Min Zhang, Yun Qiao, James F Martin, Christine E Seidman, Jon Seidman, Vincent Christoffels, Igor R Efimov, Elizabeth M McNally, Christopher R Weber, and Ivan P Moskowitz. Pitx2 modulates a Tbx5-dependent gene regulatory network to maintain atrial rhythm. *Science translational medicine*, 8(354):354ra115, aug 2016.
- [79] Sanjiv M. Narayan, David E. Krummen, Kalyanam Shivkumar, Paul Clopton, Wouter-Jan Rappel, and John M. Miller. Treatment of Atrial Fibrillation by the Ablation of Localized Sources: CONFIRM (Conventional Ablation for Atrial Fibrillation With or Without Focal Impulse and Rotor Modulation) Trial. *Journal of the American College of Cardiology*, 60(7):628–636, 2012.
- [80] Wolfgang Niem. Robust and fast modeling of 3D natural objects from multiple views. pages 388–397. International Society for Optics and Photonics, mar 1994.
- [81] Yoshinori Onuki, Upkar Bhardwaj, Fotios Papadimitrakopoulos, and Diane J. Burgess. A Review of the Biocompatibility of Implantable Devices: Current Challenges to Overcome Foreign Body Response. *Journal of Diabetes Science and Technology*, 2(6):1003–1015, nov 2008.



- [82] Michele Orini, Peter Taggart, Neil Srinivasan, Martin Hayward, and Pier D. Lambiase. Interactions between Activation and Repolarization Restitution Properties in the Intact Human Heart: In-Vivo Whole-Heart Data and Mathematical Description. *PLOS ONE*, 11(9):e0161765, sep 2016.
- [83] Hui-Nam Pak, Soon Jun Hong, Gyo Seung Hwang, Hyun Soo Lee, Sang-Weon Park, Jeong Cheon Ahn, Young Moo Ro, and Young-Hoon Kim. Spatial dispersion of action potential duration restitution kinetics is associated with induction of ventricular tachycardia/fibrillation in humans. *Journal of cardiovascular electrophysiology*, 15(12):1357–63, dec 2004.
- [84] Susanne S Pedersen, Martha van den Berg, Ruud A M Erdman, Jenny van Son, Luc Jordaens, and Dominic A M J Theuns. Increased anxiety in partners of patients with a cardioverter-defibrillator: the role of indication for ICD therapy, shocks, and personality. *Pacing and clinical electrophysiology : PACE*, 32(2):184–92, mar 2009.
- [85] A M Pertsov, J M Davidenko, R Salomonsz, W T Baxter, and J Jalife. Spiral waves of excitation underlie reentrant activity in isolated cardiac muscle. *Circulation Research*, 72(3), 1993.
- [86] Fujian Qu, Crystal M. Ripplinger, Vladimir P. Nikolski, Cindy Grimm, and Igor R. Efimov. Three-dimensional panoramic imaging of cardiac arrhythmias in rabbit heart. *Journal of Biomedical Optics*, 12(4):044019, 2007.
- [87] Julia Ramírez, Violeta Monasterio, Ana Mincholé, Mariano Llamedo, Gustavo Lenis, Iwona Cygankiewicz, Antonio Bayés de Luna, Marek Malik, Juan Pablo Martínez, Pablo Laguna, and Esther Pueyo. Automatic SVM classification of sudden cardiac death and pump failure death from autonomic and repolarization ECG markers. *Journal of electrocardiology*, 48(4):551–7, jul 2015.
- [88] Crystal M Ripplinger, Qing Lou, Wenwen Li, Jennifer Hadley, and Igor R Efimov. Panoramic imaging reveals basic mechanisms of induction and termination of ventricular tachycardia in rabbit heart with chronic infarction: implications for low-voltage cardioversion. *Heart rhythm : the official journal of the Heart Rhythm Society*, 2009.
- [89] J M Rogers, J Huang, W M Smith, and R E Ideker. Incidence, evolution, and spatial distribution of functional reentry during ventricular fibrillation in pigs. *Circulation research*, 84(8):945–54, apr 1999.
- [90] Jack M. Rogers, Gregory P. Walcott, James D. Gladden, Sharon B. Melnick, and Matthew W. Kay. Panoramic Optical Mapping Reveals Continuous Epicardial Reentry during Ventricular Fibrillation in the Isolated Swine Heart. *Biophysical Journal*, 92(3):1090–1095, feb 2007.

- [91] J.M. Rogers. Combined Phase Singularity and Wavefront Analysis for Optical Maps of Ventricular Fibrillation. *IEEE Transactions on Biomedical Engineering*, 51(1):56–65, jan 2004.
- [92] K M Ropella, A V Sahakian, J M Baerman, and S Swiryn. The coherence spectrum. A quantitative discriminator of fibrillatory and nonfibrillatory cardiac rhythms. *Circulation*, 80(1):112–9, jul 1989.
- [93] G Salama, R Lombardi, and J Elson. Maps of optical action potentials and NADH fluorescence in intact working hearts. *The American journal of physiology*, 252(2 Pt 2):H384–94, feb 1987.
- [94] Gregor Schwartz, Benjamin C.-K. Tee, Jianguo Mei, Anthony L. Appleton, Do Hwan Kim, Huiliang Wang, and Zhenan Bao. Flexible polymer transistors with high pressure sensitivity for application in electronic skin and health monitoring. *Nature Communications*, 4:1859, may 2013.
- [95] Samuel F Sears, Tara Saia Lewis, Emily A Kuhl, and Jamie B Conti. Predictors of quality of life in patients with implantable cardioverter defibrillators. *Psychosomatics*, 46(5):451–7, jan 2005.
- [96] Michael J Shattock, Kyung Chan Park, Hsiang-Yu Yang, Angela W C Lee, Steven Niederer, Kenneth T MacLeod, and James Winter. Restitution slope is principally determined by steady-state action potential duration. *Cardiovascular research*, 113(7):817–828, jun 2017.
- [97] Karl A. Sillay, Paul S. Larson, and Philip A. Starr. Deep Brain Stimulator Hardware-Related Infections: Incidence and Management in A Large Series. *Neurosurgery*, 62(2):360–367, feb 2008.
- [98] Takao Someya, Yusaku Kato, Tsuyoshi Sekitani, Shingo Iba, Yoshiaki Noguchi, Yousuke Murase, Hiroshi Kawaguchi, and Takayasu Sakurai. Conformable, flexible, large-area networks of pressure and thermal sensors with organic transistor active matrixes. *Proceedings of the National Academy of Sciences of the United States of America*, 102(35):12321–5, aug 2005.
- [99] Micha E. Spira and Aviad Hai. Multi-electrode array technologies for neuroscience and cardiology. *Nature Nanotechnology*, 8(2):83–94, feb 2013.
- [100] Christoph Sprössler, Morgan Denyer, Steve Britland, Wolfgang Knoll, and Andreas Offenhausser. Electrical recordings from rat cardiac muscle cells using field-effect transistors. *Physical Review E*, 60(2):2171–2176, aug 1999.

- [101] M. S. Sulkin, E. Widder, C. Shao, K. M. Holzem, C. Gloschat, S. R. Gutbrod, and I. R. Efimov. Three-dimensional printing physiology laboratory technology. *AJP: Heart and Circulatory Physiology*, 305(11):H1569–H1573, dec 2013.
- [102] Charles D. Swerdlow, Walter H. Olson, Mark E. O’Connor, Donna M. Gallik, Robert A. Malkin, and Michael Laks. Cardiovascular Collapse Caused by Electrocardiographically Silent 60-Hz Intracardiac Leakage Current. *Circulation*, 99(19), 1999.
- [103] YOSHIHIDE TAKAHASHI, SHINSUKE IWAI, SYU YAMASHITA, MAYUMI MASMURA, MASAHIITO SUZUKI, KENTO YABE, YASUHIRO SATO, KENZO HIRAO, and MITSUAKI ISOBE. Novel Mapping Technique for Localization of Focal and Reentrant Activation During Atrial Fibrillation. *Journal of Cardiovascular Electrophysiology*, 28(4):375–382, apr 2017.
- [104] Kuniharu Takei, Toshitake Takahashi, Johnny C. Ho, Hyunhyub Ko, Andrew G. Gillies, Paul W. Leu, Ronald S. Fearing, and Ali Javey. Nanowire active-matrix circuitry for low-voltage macroscale artificial skin. *Nature Materials*, 9(10):821–826, oct 2010.
- [105] K. H. W. J. ten Tusscher and A V Panfilov. Alternans and spiral breakup in a human ventricular tissue model. *AJP: Heart and Circulatory Physiology*, 291(3):H1088–H1100, may 2006.
- [106] C THOMASJR, P SPRINGER, G LOEB, Y BERWALDNETTER, and L OKUN. A miniature microelectrode array to monitor the bioelectric activity of cultured cells. *Experimental Cell Research*, 74(1):61–66, sep 1972.
- [107] Bozhi Tian, Tzahi Cohen-Karni, Quan Qing, Xiaojie Duan, Ping Xie, and Charles M. Lieber. Three-Dimensional, Flexible Nanoscale Field-Effect Transistors as Localized Bioprobes. *Science*, 329(5993), 2010.
- [108] Arturo J Vegas, Omid Veisesh, Joshua C Doloff, Minglin Ma, Hok Hei Tam, Kaitlin Bratlie, Jie Li, Andrew R Bader, Erin Langan, Karsten Olejnik, Patrick Fenton, Jeon Woong Kang, Jennifer Hollister-Locke, Matthew A Bochenek, Alan Chiu, Sean Siebert, Katherine Tang, Siddharth Jhunjhunwala, Stephanie Aresta-Dasilva, Nimit Dholakia, Raj Thakrar, Thema Vietti, Michael Chen, Josh Cohen, Karolina Siniakowicz, Meirigeng Qi, James McGarrigle, Stephen Lyle, David M Harlan, Dale L Greiner, Jose Oberholzer, Gordon C Weir, Robert Langer, Daniel G Anderson, and Daniel G Anderson. Combinatorial hydrogel library enables identification of materials that mitigate the foreign body response in primates. *Nature Biotechnology*, 34(3):345–352, jan 2016.
- [109] Jonathan Viventi, Dae-Hyeong Kim, Joshua D. Moss, Yun-Soung Kim, Justin A. Blanco, Nicholas Annetta, Andrew Hicks, Jianliang Xiao, Younggang Huang, David J.

- Callans, John A. Rogers, and Brian Litt. A Conformal, Bio-Interfaced Class of Silicon Electronics for Mapping Cardiac Electrophysiology. *Science Translational Medicine*, 2(24), 2010.
- [110] Jonathan Viventi, Dae-Hyeong Kim, Leif Vigeland, Eric S Frechette, Justin A Blanco, Yun-Soung Kim, Andrew E Avrin, Vineet R Tiruvadi, Suk-Won Hwang, Ann C Vanleer, Drausin F Wulsin, Kathryn Davis, Casey E Gelber, Larry Palmer, Jan Van der Spiegel, Jian Wu, Jianliang Xiao, Yonggang Huang, Diego Contreras, John A Rogers, and Brian Litt. Flexible, foldable, actively multiplexed, high-density electrode array for mapping brain activity in vivo. *Nature Neuroscience*, 14(12):1599–1605, nov 2011.
- [111] Dirk Vollmann, Lars Lüthje, Stefan Vonnhof, and Christina Unterberg. Inappropriate therapy and fatal proarrhythmia by an implantable cardioverter-defibrillator. *Heart rhythm : the official journal of the Heart Rhythm Society*, 2(3):307–9, mar 2005.
- [112] A Vulpian. Note sur les effets de la faradisation directe des ventricules du coeur chez le chien. *Arch Physiol Norm Path*, 6:975–982, 1874.
- [113] Elaine Wan, Jeffrey Abrams, Richard L. Weinberg, Alexander N. Katchman, Joseph Bayne, Sergey I. Zakharov, Lin Yang, John P. Morrow, Hasan Garan, and Steven O. Marx. Aberrant sodium influx causes cardiomyopathy and atrial fibrillation in mice. *Journal of Clinical Investigation*, 126(1):112–122, nov 2015.
- [114] W. Kenneth Ward. A Review of the Foreign-body Response to Subcutaneously-implanted Devices: The Role of Macrophages and Cytokines in Biofouling and Fibrosis. *Journal of Diabetes Science and Technology*, 2(5):768–777, sep 2008.
- [115] D. F. Watson. Computing the n-dimensional Delaunay tessellation with application to Voronoi polytopes. *The Computer Journal*, 24(2):167–172, feb 1981.
- [116] J N Weiss, A Garfinkel, H S Karagueuzian, Z Qu, and P S Chen. Chaos and the transition to ventricular fibrillation: a new approach to antiarrhythmic drug evaluation. *Circulation*, 99(21):2819–26, jun 1999.
- [117] James N Weiss, Alain Karma, Yohannes Shiferaw, Peng-Sheng Chen, Alan Garfinkel, and Zhilin Qu. From pulsus to pulseless: the saga of cardiac alternans. *Circulation research*, 98(10):1244–53, may 2006.
- [118] N Wiener and A Rosenblueth. The mathematical formulation of the problem of conduction of impulses in a network of connected excitable elements, specifically in cardiac muscle. *Archivos del Instituto de Cardiologia de Mexico*, 16(3):205–65, jul 1946.
- [119] Carl J Wiggers. Studies of ventricular fibrillation caused by electric shock: II. cinematographic and electrocardiographic observations of the natural process in the dog’s

- heart. its inhibition by potassium and the revival of coordinated beats by calcium. *American Heart Journal*, 5(3):351–365, 1930.
- [120] Carl J Wiggers and R Wgria. Ventricular fibrillation due to single, localized induction and condenser shocks applied during the vulnerable phase of ventricular systole. *Am J Physiol*, 128:500–505, 1940.
  - [121] Wenzhuo Wu, Xiaonan Wen, and Zhong Lin Wang. Taxel-Addressable Matrix of Vertical-Nanowire Piezotronic Transistors for Active and Adaptive Tactile Imaging. *Science*, 340(6135), 2013.
  - [122] Xindong Liu, D.B. McCreery, R.R. Carter, L.A. Bullara, T.G.H. Yuen, and W.F. Agnew. Stability of the interface between neural tissue and chronically implanted intracortical microelectrodes. *IEEE Transactions on Rehabilitation Engineering*, 7(3):315–326, 1999.
  - [123] Lizhi Xu, Sarah R. Gutbrod, Andrew P. Bonifas, Yewang Su, Matthew S. Sulkin, Nanshu Lu, Hyun-Joong Chung, Kyung-In Jang, Zhuangjian Liu, Ming Ying, Chi Lu, R. Chad Webb, Jong-Seon Kim, Jacob I. Laughner, Huanyu Cheng, Yuhao Liu, Abid Ameen, Jae-Woong Jeong, Gwang-Tae Kim, Yonggang Huang, Igor R. Efimov, and John A. Rogers. 3D multifunctional integumentary membranes for spatiotemporal cardiac measurements and stimulation across the entire epicardium. *Nature Communications*, 5:3329, feb 2014.
  - [124] S Yamauchi, R B Schuessler, T Kawamoto, T A Shuman, J P Boineau, and J L Cox. Use of intraoperative mapping to optimize surgical ablation of atrial flutter. *The Annals of thoracic surgery*, 56(2):337–42, aug 1993.
  - [125] G Zeck and P Fromherz. Noninvasive neuroelectronic interfacing with synaptically connected snail neurons immobilized on a semiconductor chip. *Proceedings of the National Academy of Sciences of the United States of America*, 98(18):10457–62, aug 2001.
  - [126] Xin Zhou, Alfonso Bueno-Orovio, Michele Orini, Ben Hanson, Martin Hayward, Peter Taggart, Pier D. Lambiase, Kevin Burrage, and Blanca Rodriguez. In Vivo and In Silico Investigation Into Mechanisms of Frequency Dependence of Repolarization Alternans in Human Ventricular Cardiomyocytes Novelty and Significance. *Circulation Research*, 118(2):266–278, jan 2016.
  - [127] D P Zipes and H J Wellens. Sudden cardiac death. *Circulation*, 98(21):2334–51, nov 1998.

**High Resolution Cardiac Tools, Gloschat, Ph.D. 2017**